Terahertz Imaging and Quantum Cascade Laser Based Devices

by

Alan Wei Min Lee

Submitted to the Department of Electrical Engineering and Computer Science
in partial fulfillment of the requirements for the degree of
Doctor of Philosophy
at the
MASSACHUSETTS INSTITUTE OF TECHNOLOGY
February 2010

Author .....
Department of Electrical Engineering and Computer Science
January 29, 2010

Certified by .....
Qing Hu
Professor
Thesis Supervisor

Accepted by .....
Terry P. Orlando
Chairman, Department Committee on Graduate Students

Terahertz Imaging and Quantum Cascade Laser Based Devices

by

Alan Wei Min Lee

Submitted to the Department of Electrical Engineering and Computer Science on January 29, 2010, in partial fulfillment of the requirements for the degree of Doctor of Philosophy

Abstract

The terahertz (THz) frequency range (f=0.3-10 THz, λ=30-1000 μm) is much less technologically developed that the adjacent microwave and infrared frequency ranges, but offers several advantages for imaging applications: THz wavelengths offer better spatial resolutions than microwave frequencies, and THz radiation is able to penetrate materials that are opaque at infrared frequencies (e.g. packaging, plastics, paints and semiconductors). These features, combined with the unique THz spectral signatures of chemicals have lead to the development of terahertz imaging systems for non-destructive test. However, the weak radiation sources in these existing systems result in single pixel scanning architectures requiring minutes to acquire images or enhanced speed at the expense of signal to noise ratio (SNR).

In this thesis, a system for real-time imaging is demonstrated using recently developed terahertz quantum-cascade laser (QCL) sources, along with commercial, focal plane array thermal detectors. The system uses a high power (48 mW) 4.3-THz QCL, which is also

used to characterize the focal plane array, resulting in a noise equivalent power (NEP) of 320 pW/√Hz. The source and detector are used in a synchronous detection scheme, resulting in an SNR of ~25 dB/pixel at a 20-Hz frame rate. This represents a two order of magnitude improvement in speed over previous systems at comparable SNRs. Real-time imaging over a 25-m distance is described, using a QCL adjusted for emission in the narrow 4.9 THz atmospheric transmission window.

The challenges posed by the long THz wavelengths in QCL waveguide design leads to a tradeoff between high temperature operation (<186K) and high power/good beam patterns (248 mW peak, 12deg FWHM). To mitigate these tradeoffs, a technique for butt-coupling a metal-metal waveguide QCL to an index matched lens is developed. The resulting device achieves the highest reported power for a MM waveguide (145 mW peak) and while retaining a high operating temperature (160 K) and achieving a narrow beam pattern (<5deg).

The lens coupling technique is also used to add spectroscopic capability to the system, through the development of an external cavity QCL. The butt-coupling of an anti-reflection coated lens to a semi-insulating surface plasmon waveguide QCL results in increased optical losses and suppression of lasing. Lasing is recovered using an external optical system with a reflective grating for frequency selective feedback. A device is characterized showing 4% tuning range at ~4.4 THz, and is among the first demonstrations of tunable THz QLCs.

Thesis Supervisor: Qing Hu
Title: Professor

Acknowledgements

I would first like to thank my supervisor Qing Hu for giving me the opportunity to work on this project and for his steady guidance throughout. His teaching and emphasis on obtaining key results have contributed greatly to my development as a researcher.

A lot of credit goes to John Reno, for the excellent MBE growth of the quantum-cascade lasers used in this work, along with my group-mates who designed and fabricated them, Benjamin Williams and Sushil Kumar. In addition enabling my project with the best terahertz quantum-cascade lasers, Ben and Sushil have always made themselves available to answer questions and teach valuable lab technique. Thanks also go to past and present students of the group for their help and stimulating conversations: Stephen Kohen, Hans Callebaut, Allen Hsu, Qi Qin, Wilt Kao, David Burghoff and Ivan Chan. I would particularly like to thank Qi Qin and Stephen Kohen for their help in experimental work and in electromagnetic simulation.

I would like to thank David Staelin and Cardinal Warde for serving as my thesis committee and for their useful suggestions and comments.

This work would not have been possible without the love and support of my wife Jessica, who transplanted her life and career from California in order to make Boston our home. I consider myself fortunate to have someone I can analyze a problem with and who can sense when I need to leave the lab or when to push harder for a goal. The balance that she has brought to my life has made these years much richer, for which I am indebted to her.

I would like to thank my parents, for their love, support and guidance over the years. Their keen interest in my work has helped supply me with motivation. I would also like to thank my sister and my extended family for their loving support.

Table of Contents

List of Figures

List of Tables

1 Introduction

1.1 Terahertz frequency range

The terahertz (THz) spectrum lies in the frequency range of 0.3 to 10 THz (or in wavelength, 1 mm to 30 μm, as shown in Figure 1-1) and exists in between two readily accessible frequency bands: the microwave (<0.3 THz) and the infrared (>10 THz). The lack of technological development in the terahertz range is largely due to a lack of applications, particularly when compared with the development of microwave and infrared component, which have been driven by military and commercial uses [1-3]. Until recently, the primary interest in the terahertz spectrum has been from the astronomy and atmospheric science community. For astronomers, light emitted by cool interstellar dust, which falls in the terahertz frequency range, gives information about the formation of stars and planets [4, 5]. Some estimates indicate that over half the total luminosity and 98% of photons emitted since the Big Bang are in the terahertz [6]. For atmospheric science, many gasses in the upper atmosphere have thermal emission lines at terahertz frequencies which give information on ozone destruction, global warming and pollution [7].

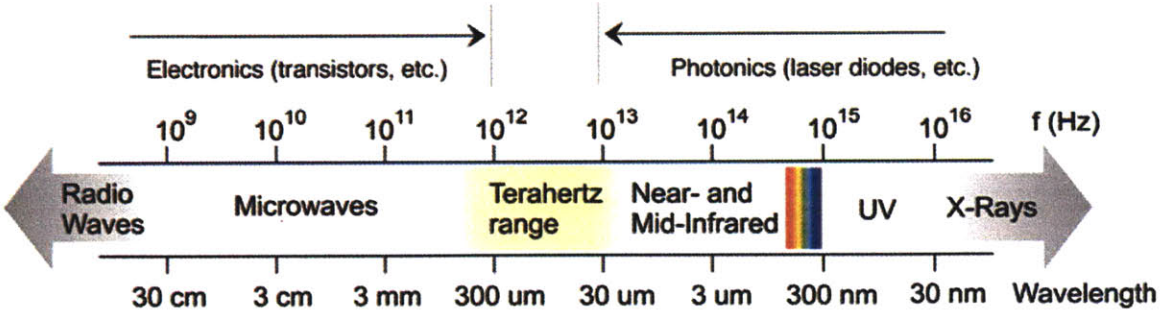

Figure 1-1 The electromagnetic spectrum, which shows the underutilized terahertz spectrum between the well developed microwave and infrared ranges.

1.2 Applications in spectroscopy

Until recently, few terrestrial applications existed for terahertz technology. This has slowly changed with the development of the terahertz pulse spectrometer (TPS) in the

1980's, enabling both sensitive spectroscopy and imaging at terahertz frequencies [8, 9]. These systems use ultrafast, femtosecond infrared pulses, typically from a Ti:sapphire laser[1] to both generate and detect THz radiation, as depicted in Figure 1-2 [10]. The most common technique, known as photoconductive switching, focuses the femtosecond pulse at the center of an antenna patterned on a semiconductor (part a). This generates electron hole pairs which are accelerated under an applied DC bias, resulting in a pulse of current which is radiated by the antenna whose electric field is proportional to the time derivate of the current, $E_{radiation} \propto dJ/dt$ [10]. In a modern system, a picosecond long pulse typically results, containing frequency components from approximately 100 GHz to 5 THz. This pulse is then efficiently coupled to freespace by integrated optics and reflective optics (part b). Conversion efficiency is on the order of 10^{-4}~10^{-6}, resulting in low average pulse power levels of microwatts levels [11]. As a result, specialized phase-sensitive coherent techniques are required for detection. A photoconductive detection technique, similar to the generation method, can be used to correlate the picosecond long terahertz pulse with the femtosecond long infrared pulse. As before, the infrared beam is first focused to the center of an antenna generating electron hole pairs. These carriers are accelerated by the terahertz electric field coupled to the antenna by freespace optics. Typically the semiconductor in the detector is modified so that the carriers have a short lifetime (i.e. sub-picosecond carrier lifetimes of low temperature grown GaAs). This fast current allows the terahertz beam to be "sampled" by changing the relative timing of the terahertz and infrared pulse, typically using a movable delay line. This sampling current, which is proportional to the terahertz electric field, is too fast to be resolved by external electronics attached to the antenna, and instead the average current is measured. The result is the coherent detection of the picosecond long pulse (red trace in part c) which can be Fourier transformed to reveal its spectral content. An object placed between the source and the detector results in a time delay, shown by the blue trace, which can be used to determine the thickness of the sample if the index of refraction is know, or the index refraction if the thickness is known. Loss of the material can be determined by the difference in amplitude of Fourier transform.

[1] Typical parameters for the Ti:sapphire laser are $\lambda \approx 780$ nm, pulse lengths, τ_{pulse} <100 fs, average power levels of, $P_{avg} \approx 100$ mW, with repetition rates of ≈ 100 MHz.

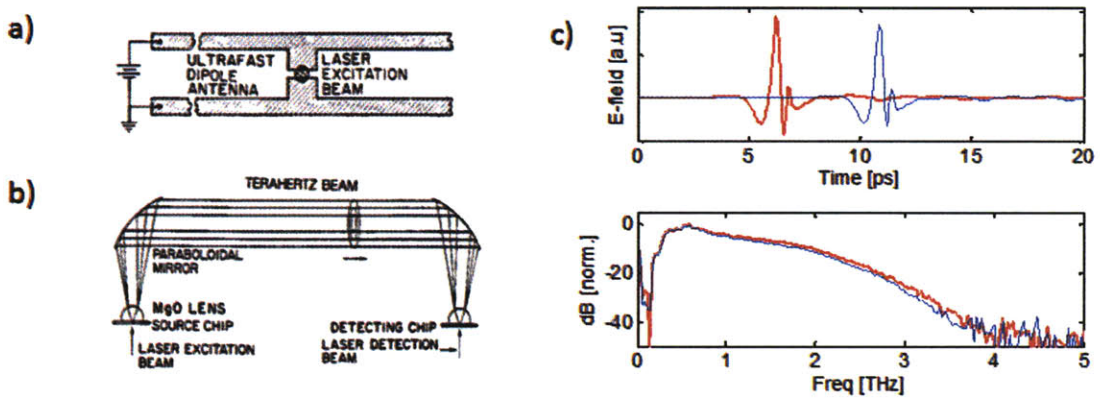

Figure 1-2 Schematic of pulsed terahertz spectroscopy system demonstrated by *Van Exter et. al.*[9]. Part (a) shows a photoconductive antenna patterned on semiconductor. A pulse of infrared light photoexcites carriers at the center of the antenna. Carriers are accelerated by DC bias, resulting in a current pulse, with terahertz spectral components. The pulse is radiated by the arms of then antenna, coupled to freespace using optical setup shown in (b). Detection is accomplished by correlation of terahertz pulse with infrared pulse in a photoconductive antenna, resulting in time domain pulse in (c) (red trace). Sample placed in terahertz beam results in delay of pulse (blue trace). Fourier transformed spectra allow measurement of the loss in the sample.

Determination of both the index of refraction and the loss (the optical constants n and k) as a function of frequency is a significant improvement over incoherent systems, such as grating spectrometers or Fourier transform infrared spectrometers (FTIRs), where only one parameter is determinable. Single pixel signal-to-noise ratios (SNRs) can be quite high as well, reaching ~60 dB in some systems, compared with ~20 dB typical of an FTIR at terahertz frequencies[12]. This 10^4 improvement over FTIR has triggered a period of exponential growth for TPS systems resulting in several vendors producing THz systems [13-15], and over 100 groups currently using THz frequencies for research [16]. As a result terahertz spectral libraries for common materials are being developed (e.g. NIST [17] and RIKEN [18] in Japan) and properties of many materials are now well understood, allowing applications to be developed.

One example is in analysis of pharmaceuticals in manufacturing quality control [19, 20]. TPS has shown the ability to determine between crystalline forms (polymorphs) by the

frequencies of the resonant absorption peaks (see Figure 1-3). While the manufacture of one form or another is well controlled by using specific solvents, controlling rates of cooling and degree of saturation in solution, the solid can transform from one form to another by incorrect storage or final preparation. The different forms lead to different physical and chemical properties of the material, and may affect the dissolution, bioavailability and/or stability of the compound. While it is possible to similar analysis at near-infrared or visible frequencies, the packaging material (plastics and paper) are only transparent at terahertz frequencies. This allows for a rapid through package screening system.

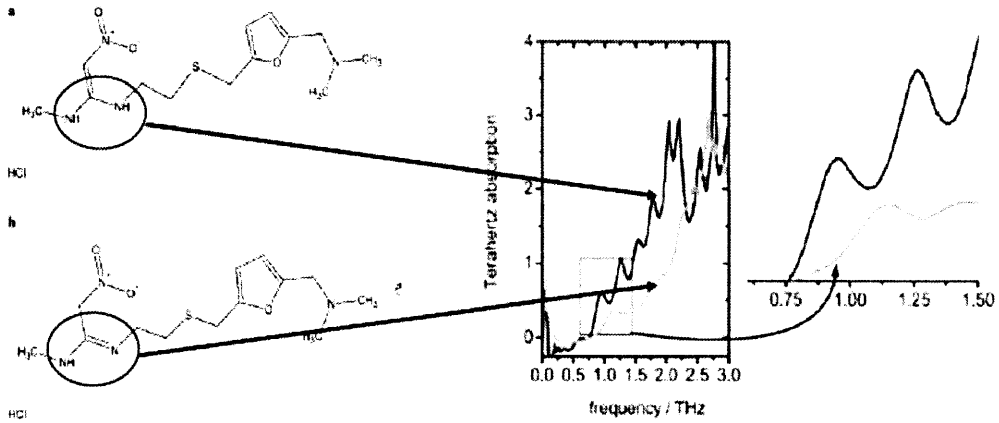

Figure 1-3: Parts (a) and (b) show the isomers of the common heart burn medication ranitidine hydrochloride, with their respective terahertz absorption spectra shown in (c). The resonant absorption peaks are likely due to large-amplitude torsional vibrations or intermolecular (nearest neighbor) interactions, which shift in frequency or are suppressed depending on which isomer is crystallized. Adapted from *Taday et. al.* [19].

1.3 Applications in imaging

Applications using terahertz for imaging are also been pursued using the same TPS systems, where full images are acquired by scanning objects through the beam [10, 21, 22]. The majority of THz imaging work that has been done uses the same single-pixel, raster scanned, terahertz pulsed imaging (TPI) system first demonstrated by Hu and Nuss in 1995 (Figure 1-4) [21]. Here an object, such as the microchip or leaf shown in the figure, is scanned through an intermediate beam focus. The false color intensity of the images result from taking the peak of the time domain pulse shown in Figure 1-2 from integration of the spectra over an a frequency range (typical values of 0.3 to 3 THz).

From these images the advantages of using terahertz frequencies are apparent: good spatial resolution allowing fine detail between the microchip to be seen, and the ability to penetrate materials that are opaque at infrared frequencies, such as paper, plastics, ceramics and semiconductors. Furthermore, unlike UV or x-ray photons, THz photon energies are low (1 – 42 meV) making ionization of molecules unlikely.

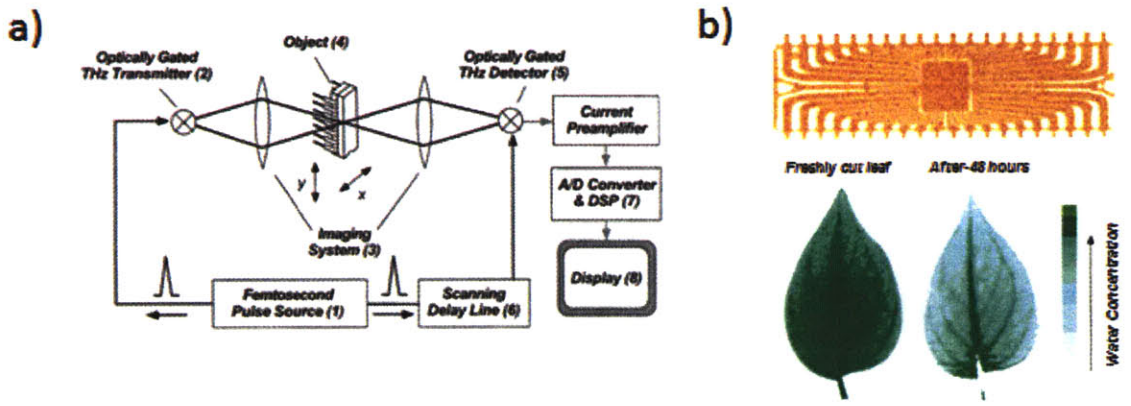

Figure 1-4 Schematic of pulsed terahertz imaging system demonstrated by *Hu and Nuss* (part a) [21]. Part (b) shows resulting raster scanned transmission images. False color pixel intensity results from integrating spectra over 1-3 THz bandwidth. Images acquired at 12 pixels/s ~50K pixels/image.

This unique combination of advantages has been used with good success in non-destructive test. For example NASA has used terahertz for the evaluation of unique materials operating under extreme conditions [23-25]: urethane based spray-on foam insulation (SOFI) and silica based shuttle tile for use in the thermal protection system. Here the use of terahertz is necessary because these materials have low densities, making ultrasound impossible, and they are also non-conductive, making eddy current systems impossible. Detachment of SOFI foam was responsible for the Columbia shuttle disaster when a section punctured the shuttle wing during liftoff [26]. As a result, NASA selected terahertz NDT as one of the technologies for pre-flight quality control [27]. Results from evaluation of the technology are shown in Figure 1-5 and show the detection of numerous defects and voids concealed within the SOFI foam.

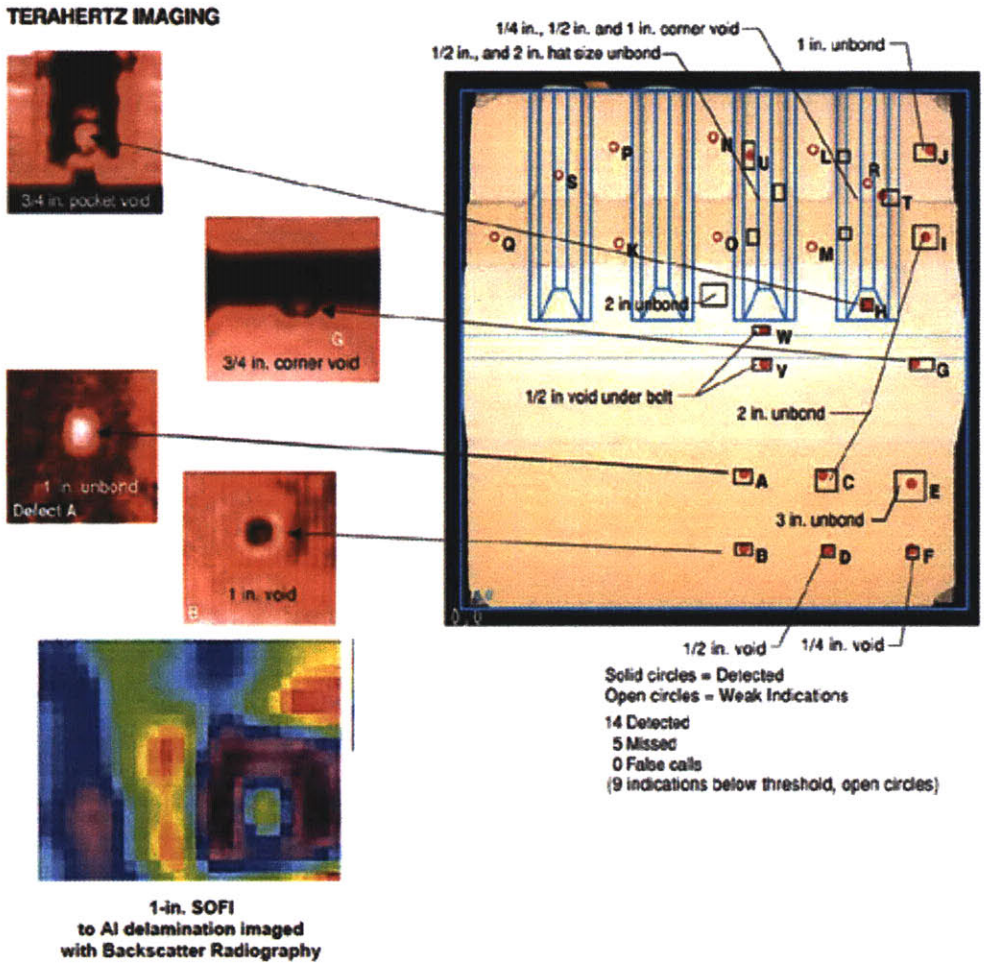

Figure 1-5 Terahertz imaging uses for non-destructive test of spray on foam insulation (SOFI) used on the shuttle external tank PAL ramp. Terahertz images taken in reflection and show subsurface detection of defects. Images from [27].

While TPI results in good quality images, allowing the detection of defects for NDT, imaging rates are typically in the 10 to 100 pixel/s range, requiring 10's of minutes to form an imaged due to the ~60 dB SNR, the requirement of a scanning delay line for detection, and the need to mechanically scan the object through the terahertz beam (or the beam over the object). Furthermore the use of a femtosecond laser adds an additional layer of complexity and cost, resulting in systems that cost >$100K [28].

To overcome the limitations of imaging speed, the detector used in this technique can be modified so that a THz image is formed on a large area electro-optic (EO) crystal, allowing real-time imaging (Figure 1-6) [29, 30]. The two dimensional THz electric

field distribution on the crystal changes the polarization of the femtosecond infrared probe pulse via the Pockels effect. This small shift in polarization of the probe pulse is then measured using a crossed polarizer (analyzer) and a CCD camera. Because the THz pulse is spread over a large area, there is a tradeoff between SNR (typical values of ~30 dB per pixel) and the number of pixels imaged (typically a 1000 pixels per second). Unfortunately this detector scheme is much less effective when combined with higher average power continuous-wave sources, which have lower peak power levels, and hence lower electric field strengths [31].

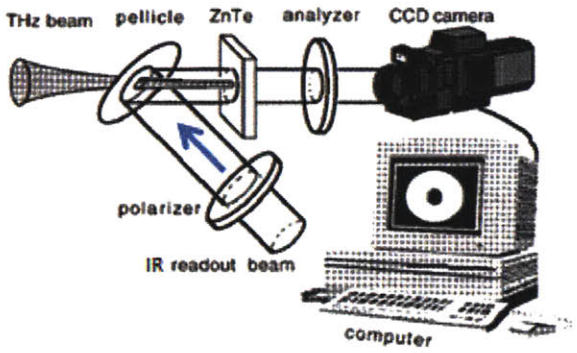

Figure 1-6 Schematic of 2D pulsed terahertz imaging system demonstrated by *Wu et. al.* [29]. Polarized readout beam of near-infrared light is combined with THz beam through pellicle beam combiner. Near-infrared birefringence in ZnTe is modified by electric field of THz beam (Pockels effect), resulting in polarization rotation of near-infrared beam measured by a polarizer (analyzer) and a CCD camera. The electric field of the THz beam can have a two dimensional spatial pattern resulting in local changes of crystal birefringence.

1.4 Real-time terahertz imaging

A more conventional approach to real-time imaging can be taken by using multi-element arrays of incoherent (direct) detectors along with a high-power source for illumination. Unlike coherent detectors which are sensitive to field, direct detectors are sensitive to incident power. High-power, continuous-wave (CW) sources based on electronics, sources such as Gunn oscillators and Schottky multiplier chains have limited powers levels (~10's of μW) above 1.5 THz, owing to transit-time and resistive-capacitive charging effects which scale with $1/f^4$ [32-34]. Optically pumped gas-lasers have high c.w. power levels, but they are large, complex and only have limited coverage of the

terahertz spectral region depending on the energies of the rotational-vibrational transitions of the gases being used [35-37]. For instance a 2.5 THz methanol gas-laser pumped by a CO_2 gas-laser was developed as a local-oscillator source for the Microwave Limb Sounder instrument on the Aura satellite resulting in very stringent requirements, and is a demonstration of the state-of-the-art for this technology: 18 mW c.w. output power, in a 22 Kg package measuring 75×30×10 cm^3, using < 120 W of power.

As a proof of concept, an imaging system using a methanol vapor laser was demonstrated as depicted in Figure 1-7 [38]. The ~10 mW c.w. laser beam is focused using low loss, reflective off-axis parabolic mirrors. An object (an envelope in the figure) is illuminated and imaged onto a focal plane array whose operation is characterizations are detailed in sections 2.1 through 2.3. These arrays are primarily sensitive to the 7-14 μm (≈20-40 THz) wavelength range which encompasses the peak of the 300 K blackbody emission at 10 μm. These "night vision" arrays are produced commercially by BAE Systems [39, 40]. Commercial pyroelectric arrays with 100's of $nW/\sqrt{Hz}$ of sensitivity at THz frequencies were known prior to this work[2], however it was discovered that microbolometer arrays tuned for infrared frequencies have sensitivity on the order of 1 $nW/\sqrt{Hz}$ at THz frequencies, offering two order of magnitude of improvement[41].

As an alternative to the far-infrared gas laser, the THz quantum cascade lasers (QCLs) are attractive because they are compact, high-power, solid-state, sources of radiation [42-44]. Despite the need for cryogenic cooling, these devices produce 10's or 100's of mW of power, and can be engineering to emit over a range of frequencies currently spanning a range of 1.2 to 4.9 THz [45-48]. Their operation is briefly summarized below, with thorough reviews given in [49-51]. Using QCL sources for illumination (part b), a differential imaging system is implemented (section 2) which reduces $1/f$ noise, and the infrared background present in the scene. The differencing procedure is done over 3 frames and begins with the terahertz radiation applied during the first frame. During the second frame, the microbolometers are still warm from the THz radiation, and their values are discarded. By the third frame, the microbolometers have had adequate time to

[2] Broadband Pyroelectric detector: Pyrocam III, Spiricon Inc.

cool, and this frame is subtracted from the first frame, resulting in a differential image. Because $1/f$ noise and slow moving thermal imagery are relatively constant from frame to frame, they are effectively canceled by this scheme, leaving only the terahertz signal. The resulting imaging system has a signal to noise ratio of 27 dB while imaging $>10^5$ pixels per second, two orders of magnitude improvement in speed over previous systems [38, 41].

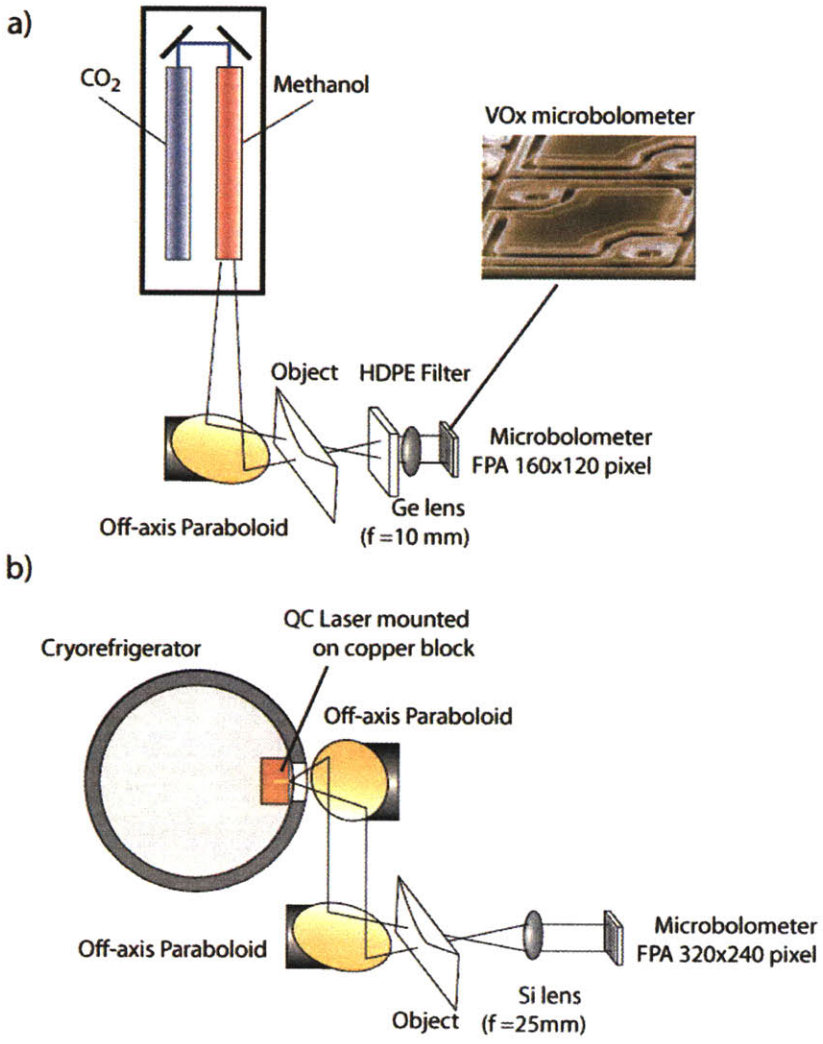

Figure 1-7 Real-time terahertz imaging experimental setups using high power lasers: part (a) show CO_2 laser optically pumping methanol gas laser, operating at 2.5 THz; part (b) shows QCL in a cryorefrigerator. Both setups show transmission mode imaging using large format microbolometer detectors (shown in inset of part (a)).

1.5 Quantum-cascade lasers

Quantum cascade lasers are electrically pumped, unipolar devices in which population inversion takes place between the intersubband transitions in quantum wells of a semiconductor heterostructure. By engineering of the thicknesses of the quantum wells and barriers, the energy spacing of the subbands can be adjusted, in principle allowing arbitrary photon energies to be achieved. While the first theory on intersubband emission was published in 1971, the first realization was significantly later, in 1994 by Faist *et. al.* [52]. Several technological advances were required for this demonstration including the refinement of molecular beam epitaxy (MBE), necessary for the growth of the thin layers (<10 nm) of quantum wells/barriers, and novel design strategies to mitigate the fast (~picosecond) relaxation times of intersubband transitions. The resulting design (Figure 1-8 part a) shows the conduction band structure of the first QCL which used the GaInAs/AlInAs material system. The amplitude squared wave functions show the active subbands in the laser, which roughly equate to a four level laser: the upper and lower radiative states, n = 3 and n = 2 respectively an excited ground state, n = 1, and the ground state represented by the digitally graded alloy. Electrons injected into the structure when the device is lasing, undergo stimulated emission from n = 3 to n = 2 then quickly relax to n = 1 by fast scattering through emission of a longitudinal-optical (LO) phonon. Electrons then tunnel to the doped, digitally graded allow of GaInAs/AlInAs for reinjection into the upper radiative state of the next module.

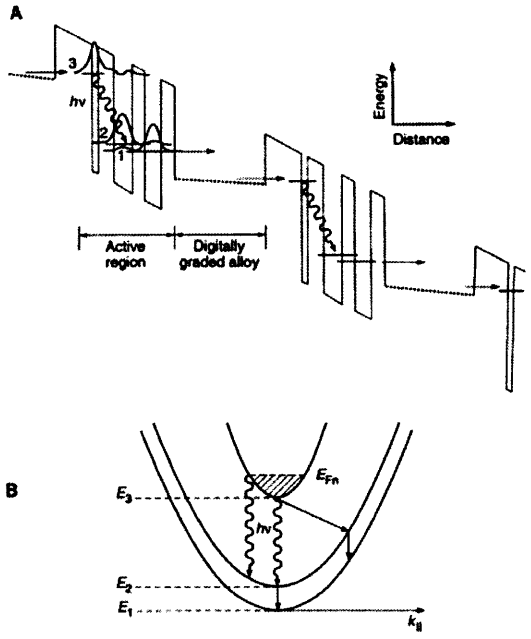

Figure 1-8 Part (a) Conduction band diagram of the first quantum-cascade laser from Faist *et. al.*[52] . Numbered amplitude squared wave functions show radiation between upper and lower energy levels (3-2), with lower level rapidly depopulated by resonant loginitudinal-optical (LO) phonon (2-1). Digitally graded alloy collects electrons and reinjects them into the next module completing cascade pumping scheme.

The relationship between population inversion, ΔN, and the relaxation times of the upper state, τ_u, the lower state, τ_l, and upper-to-lower state, $\tau_{u\to l}$, and the injected current density J, is given by the solution to a two level rate equation:

$$\Delta N = \frac{J}{e} \cdot \tau_u [1 - \frac{\tau_l}{\tau_{u\to l}}] \qquad \textbf{Eq. 1-1}$$

Here, a large τ_u, and $\frac{\tau_u}{\tau_{u\to l}} \ll 1$ lead to strong population inversion. Intuition on these relaxation rates can gained by looking at part b, which shows the electron dispersion in subbands n =1 to 3. These subbands are nearly parabolic as electrons can move freely in the plane perpendicular to growth, i.e. they are only confined in the growth direction. The primary mechanism of non-radiative relaxation of the upper state is by electron-LO-phonon scattering. As the separation of n=3 and n=2 is relatively large compared with the LO-phonon energy, $E_{32} >> E_{LO}$, a large exchange of moment must occur the emission of an LO-phonon (shown as solid arrow from subband 3 → 2). This leads to a

relatively long relaxation time $\tau_{3\to2}$ and upper state lifetime τ_u . By contrast, τ_{21} ($\approx \tau_l$) is much shorter as $E_{21} \approx E_{LO}$, and no exchange of momentum is required, resulting in a favorable ratio of $\frac{\tau_l}{\tau_{u\to l}}$, leading to population inversion and gain.

A key feature of QCLs is the cascade pumping scheme allowing a single electron to emit multiple photons, resulting in greater than unity differential quantum efficiency. For this first example, 25 modules were cascade between dielectric cladding layers, providing waveguiding. Since this initial demonstration, mid infrared QCL development has been swift, resulting in commercial devices with watt level c.w. performance at room temperature, and devices that tune over 40% of the center frequency.

1.6 Terahertz quantum-cascade lasers

By comparison, the development of QCLs below the Restrahlen band, the optical phonon absorption band of polar semiconductors (8~9 THz in GaAs/AlGaAs material system typically used for terahertz), was more challenging due to two main difficulties. Firstly, the mid-infrared strategy of fast depopulation of the lower radiative state by LO phonon scattering is more challenging at terahertz frequencies because the photon energies (<20 meV) are lower than the LO phonon energies (36 meV). This makes selective depopulation of only the lower state difficult, as the upper state will have a similar lifetime. Secondly, there is a challenge in designing low loss waveguides for longer terahertz wavelengths, as free carrier absorption scales with λ^2, and dielectric guiding results in impractically thick cladding layers on the order of 10's of microns.

Breakthroughs in band structure designs resulting in lasers were demonstrated by three groups in quick succession: Köhler *et. al.* in 2001 [42], Rochat *et. al.* in 2002 [43], and Williams *et. al.* in 2002 [44]. Since these initial demonstrations, the designs based on Williams have shown the highest operating temperature of 186 K [53] and the highest power levels of 248 mW [54], and are used for this work. The conduction band profile of a design (labeled FL183R-2) is shown in Figure 1-9 at the design bias. An individual gain module consists of four quantum wells of GaAs/$Al_{0.15}Ga_{.085}As$, and is encircled in

the dashed lines. The barrier thicknesses in the module correspond to (from left to right with the barriers in bold) **48**/82/**17**/68/**40**/164/**34**/90 in Å. The total QCL active region is ~10 μm thick, consisting of 183 modules cascaded together.

Understanding of the design shown in Figure 1-9 is aided by an expression for the peak material gain, g_{peak}, of an intersubband transition:

$$g_{peak} \propto \frac{\Delta N_{if} \cdot f_{if}}{\Delta \nu} \qquad \textbf{Eq. 1-2}$$

Here the gain is related to the population inversion between the radiative levels i and f, ΔN_{if}, the oscillator strength, f_{if}, and the spontaneous emission line width of the transition, $\Delta \nu$. The spontaneous emission line width cannot be directly designed and is a function of the scattering mechanisms present in the transition. The unitless oscillator strength, $f_{if} = (2m^* \omega z_{if}^2)/\hbar$, is an indicator of the strength of coupling between the optical field and the $i \rightarrow f$ transition, and is proportional to the square of the dipole moment, $z_{ij} = \langle i|z|f\rangle$. For intersubband transitions there is a well known selection rule which permits only interaction with the growth direction polarized electric field. The oscillator strength between the radiative transition, $5 \rightarrow 4$ in Figure 1-9, can be maximized by spatially overlapping the wavefunctions, however this at the expense of decreasing the upper state lifetime through enhanced inelastic scattering mechanism (e.g. electron-electron, impurity, and surface roughness). Fast depopulation of n = 4 occurs through a resonance with n =3 which is coupled by LO phonon scattering to the n = 1,2 levels. This depopulation is both rapid and selective as the n=3,4 and n=1,2 levels are separated by approximately the LO-phonon energy. In terms of Eq. 1-1 a favorable ratio of $\frac{\tau_2}{\tau_{3\rightarrow 2}}$ is obtained allowing population inversion is achieved. Because the n =5 and n = 1,2 levels are spatially separated, non-radiative relaxation from $5 \rightarrow 1,2$ is suppressed.

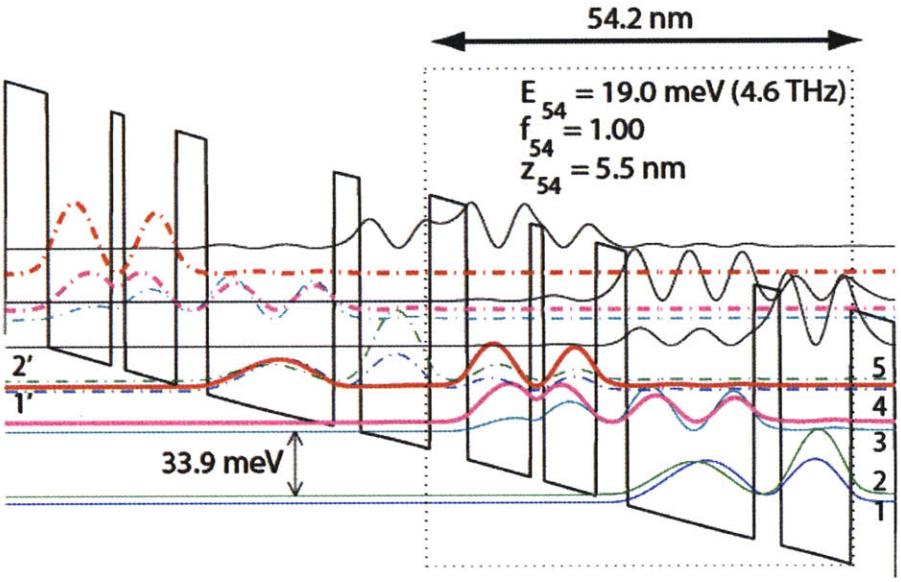

Figure 1-9 Conduction band diagram of the QCL used in this work (design FL183R-2). Active region is formed by 183 repeats of the outlined four well module, shown at design bias of 11 kV/cm (59.5 mV/module). Radiative transition occurs between 5 → 4. Electrons in 4 rapidly relax through resonance with n = 3 and fast LO phonon emission to n = 1,2, where electrons can be injected into next module. Widest well n-doped at 1.9×10^{16} cm^{-3}

1.7 Terahertz quantum-cascade laser waveguides

The low loss semi-insulating surface Plasmon (SISP) waveguide was initially demonstrated by Ulrich [55] and used in the first demonstration of a terahertz QCL by Kohler [42]. An SISP waveguide structure is shown schematically in Figure 1-10 part (a) and consists of the top metal contact above a GaAs/AlGaAs active region on a thin (<1 μm) heavily doped n^+-GaAs contact layer on a semi-insulating GaAs substrate. The doping level causes the plasma frequency to be above the operating frequency of the laser, resulting in a negative dielectric constant at the <5 THz operating frequencies of the QLCs. This results in a surface plasmon mode which attaches to the n^+ layer and decays exponentially into the semi-insulating substrate. The result is a low loss waveguide whose intensity mode profile is shown for a typical 10×100 μm^2 mesa.

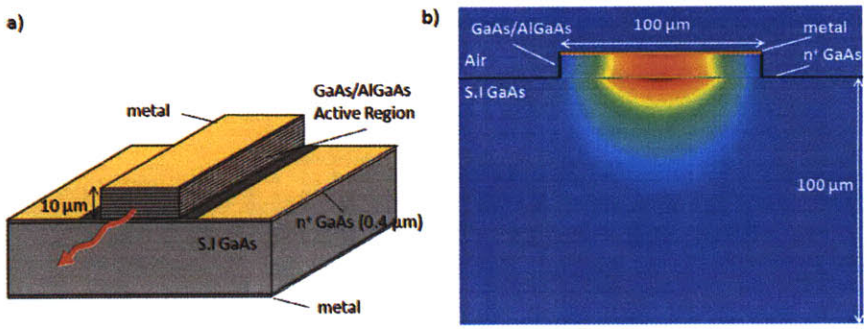

Figure 1-10 Part (a) shows semi-insulating surface plasmon waveguide structure. Active region is has top metal contact, and sits above a thin, heavily n-doped layer (400 nm, silicon doped at 3×10^{18} cm^{-3}), above a nominally undoped (semi-insulating) substrate. A surface plasmon mode results from the negative dielectric constant of n-doped layer, resulting in the optical mode shown in (b).

The optical mode of the SISP extends into the substrate resulting in a relatively low divergence beam patterns, approximately 85% of the beam is collected by an *f*/1 optic in section 2.4. This relatively large mode also results in low reflectivity (32%) of a cleaved facet, the typical output coupling mirror for QCLs. This reflectivity is entirely due to index of refraction mismatch between the GaAs/AlGaAs semiconductor and air. This low reflectivity results in high output powers, also characterized in section 2.4. Both the high power levels and the good beam patterns make this waveguide useful for illuminating multi-element direct detectors, with results reported in section 2.5.2.

A drawback to the use of SISP waveguides is the low mode confinement, Γ, defined as the spatial overlap of the optical mode with the active region, which is typically less than 50% for this waveguide. As less of the gain material is "seen" by the optical mode, more gain is required to achieve lasing. As the gain decreases with temperature, the low Γ leads to limited operating temperatures, below ~105 K and high-power, CW performance to temperatures below ~40 K [54]. In contrast to SISP waveguides, metal-metal (MM) waveguides have a near unity confinement factor, Γ, lower threshold gains, and high operating temperatures of 186 K in pulsed operation [53]. However, this high confinement also results in high end-facet reflectivities of 70% to 90% depending on the wavelength and geometry [56], compared with 32% for SISP based devices. The high reflectivities result because of dielectric mismatch and modal mismatch. This increased

reflectivity limits output coupling and hence limits output power levels to ~10 mW. The highly confined mode which is much less than the freespace wavelength result in highly divergent beam patterns exceeding 180° [57]. A more quantitative comparison of these waveguides is given in Appendix A.

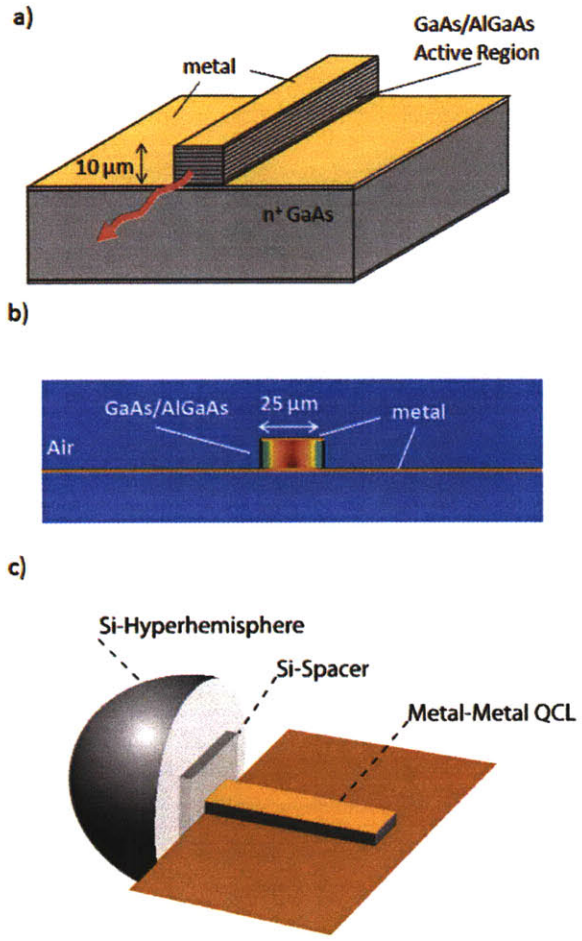

Figure 1-11 Part (a) shows metal-metal (MM) waveguide consisting of a top and bottom metal layers enclosing QCL active region. Part (b) shows optical mode and near unity optical confinement (overlap of optical mode with active region), similar to microstrip transmission line. Part (c) shows lens-coupled MM waveguide for enhance output coupling, and reduced beam divergence.

In chapter 3 a MM waveguide QCL with an optically-coupled silicon hyperhemispherical lens is demonstrated (shown in Figure 1-11). The metal-metal waveguide end facet is abutted to a high-resistivity silicon wafer (n~3.4) providing a good index match to the GaAs/AlGaAs (n~3.6) active region of the waveguide. The residual reflectivity of the MM waveguide at the silicon interface is due to the discontinuity of the guided mode, and this interface acts as the laser output mirror. The reduced reflectivity (increased mirror

loss) leads to ~5× higher output powers, and narrow beam patterns of ~5° FWHM, while retaining high temperature performance[58].

In chapter 4 an approach for tunable lasers is described using the same lens coupling technique, but used with a SISP waveguide. As the optical mode of the SISP waveguide is substantially larger than that in the MM waveguide, the reflectivity is much more plane wave like, and can be reduced <1% by abutting to an index matched silicon lens. Using an external grating as a frequency selective feedback mirror, the output of the laser can be tuned (shown in Figure 1-9)[59].

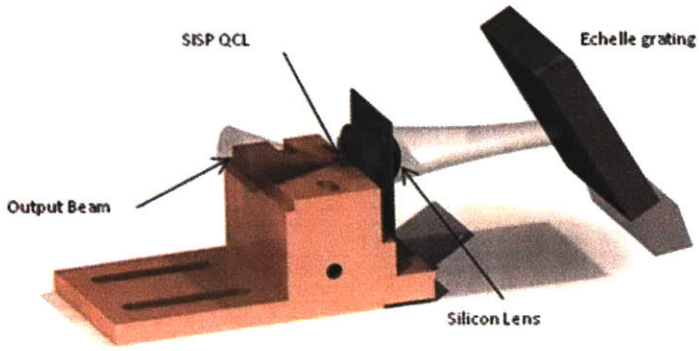

Figure 1-12 External cavity QCL (EC-QCL): Semi-insulating surface plasmon waveguide THz QCL, mounted on a copper block abutted to a high-resistivity silicon hyperhemispherical lens with a grating for external feedback. Silicon lens held in place by metal retaining clip.

2 Real-Time THz Imaging using QCLs

This chapter describes the components and the system performance used for the real-time imaging setup pictured in Figure 1-7. A key enabling component, the larger format microbolometer array produced by BAE Systems, is described in section 2.1 along with a brief background on incoherent detectors at terahertz frequencies. Among the attractive features of this array are its size, 320×240 microbolometer elements, and its ability to operate at room temperature yet still be sensitive to terahertz radiation. Prior to these commercially available arrays, only 100× less sensitive pyroelectric arrays or specially purposed cryogenically cooled arrays for astronomy were available [60, 61]. The microbolometer absorption at terahertz frequencies and the resolution limits of the system are calculated in sections 2.2 and 2.3 respectively. When combined with a 4.3 THz QCL operating at 30 K,[3] whose performance and beam pattern results are presented in section 2.4, real-time imaging results. The microbolometer array sensitivity is characterized using the 4.3 THz QCL in section 2.5.2, with imaging results present in section 2.5.3. A discussion of the atmospheric losses is presented in section 2.6, as well as results in coarse tuning of QCLs for emission in atmospheric windows.

2.1 Bolometer Detectors

Incoherent, direct detectors, i.e. detectors with an electrical response in proportion to the incident power, generally fall into two categories: photodetectors and thermal detectors. The photodetectors, such as quantum well infrared photodetectors (QWIPS)[62-64] and gallium doped germanium detectors [61, 65-67], operate on the photoexcitation of carriers across energy gaps. These energy gaps can be naturally occurring such as the shallow gallium dopants in a germanium host crystal (~6 meV), or they can be

[3] Though it may be noted that QCLs operate cryogenically, their high temperature performance is continually improving. The current record, 186 K, is well beyond what is required for compact Stirling cycle cyrocoolers, which have minimum temperatures <77 K and are compact and reliable (e.g. Ricor #543, 0.6 W power dissipation at 77 K, with MTTF of 15,000 hours in <1 Kg package). QCLs are also now compatible with commercial multistage Peltier coolers, which have minimum temperatures of 167 K, allowing for an all solid state source (e.g. 6 stage Peltier cooler from Marlow Industries). Using either of these forms of cooling would result in a compact imaging system.

engineered, such as the energy separation of intersubband transitions in quantum wells (QWIPS) or quantum dots/rings (TQDIP, QRID). In either case there is a cutoff energy and frequency, $E_g=h\cdot\nu_{cutoff}$, below which photons are not readily absorbed. Since these devices operate in thermal equilibrium, carriers are thermally excited across the energy gap roughly in proportion to $e^{-Eg/kT}$, which for values $T>h\cdot\nu_{cutoff}/3k$ creates a large dark current, degrading the noise performance. For a photodetector with a 1 THz cutoff frequency, the detector dark current will become significant at ~15 K, overwhelming the photo-generated signals. This trend is plotted in Figure 2-1 using a theoretical dark current limited photodetector with various cutoff frequencies and is closely followed by the commercial and literature photodetectors. Figure 2-1 uses the common figure of merit of detectivity, D* ("D-star"):

$$D^* = \frac{\sqrt{A}}{NEP} \qquad \left[\frac{cm \cdot Hz^{1/2}}{W}\right] \qquad \textbf{Eq. 2-1}$$

For D^* comparisons, larger number indicate better noise performance. Here the NEP, units of $W/Hz^{-1/2}$, is defined as the power absorbed by the detector which is required to create a signal to noise ratio of unity in a 1 Hz bandwidth. For the dark current limit:

$$NEP_{dark} = \frac{\sqrt{2 \cdot I_{dark} \cdot e \cdot \Delta f}}{R} \qquad \left[\frac{W}{\sqrt{Hz}}\right]$$
$$\approx \frac{\sqrt{2 \cdot n_{dark} \cdot v_{sat} \cdot e^2 \cdot \Delta f}}{R} \qquad \textbf{Eq. 2-2}$$

Where v_{sat} is the saturation velocity of the carriers (on the order of 1×10^7 cm/s for GaAs) and R is the responsivity of the photodetector in A/W and is assumed to be $e/h\nu$ for an ideal detector.

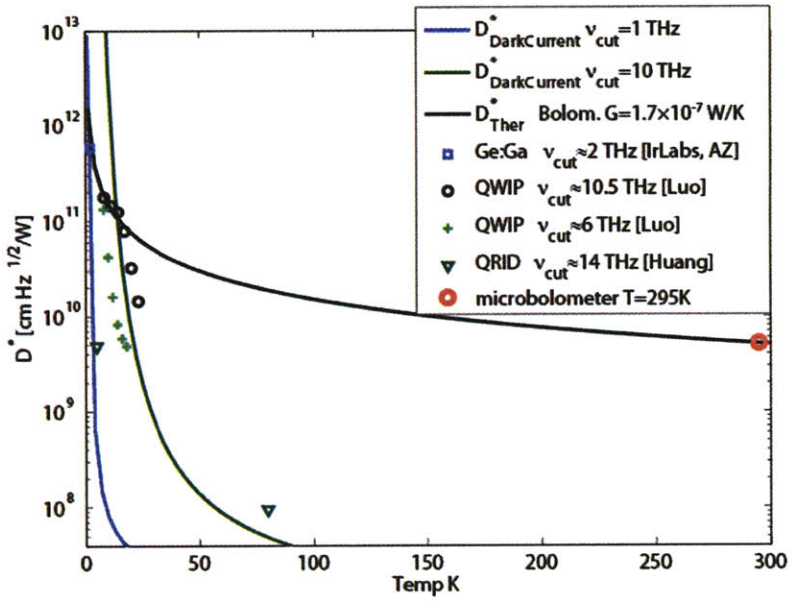

Figure 2-1 (colored lines) D* performance of dark-current limited photodetectors parameterized by cutoff frequency (ν_{cutoff}) using GaAs with n=1·10^{16}/cm^3 donors at v_{sat}=1·10^6 cm/s. (black line) D* performance of thermal fluctuation limited bolometer with thermal conductivity G=1.7× 10^{-7}. Devices in legend indicated for reference.

Thermal detectors do not rely on energy gaps and instead detect the amount of absorbed power through sensitive thermometer elements: pyroelectric detectors create a polarization charge induced by temperature changes; bolometers typically take advantage of a change in resistance due to temperature changes. In both cases, the temperature sensing function can be decoupled from the radiation absorption function, allowing separate optimization of both functions. Optimization of the temperature sensing function has been done on multi-element arrays produced by BAE Systems, shown in Figure 2-2 part (a) [40]. Absorbers can be made to absorb efficiently over a narrow range of frequencies, such as the ~80% absorption over the 7 – 14 μm thermal emission band of the BAE microbolometers. The bolometer structure consists of a MEMS microbridge suspended by support legs above a reflective backplane, shown schematically in part (b). The microbridge acts as an absorber of incident power (P) and also contains a temperature sensitive resistive film of vanadium oxide (VOx).

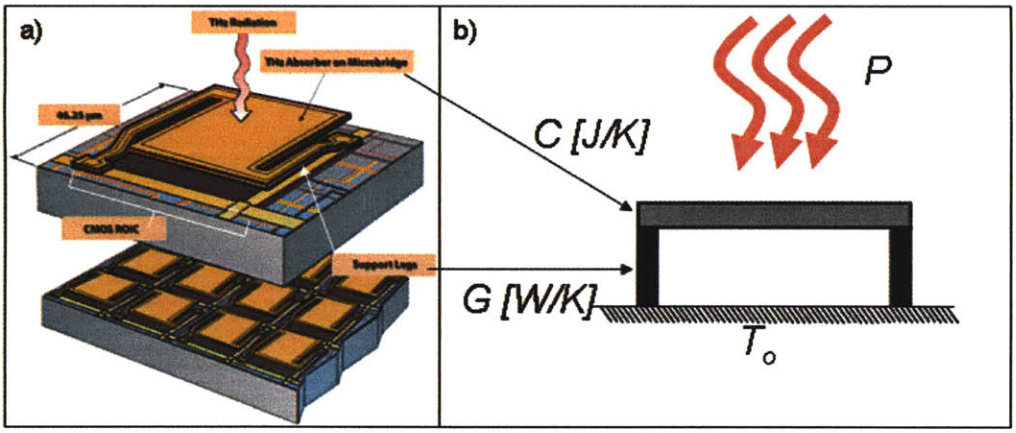

Figure 2-2 THz Microbolometer Focal Plane Array. Part (a) shows an enlargement of a single microbolometer element pictured above a small array. Part (b) shows a schematic of the key components of the bolometer for analysis.

For a given incident power, P, and absorption efficiency η (which is a function of wavelength, as described below), the steady state change in temperature of microbridge is primarily a function of the thermal conductivity (G in W/K) of the support legs:

$$\Delta T = \eta \cdot \frac{P}{G} \qquad [K] \qquad \textbf{Eq. 2-3}$$

The microbridge is formed primarily of silicon nitride for structure, with an embedded thin film of vanadium oxide (microbolometer stack shown in Figure 2-3), which has a large fractional temperature change of resistance, TCR [40] [68]:

$$\text{TCR} = \frac{1}{R} \cdot \frac{dR}{dT} \qquad \textbf{Eq. 2-4}$$

Deposition of the vanadium oxide layer forms a large number polymorphic phases (V_4O, V_2O, VO, etc), and as a result, are typically referred to as VO_x, where x is the concentration of oxygen. TCR values for this microbolometer are -2%/K, and result from thermally activated transport of localized states [69]. For small values of G a large temperature difference between the microbridge and the underlying substrate (T_o) can be developed for a given amount of incident power. This temperature difference is measured using a bias current, I, to develop a voltage signal:

$$S_v = \frac{I \cdot dR/dT}{G} \quad [\frac{V}{W}] \qquad \textbf{Eq. 2-5}$$

The resulting expression, S_V, shown here in the low frequency limit, is the voltage produced by the device for a given bias current per watt of absorbed optical power. The bias current is chosen to be large enough to suppress the Johnson noise (or noise from the resistance of the bolometer, $NEP_{Johnson}$) and amplifier noise (both current and voltage, NEP_{V/I_Amp}) terms in the noise expression:

$$\begin{aligned} NEP_o &= \left[NEP_{Therm}^2 + NEP_{Johnson}^2 + NEP_{V-amp}^2 + NEP_{I-amp}^2\right]^{\frac{1}{2}} \\ &= \left[\frac{4kT^2G\Delta f}{\eta^2} + \frac{4kTR\Delta f}{\eta^2 S_v^2} + \frac{V_A^2\Delta f}{\eta^2 S_v^2} + \frac{I_A^R R^2 \Delta f}{\eta^2 S_v^2}\right]^{1/2} \end{aligned} \qquad \textbf{Eq. 2-6}$$

Here Δf is the noise bandwidth (~half the sampling rate ~30 Hz) and k is Boltzmann's constant ($1.38 \cdot 10^{-23}$ J/K). The total optical noise equivalent power, NEP_O the optical power necessary to generate an SNR of 1, consists of contributions from several statistically independent noise parameters: the value $\sqrt{4kTR}$ is the Johnson voltage noise from the resistance of the VOx layer, and V_A and I_A are the voltage and current noise density of the microbolometer amplifier. For a sufficiently high responsivity, the dominant term is the thermal fluctuation noise, NEP_{Therm}, whose physical origin is the statistical fluctuations of quantized carriers (phonons) through the support legs. Using values from Table 2-1 and the 4% optical efficiency calculated for the THz region in section 2.2, the NEP_o is calculated to be $\sim 150 \times 10^{-12}$ W/Hz$^{1/2}$, including the ~38% transmission through a germanium vacuum window, obtained from Fresnel reflection of an air/germanium interface ($n_{Ge} \approx 4$ [70]).

Table 2-1 Nominal Microbolometer Device Parameters [40]

Detector Parameter	Value
Pitch	46.26 μm
Heat Capacity – **C** [J/K]	$2 \cdot 10^{-9}$ J/K
Thermal Conductivity – **G** [W/K]	$1.7 \cdot 10^{-7}$ W/K
Time Constant	12 ms
Bolometer TCR	-2 %
Fill Factor	48 %
Resistance	15 kOhm
Resistance Uniformity	<10%
Avg. Absorption (**η**)	
IR: 8-12 μm	80%
THz: 30-300 μm	4%

Though the NEP_o is limited by NEP_{Therm}, and consequently thermal conductance G, its value is constrained by the thermal time constant $\tau=C/G \approx 12$ ms, where C is the heat capacity of the microbolometer, which is minimized by using thin film materials. This value must be kept below ~16 ms, to maintain a 60 Hz framerate. Values of thermal fluctuation limited D^* are plotted in Figure 2-1 for the THz absorptive microbolometer array, showing good performance at room temperature.

2.2 Microbolometer Absorption

The absorption of the microbolometer has been optimized by BAE Systems for the 7 – 14 μm 'Night Vision' absorption band, and are poor absorbers at terahertz frequencies (0.3 to 10 THz or in wavelength, 1 mm to 30 μm). The absorption as a function of wavelength is calculated using transmission line analysis (plane wave at normal incidence) of the **Si_3N_4/Vox/Si_3N_4**/Air/TiW structure with thicknesses of 0.65/0.03/0.65/1.8/Infinite, in units of μm, reported in [71] and shown in Figure 2-3. The layers in bold constitute the microbridge structure suspended a short distance from a TiW reflecting layer. The thicknesses of the layers result in 80% absorption over the 7 – 14

μm band. At the center wavelength, 10 μm, the structure forms a resonant optical cavity as the microbridge and reflecting layer form a near λ/4 resonator. However, at longer THz wavelengths, the cavity is no longer resonant and the reflecting backplane reduces the absorption in the microbridge, i.e. in microwave terms, the backplane acts as a backshort. Optical absorption is further reduced by the decrease in absorption of the VOx/Si_3N_4 layers with decreasing frequency – the average absorption over the 1-10 THz range is ~4%.

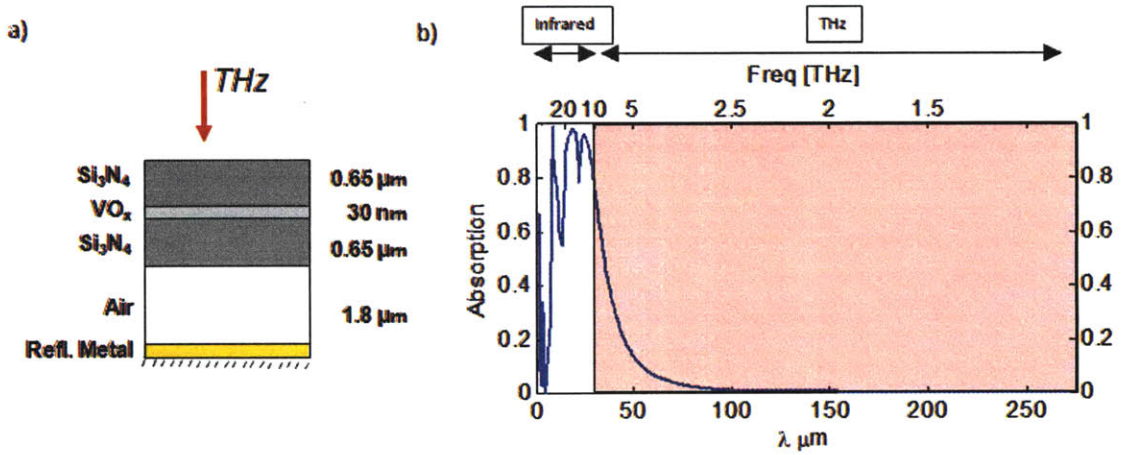

Figure 2-3 Thin film composition of microbolometer structure (as seen from the side). Part (b) shows absorption vs wavelength. Average absorption over terahertz range (<10 THz) ~4%. Average absorption over infrared range (7-14 μm or 21 to 52 THz) 80%.

2.3 Resolution

The microbolometers were designed for operation around a 10-μm wavelength, and are quite small, 46.25 μm × 46.25 μm, when compared with the 70-μm wavelength of the 4.3 THz QCL used in this experiment. For a simple f/1 imaging configuration shown in Figure 2-4, the diffraction limit is calculated as $x = 1.22 \cdot \lambda \cdot \frac{f}{d} \approx 170\ \mu m$, where *f/d* is the f/number of the lens. The root mean square (RMS) spot size of a ray trace at the focus shows diffraction limited performance, which is 2× the pixel size. As a result the array is oversampled by 4×, and the 320×240 elements become effectively a 160×120 element array.

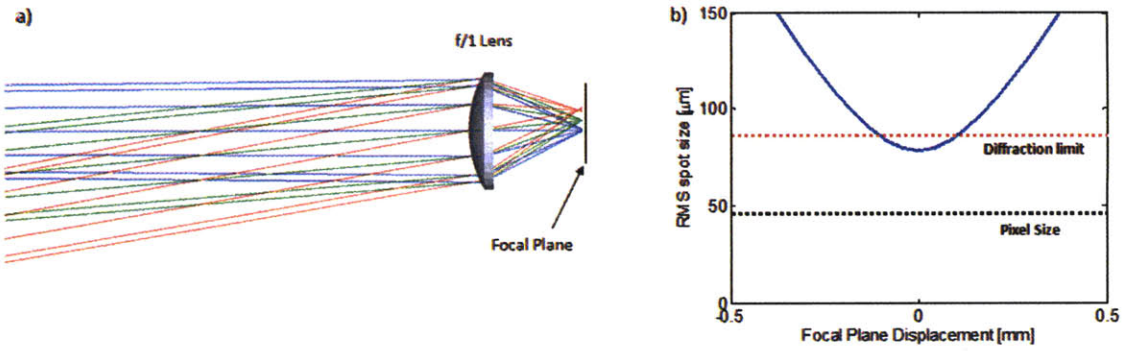

Figure 2-4 Part (a): a simple imaging configuration using a high-resistivity silicon lens (low THz absorption). Part (b): the RMS blur spot size vs focal plane displacement from optimum position showing diffraction limited performance which is 2.5× the pixel size.

2.4 QCL characteristics

The growth, fabrication, and characterization of the QCL used in this work are detailed in [54] and [51] and are briefly summarized here. The active region of the laser measures 98-μm wide × 2.15-mm × 10-μm high, and uses the SISP waveguide shown in Figure 1-10, with a semi insulating substrate thickness of 170 μm. The front facet is defined by cleaving, and an Al_2O_3/Ti/Au high-reflectivity (HR) coating is applied to the rear facet. The device was mounted in a liquid helium cryostat operating at ~4 K, and characterized for output power versus current in pulsed and DC biases are shown in Figure 2-5 parts (a) and (b) respectively. Short 200 ns pulses were used part (a), minimizing the heating in the active region resulting in a peak power of ~135 mW at a 10 K heat sink temperature. At higher heat sink temperatures (after allowing the helium to boil off) higher currents are required to achieve lasing threshold, as the gain is reduced with temperature, as seen by the lasing threshold current density versus temperature in the inset. The typical pulsed lasing spectra of the device is also shown in an inset, measured by Fourier transform infrared spectrometer. Part (b) shows the continuous wave characteristics of the device This device produces a maximum CW power of 125 mW 10 K, and ceases to lase much above 40 K.

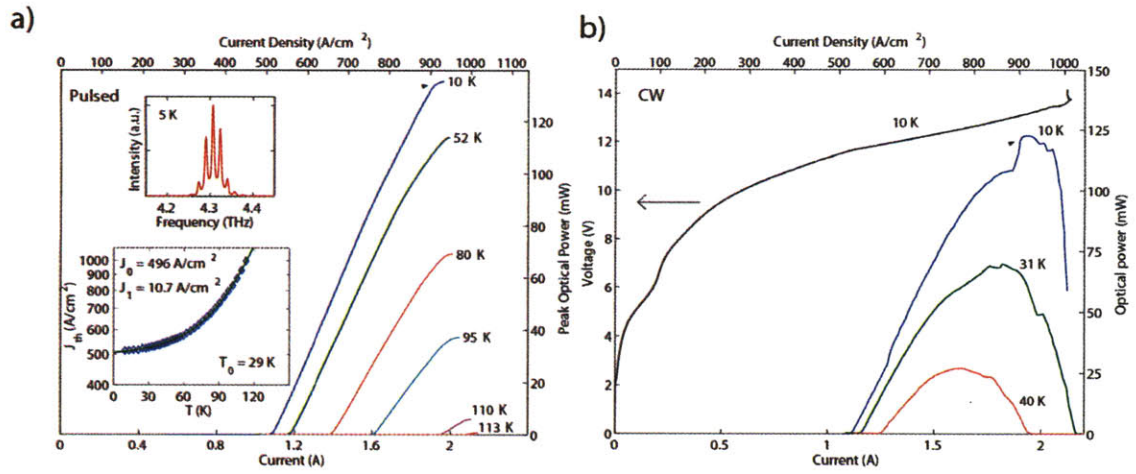

Figure 2-5 Output power versus current characteristics for 98-μm wide × 2.15-mm long FL183R-2 device (band diagram shown in Figure 1-9), fabricated in SISP waveguide with a substrate thickness of 170 μm, with the rear facet HR coated. Part (a) shows characteristic for 200 ns pulses at a repetition rate of 100 KHz, modulated at 1 KHz (1% duty cycle). Output power was measured with a pyroelectric detector (Molectron P4-42) with the peak power was calibrated using a thermopile detector (ScienTech model AC2500H) without correction for collection efficiency or optical losses of the vacuum window. Part (b) shows continuous wave operation measured with an optical chopper with the peak calibrated to the same thermopile detector.

For practical use in imaging, it is inconvenient to continually fill the liquid helium dewar, and instead a closed cycle pulse tube cryocooler is used (Cryomech PT60). This closed cycle cooler uses helium gas as the refrigerant, to cool down to 28 K without a heat load. When a thermal load is applied the temperature was observed to increase nearly linearly at 1.4 K/W. When used with the 4.3 THz QCL listed above continuous wave operation is not possible, as the device power dissipation is 12V ×1.25 A ≈ 15 W at lasing threshold. This results in a heatsink temperature of $T_o + \Delta T = 28K + 1.4\,[\frac{K}{W}] \times 15[W] \approx 49\,K$, which would further increase the lasing threshold in a positive feedback loop. As a result the device output power decreases as the duty cycle increases shown in Figure 2-6. Because the microbolometer camera has a thermal time constant $\tau \approx 12$ ms, longer pulses are favored. The optimum pulse length is determined experimentally in section 2.5.

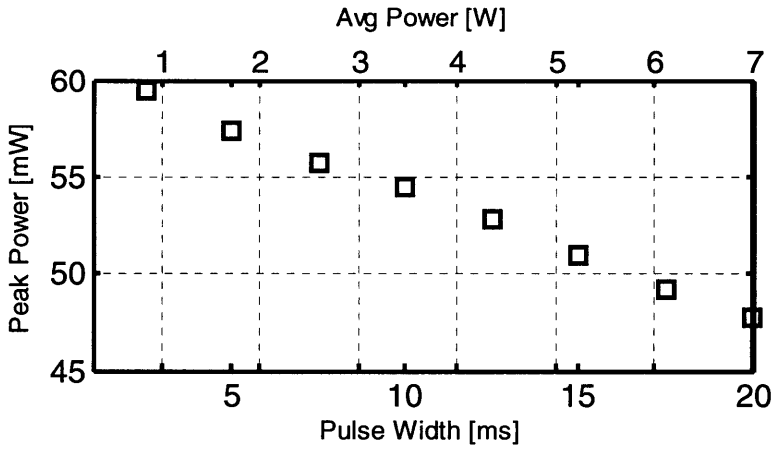

Figure 2-6 Peak power vs pulse width of 98-μm wide × 2.15-mm long FL183R-2 SISP device. Pulse period is 50 ms with average power dissipated in the device shown in alternate x-axis.

The emitted beam from SISP device is shown in Figure 2-7. Measurement of the beam pattern was done using the microbolometer focal plane array. While the microbolometer array is physically large, 320×160 elements with a 46.25-μm pitch for a total area of 14.8×11.1 mm^2, the cyrocooler vacuum shroud limits the placement of the array to 35 mm from close to the device facet. As a result the image of Figure 2-7 is constructed by tiling 24 individual images in a rectilinear fashion. No effort was made account for view factor of the pixels at higher angles. Here the central lobe is approximately 12 to 13° full width at half maximum, however significant amounts of power are contained in the beyond this central lobe. To determine what optic should be used to collect light from this device, part b shows the amount of power collected as a function of collection angle. For an f/1 lens approximately 85% of the power seen in the image is collected. It is likely that this is an upper limit as higher order diffraction from the sharp discontinuities of the SISP waveguide lead to radiation at high angles not collected by this setup.

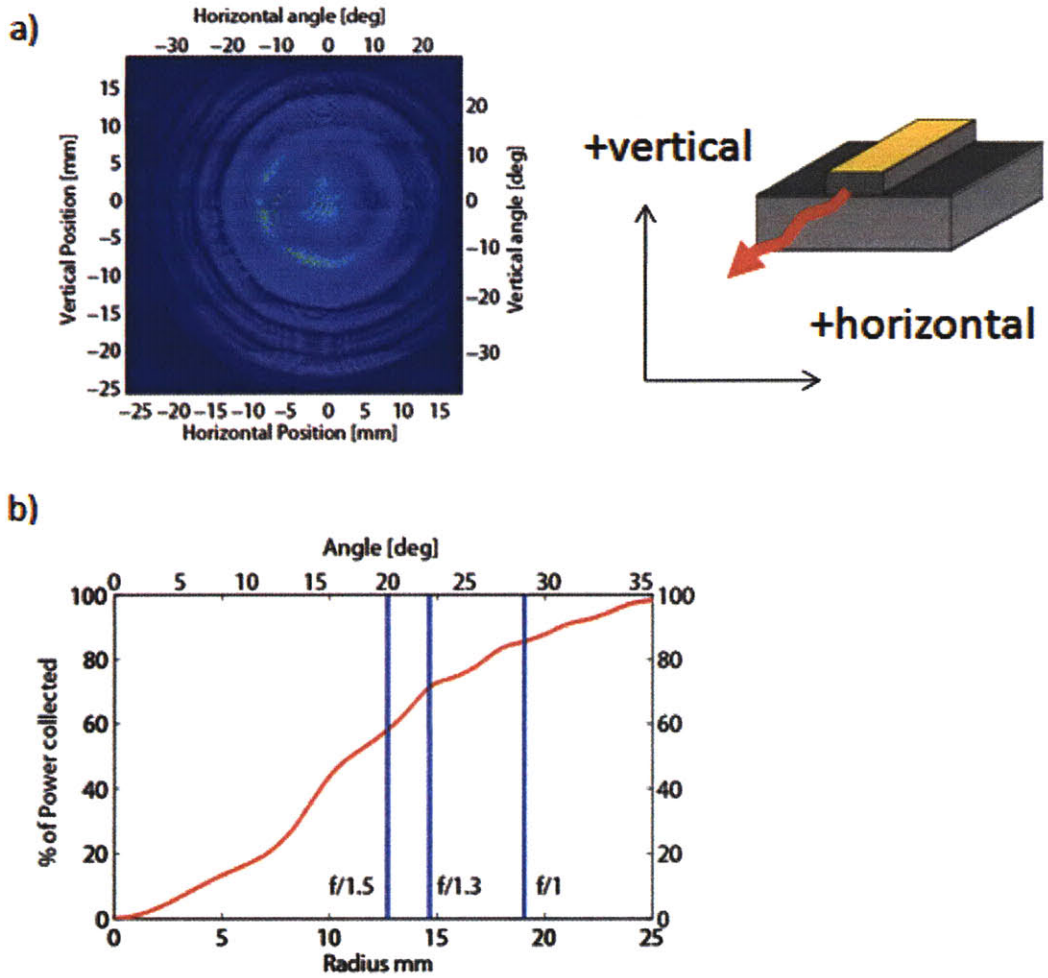

Figure 2-7 Part (a) shows beam pattern measured from 98-μm wide × 2.15-mm long FL183R-2 SISP device. Beam image taken by translating microbolometer focal plane array position 35 mm from the laser facet, and stitching image together. Part (b) shows orientation of QCL with respect to image. Part (c) shows amount of light collected as a function of collection angle subtended, or equivalently circle radius at the 35-mm distance. Lines shown equivalent angles subtended by optics with indicaed f/numbers

2.5 Imaging system

2.5.1 Synchronous Detection

When the QCL light is incident on the focal plane array, the resulting image has a terahertz light superimposed on a strong infrared background (Figure 2-8 part b), due to the strong absorption in the infrared. In order to allow the subtraction of the infrared background the QCL is biased synchronously with the first (signal) frame of a three frame sequence. Due to the thermal time constant of the microbolometer, some residual

THz signal remains in the second frame, and it is discarded (not shown in the figure). The third (reference) frame, (c), is used as the infrared background and is subtracted from the first frame, resulting in a THz only image (d).

Timing with the acquisition scheme of the camera is crucial and is shown in part (a). Pixels in a row are sampled simultaneously with rows being acquired sequentially with a 64-μs period for each row until the last row (#240), after which there is 1.47 ms of inactive time, for a total frame acquisition time of 16.6 ms. Synchronization with the terahertz pulse is considered through a simple heating model: As a pulse of incident radiation is absorbed by the microbolometers, heating causes a resistance change which is represented in the sampled signal:

$$x[n_1, n_2] = R_o P\left(1 - e^{-\frac{t}{\tau}}\right) \quad [counts] \qquad \textbf{Eq. 2-7}$$

Here x is the value of pixel (n_1,n_2) in digital "counts" equivalent to voltage, R_o is the responsivity in counts/watt, P is the incident power, and τ is the thermal time constant of the microbolometers ~ 12 ms. The terahertz pulse is applied during the inactive time (at t = -1.47 ms) to allow the microbolometers to heat up before the first row is acquired. The signal rises with a ~12 ms thermal time constant until the end of the pulse, where the signal decays with the same time constant. It is possible to allow complete cooling and use larger delays, i.e. use the 3rd or 4th frame after the terahertz pulse as the reference. However if the delay is more than a few frames, slow signal variations due to 1/f noise will be included in the measurement, and any motion between frames will results in incomplete infrared signal cancellation. However if the delay between frames is too short, as in the case of alternate frame differencing (subtracting frame 2 from frame 1), the microbolometers will have inadequate time to cool, resulting in negative signal for the first few rows. With these considerations, it was found that a 3 frame differential scheme was optimal. This differential imaging scheme obviates the need for infrared blocking filters, but the drawback of this scheme is the reduced frame rate of from 60 Hz to 20 Hz.

Timing signals are derived from the infrared camera which generates a frame synchronization signal at the beginning of the frame acquisition. A field programmable gate array (FPGA) is used to generate the pulses for the QCL, which are then used to gate the DC power supply used to bias the QCL. The raw image data is acquired from the microbolometer camera on a PC with synchronization data from the FPGA marking the first frame. This allows the frames 1 and 3 to be differenced and displayed in real time on the PC.

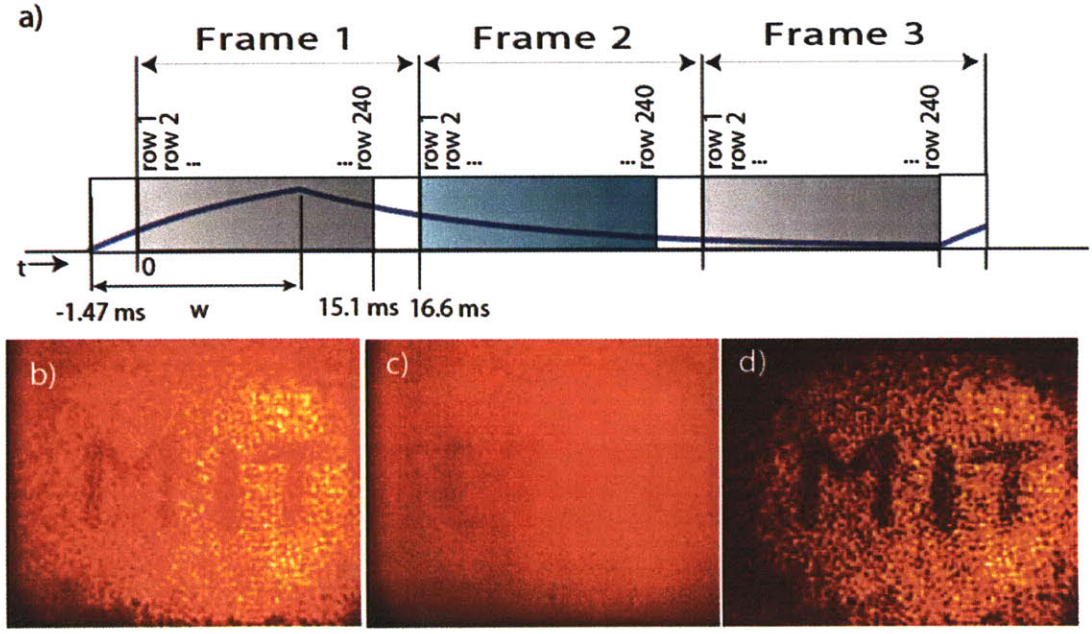

Figure 2-8 Part (a): solid trace shows signal/temperature time response to a QCL pulse, over a three frame differential sequence; a frame is composed of sequential row samples of the signal. A 1.47 ms delay exists between frames allowing the pulse to be started before the first row is acquired to allow heating. Part (b) corresponds to frame 1 with THz superimposed on infrared signal. Part (c) corresponds to frame 3: infrared signal with a small amount of residual THz signal. Part (d) corresponds to difference between frames 1 & 3, resulting in THz only signal; showing absorption of pencil inside an envelope.

An additional benefit to this differential scheme is the suppression of 1/f noise, which increases with integration time without the differential scheme as shown in Figure 2-9. Here the signal of the bolometer, x[t], is taken without differencing, as a function of time, where the variable t indicates the frame number. As the microbolometers are DC coupled (i.e. sensitive to long term drift) increasing amounts of noise are included at low

frequencies, characteristic of 1/*f* noise. When frame differencing is performed, x[t]-x[t-2], long term drifts are subtracted from one another.

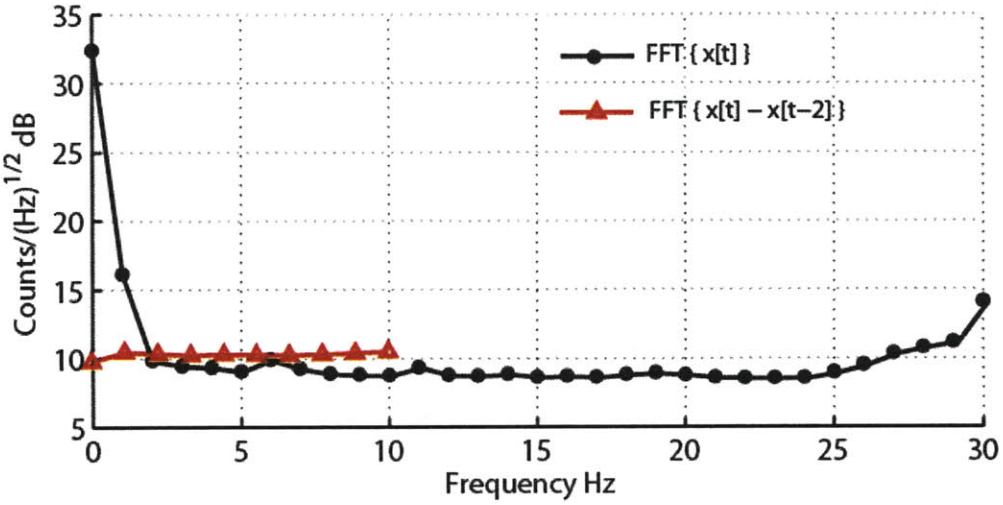

Figure 2-9 Fourier transform of microbolometer array signal with no input. Black trace shows 1/*f* noise characteristic for Fourier transformed signal x[t], which is not present in differenced signal (red trace). Signals shown up to their Nyquist frequencies.

2.5.2 Experimental Setup and Characterization

The imaging setup is shown again in Figure 2-10. The laser is indium soldered to a copper carrier, which is mounted in the cryorefrigerator. Due to the angular divergence of the emitted beam the device is placed as close as possible to the polypropylene cryorefrigerator window. An f/1, 50-mm diameter off-axis parabolic (OAP) mirror collimates the emerging beam, which is refocused by a second OAP (f/2), back-illuminating an object (an envelope in Fig. 1). Roughly 85% of the light at the window reaches the object, limited by the angle subtended by the first OAP. The transmitted light is imaged by an f/1, 25-mm diameter Si meniscus lens, through a Ge vacuum window onto the focal-plane array. A meniscus lens was chosen to minimize the center thickness, reducing the associated absorption losses. The transmission through the lens and window was improved by 20~40% by coating the surfaces with a thin sheet of polyethylene, which acts as an anti-reflection (AR) layer. The illuminated area in the object plane is roughly 3 cm × 3 cm, limited by the diameter of the first OAP. Also shown in Fig. 1 is

the modified reflection mode setup, where a specular reflection is collected by the repositioned Si lens and camera.

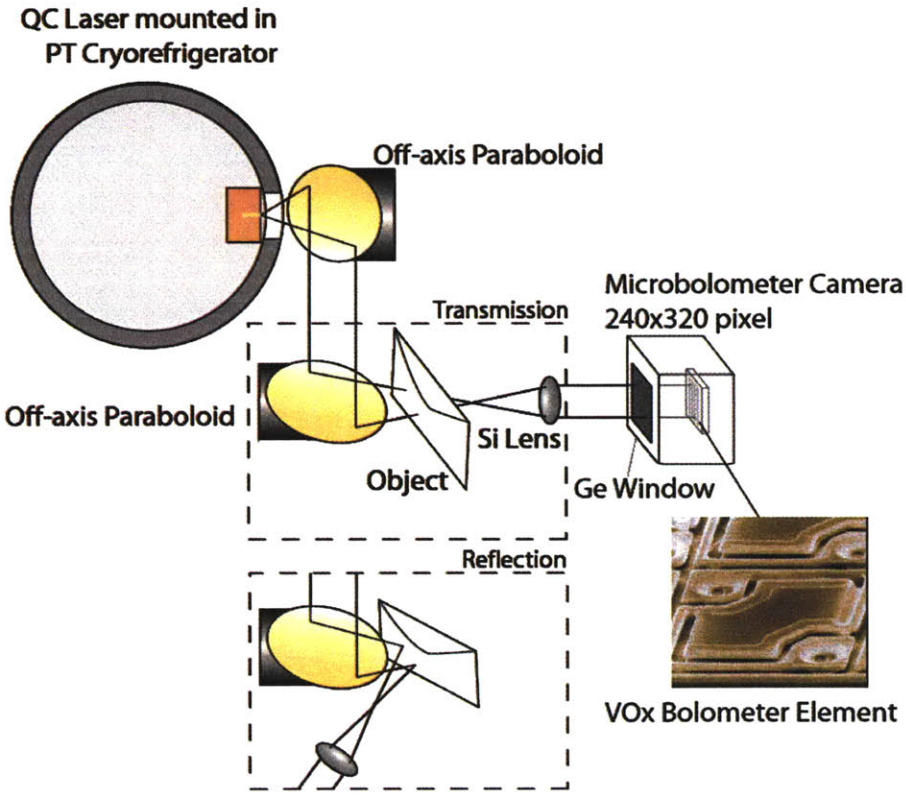

Figure 2-10 Experimental setup of the THz imaging system. The photo shows a vanadium oxide microbolometer (Courtesy of BAE Systems, Lexington, MA). Cutaway depicts alternate reflection mode setup.

Figure 2-11 part (a) shows the peak power, P, measured at the cryorefrigerator window using a thermopile power meter (ScienTech model AC2500H). The power decreases with pulse width due to active region heating in the QCL, which counteracts the benefit of the increased signal obtained with longer pulse widths. The pulse width is optimized for maximum differential signal by using the simple time constant model shown of Eq. 2-7, averaged over the focal plane. The optimum pulse width is ~ 13.5 ms, corresponding to the highest measured SNR of ~340 and ~550 with and without the Si lens respectively. We define SNR as the spatially and temporally averaged signal, $\langle x \rangle$, divided by the RMS noise, σ: $S/N = \langle x \rangle / \sigma$. Here σ is taken in a 20-Hz (single frame) bandwidth with the THz beam blocked.

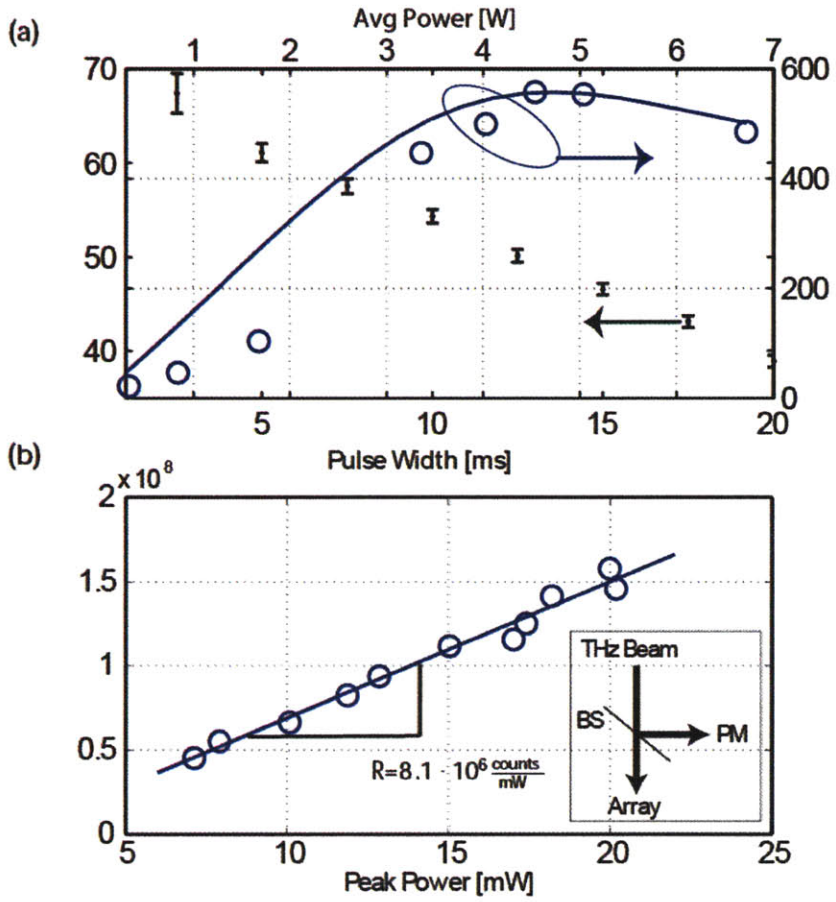

Figure 2-11 Part (a): Peak power and average signal-to-noise ratio vs. average power dissipation/pulse width. Solid trace represents normalized calculated SNR, circles represent measured single-frame SNR averaged over focal plane (without lens), and dots with error bars represent the THz laser power. Part (b): Total signal on focal-plane array vs. peak power. Right inset shows experimental setup: THz beam is beam split (BS) into a power meter (PM) and the focal-plane array.

The optical NEP_O at 4.3 THz – the incident power at which SNR is unity – is obtained from the previous expression by normalizing σ to a 1-Hz bandwidth (σ_{1Hz}~2.6 counts/ $\sqrt{\text{Hz}}$), and replacing $\langle x \rangle$ by the product of the NEP_O and a differential responsivity R: $S/N = 1 = \langle x \rangle / \sigma_{1Hz} = NEP_O \cdot R / \sigma_{1Hz}$. R is determined experimentally using the setup shown in the inset of Fig. 2 part (b) to measure the change of signal with respect to incident power – approximately 8.1×10^6 counts/mW. The incident power on the focal plane is measured using a beam-splitter, which requires a low bias on the QCL for single-mode operation,

as high biases cause multi-mode output, changing the beam-split ratio. The NEP_O is estimated to be $\sigma_{1Hz}/R \sim 320_{pW/\sqrt{Hz}}$ at 4.3-THz for this differential setup. This value is in reasonable agreement with a calculated value of ~200 $pW\sqrt{Hz}$ based on the electrical NEP_E of the microbolometers, modified for absorption/losses at the 70-μm wavelength and the differential scheme. At this long wavelength, absorption is estimated to be ~4% using a transmission line model, and the transmission through the Ge window is estimated to be 38% due to Fresnel losses and absorption. The differential process increases the noise by a factor of $\sqrt{2}$, and the microbolometer thermal time constant limits their temperature rise to ~42% of peak value.

2.5.3 Images

The ability of terahertz to see through common packaging materials is demonstrated by imaging the letters "MIT" written in pencil on the inside of a paper security envelope (~14 dB loss at 4.3 THz), shown at visible frequencies in Figure 2-12 part a. A single THz differential frame, obtained in transmission mode, is shown in part b. The same image is shown in reflection mode in part (c). In this image a 20-frame average is shown due to the weaker reflected signal. Because the signal is the result of a specular reflection, the half of the envelope covering the lettering must be wedged slightly to prevent a strong reflection from the first surface. It should be pointed out that this imaging application cannot be done using infrared frequencies as the envelope is opaque, and that imaging at millimeter-wave frequencies does not provide sufficient spatial resolution. A white-light image of an ink thumb print of the leading author is shown in part d, while the reflected THz, 20-frame average image of the thumb flattened against a polyethylene wedge is shown in part e. The distance between the grooves in the print are ~ 500 μm demonstrating high resolution capability.

While these still images are recognizable, when they are viewed in real-time the integration of the eye and pattern recognition of the brain aid tremendously as seen in real-time video. THz videos taken with the set-up described here can be found in [41].

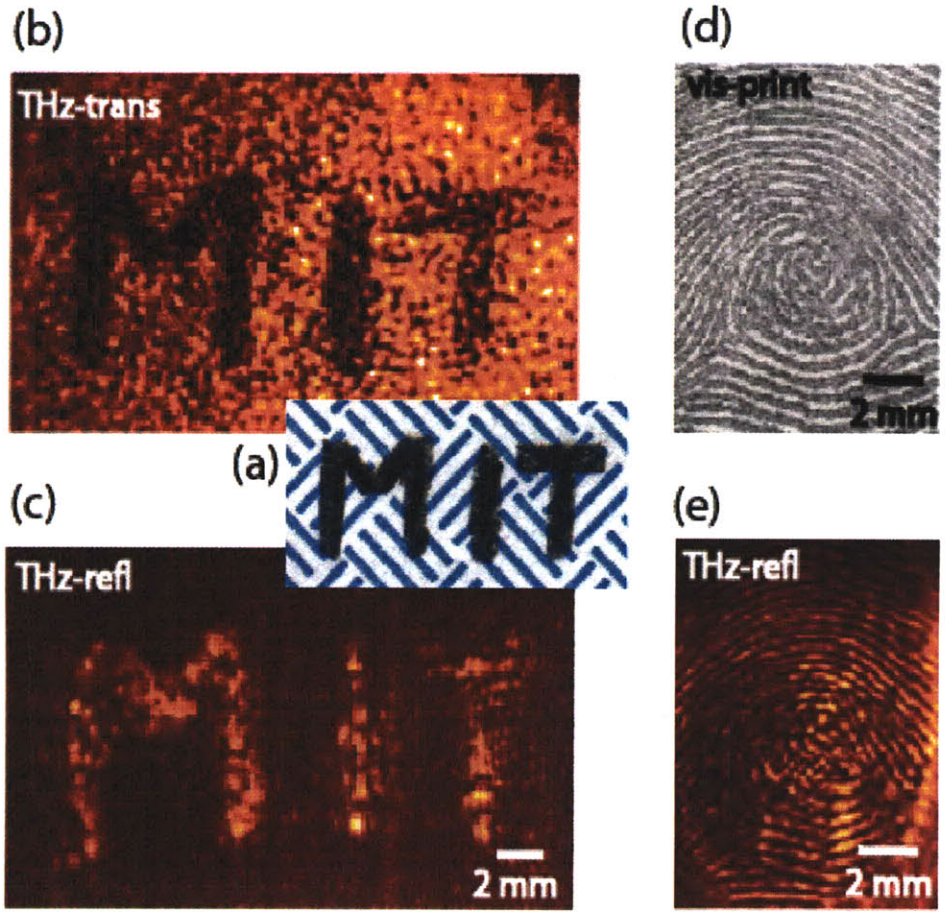

Figure 2-12 Pencil letters written on the inside of a paper security envelope at visible frequencies (a), in THz transmission mode (b, 1 frame) and THz reflection mode (c, 20 frames). Visible frequency thumb print (d), and THz reflection mode image the thumb of the leading author (e, 20 frames).

2.6 Atmospheric Losses

Water vapor can be strongly absorbing at THz frequencies, resulting in strong attenuation even over modest ranges. This attenuation exceeds >10 dB/m, outside of isolated low-loss transmission windows, which are only a few hundred GHz wide. These narrow transmission bands favor the use of narrowband sources for which the QCL is ideally suited. In this section we demonstrate the use of a frequency optimized THz QCL for real-time imaging in transmission mode over a distance of 25.8 meters, serving as a proof of concept experiment.

In order to develop the long-range capability of THz imaging, it is important and instructive to analyze the effect of several laser characteristics, most importantly the output power level and frequency, on the power received at the end of the standoff range. Because of the exponential decay of transmitted power through space, for a given minimum detectable power, the incremental distance Δl between the transmitter and the detector changes only *logarithmically* with the power available at the transmitter, $\Delta l=(10 \log N)/\alpha$, where N is the N-fold increase in power and α is the atmospheric attenuation coefficient in dB/meter. The frequency dependence of α is shown in Figure 2-13, and it changes rapidly and non-monotonically in the THz range, often varying by several dB/meter over a span of ~0.1 THz. For typical values of α at THz frequencies ranging from 0.5 to 10 dB/meter, a ten-fold increase in power yields diminishing increases in range from 20 to 1 meter. Again, because of the exponential decay, a small change in α will result in a significant change of the transmitted power over a long distance. Numerically, the relative transmitted power over 25 meters is 0.32% for α = 1 dB/meter, but 5.6% for α = 0.5 dB/meter. This straightforward but important analysis dictates that for long-range THz imaging, the frequency of the transmitter is much more important than its power, as long as adequate power levels (>10 mW) are available.

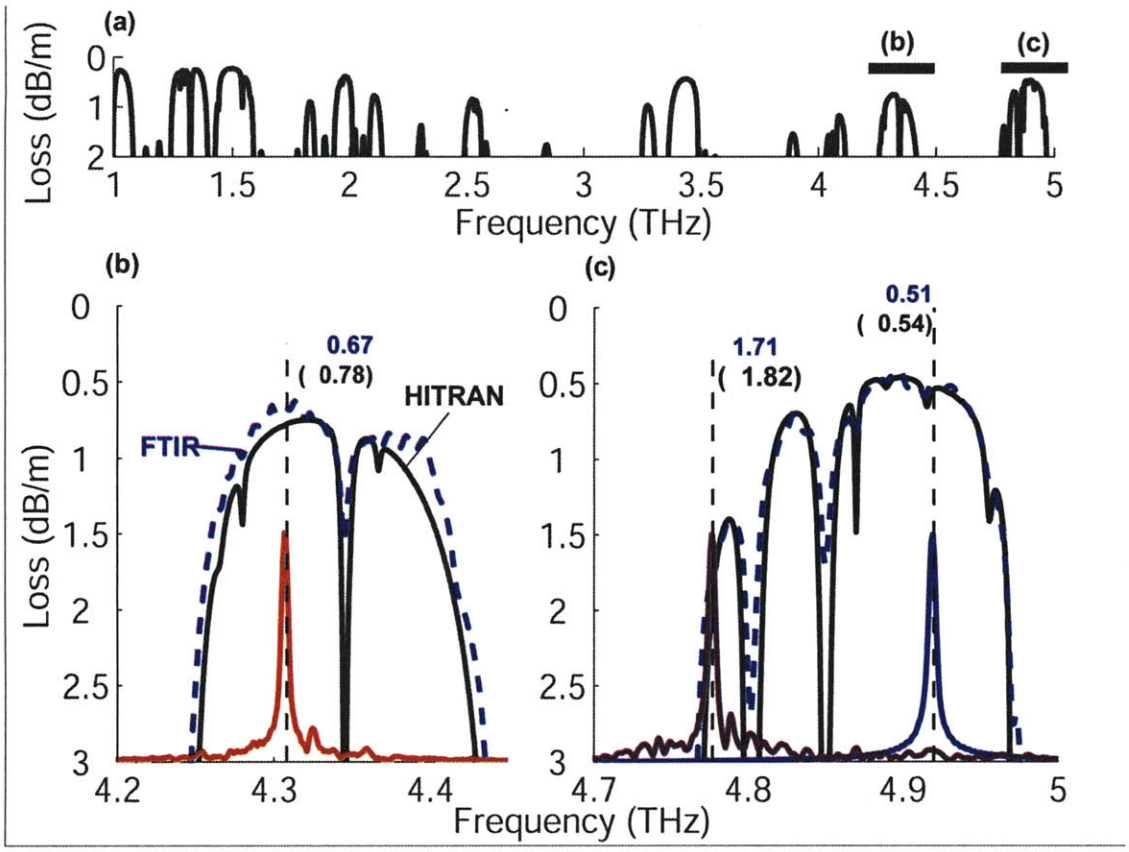

Figure 2-13 Atmospheric path loss in dB/m, measured by FTIR (dashed) and calculated from HITRAN 2004 (solid) at 296 K and 40% relative humidity for continuous frequency range of 1 to 5 THz (part(a) calculation only), and 4.3 and 4.9 THz windows (parts (b) and (c)). Path loss indicated at lasing frequencies of several selected QCL devices, FL183R-2 (4.3 THz (red), 98 μm × 2.15 mm), and FL179R-2 (4.77 THz (purple) 100 μm × 3.05 mm, and 4.9 THz (blue) 100 μm × 1.97 mm).

Here we focus on the frequency range of 4-5 THz, in which there fabricated QCLs with the high output power levels [46, 54]. The aforementioned high-power laser at ~4.3 THz has produced adequate results in real-time imaging over a distance of ~10 meters. However, the quality of the imaging degraded noticeably at the longer 25-meter range. Upon a close inspection of Figure 2-13 part (b) and (c), it is clear that the atmospheric window at ~4.9 THz has lower attenuation, and therefore is more desirable for long-range imaging. Quantitatively, the measured atmospheric attenuation are 0.51 dB/meter and 0.67 dB/meter, at 4.92 and 4.31 THz respectively. While these attenuations cause comparable losses over short ranges, they increase exponentially with distance. For example, at ranges of 25 and 100 m, the 4.92 THz window results in 2.5 and 40 times more transmitted power respectively. Furthermore, α increases linearly with the absolute humidity and thus at higher humidities these differences become even greater.

Atmospheric transmission measurements were taken by FTIR with a resolution of 3.75 GHz, in the lab environment of 296 K and 40% relative humidity (RH), over a 1.3 m path length using a 1000 K SiC blackbody source with a deuterated triglycine sulfate (DTGS) detector. The amplitude was normalized to a spectrum taken under nitrogen purge. These values are compared in Figure 2-13 with calculated values from the HITRAN 2004 database[72] under the same conditions, modeling atmospheric water ($H_2{}^{16}O$, 99.7% abundant), with additional THz transmission windows shown from 1 to 5 THz.

The device used in this work is labeled FL179R-M1 and is similar in design to the 4.3-THz, high-power device described in sections 1.6 and 2.4 (labeled FL183R-2, spectrum shown again in Figure 2-13). The primary design difference between FL183R-2 and this device, FL179R, is the thinned barrier between the n = 5 and n = 4 upper and lower radiative states, from 17 Å to 15.5 Å. Thinning of the so called "radiative" barrier, has the effect of increasing the energy separation (anticrossing) between the upper and lower radiative states to 20.3 meV (~4.9 THz) at design bias. In order to reduce the parasitic current channels that occur at lower biases, this design also has a thickened inter module ("injector") barrier from 48 Å to 54 Å, which resulted in a reduction of the threshold current density. However, this thicker injection barrier also reduced the maximum current density and yielded a lower power level (by a factor of ~3) from FL183R-2. The active region was grown by molecular beam epitaxy and processed into semi-insulating surface plasmon Fabry-Pérot ridge waveguides of various geometries using dry etching, with the rear facets high-reflectivity coated.

A number of devices with a width of 100 μm, and lengths from 3.05 to 1.97 mm-long were tested. The ridge width was chosen to optimize peak optical power output while maintaining efficient heat removal laterally through the substrate. A continuous-wave (cw) spectrum of a 3.05-mm long device is shown in Figure 2-13, and is typical of the longer devices, which emit near ~4.77 THz. As shown in Fig. 1(c), the atmospheric attenuation at this particular frequency is quite high (~1.8 dB/m). In order to shift the lasing frequency to the desired ~4.9 THz, devices with higher optical losses were deliberately chosen in order to achieve higher lasing thresholds. Shorter lengths were

used in order to increase the facet loss, $\alpha_m = -\frac{\log(R)}{L}$ where R is the 32% reflectivity of the SISP facet. The increase in loss results in a higher electrical bias at lasing threshold, and a concomitant blue Stark shift of the gain spectrum. The Stark shift, or emission frequency change with applied voltage, is a result of the n = 5 and n = 4 levels being distributed over two quantum wells, whose energy separation increases with bias. The cw spectrum of the 1.97-mm long device is shown in Fig. 1, emitting around 4.92 THz which is quite close to the optimum frequency in the ~4.9-THz window.

The 1.97-mm long device produced a cw power of 38 mW at 9 K as measured with a thermopile detector (Scientech, model AC2500). At ~30 K, the cryocooler temperature, the device produced a peak pulsed power of ~17 mW using 13.5 ms long pulses at 27% duty cycle. The use of a shorter device resulted in a small reduction in power, from 18.5 mW to 17 mW, due to an increase in the threshold and a smaller device size, for the 3.05 and 1.97-mm long devices respectively. However, this lower power is more than compensated for with increased atmospheric transmission.

An experimental demonstration of long distance transmission through the heavily attenuating atmosphere using a QCL tuning the a narrow transmission window is shown in Figure 2-14. The QCL was indium soldered to a copper carrier, and mounted in the cryocooler. The emitted light was collected and collimated by an f/1 off-axis parabolic mirror with a 5-cm diameter. Four plane mirrors (shown in part b) were used to fold the optical path and to direct the beam to a 15-cm diameter spherical mirror, tilted off the optical axis to prevent subsequent optical elements from obscuring the beam. In configuration (1), an f/3, high-resistivity Si lens was used to focus the light transmitted through an object placed at 2 meters in front of the spherical mirror, onto a 320×240 microbolometer focal plane array. Note that in the object plane, which is ~23-meters from the laser source, the beam pattern is highly symmetric as measured by the focal-plane array camera with 1-second integration time. In configuration (2), the reflected beam from the spherical mirror was further focused by an f/2 off-axis parabolic mirror and was used to back illuminate a smaller object. Transmitted light was collected and focused by an f/1 high-resistivity Si lens onto the focal plane array.

a)

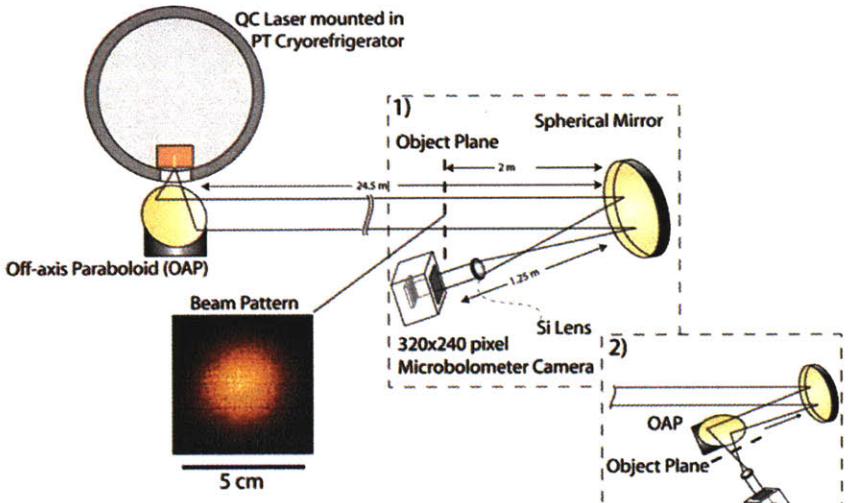

b)

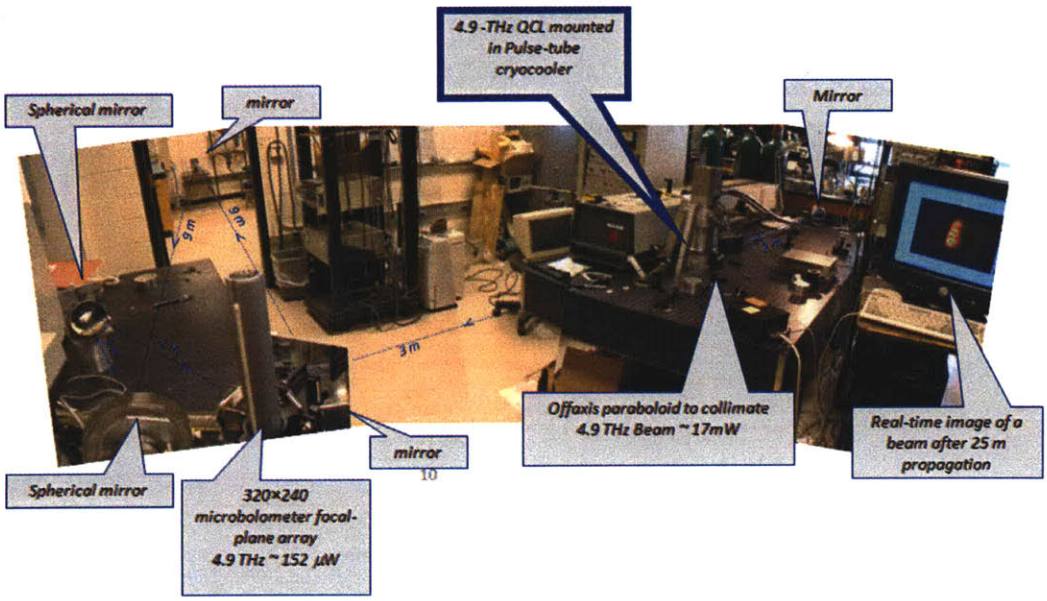

Figure 2-14 Part (a) schematic of experimental setup for imaging over a distance of 25.75 meters. A QCL device is mounted in a pulse-tube cryocooler, with emitted beam collimated by an off-axis paraboloid mirror, for transmission over a 24.5-m path before collection by a 15-cm diameter spherical mirror. In configuration (1), an object is placed 2 meters before a spherical mirror; in configuration (2), an object is placed after a second off-axis paraboloid mirror. Also shown is the beam pattern for configuration (1), measured at ~23 meters from the laser source and taken with a 320x240 element focal-plane array camera with 1-second integration. Part (b) image showing physical layout of long distance imaging setup. The large number of optical folding mirrors are necessary to obtain the 25 m distance within the lab space. Mirrors are preferred for folding and for focusing due to their low loss at terahertz frequencies relative to dielectrics.

The resulting images are shown in Figure 2-15. A dried seed pod is used as the see-through object. In part (a) a white light image of the dried seed pod is shown, with the

corresponding THz transmission images shown in parts (b) and (c) for configurations (1) and (2) respectively. After transmission over the 25.75-m path, the resulting focal-plane average SNR was ~2.5 and 10, for a single-frame and a 20-frame average (0.05 and 1 second of integration, respectively) respectively. The 20-frame average images shown in (b) and (c) were normalized to the beam pattern and were spatially low-pass filtered to smooth out isolated pixels with low SNR. This post detection signal processing is performed in real time, and only adds a ~5-ms delay in displaying the images. The image in part (b) has low spatial resolution due to the 2-meter distance from the spherical mirror, with a calculated resolution of ~3 mm at the object plane using ray tracing software (Code V, Optical Research Associates). Part (c) shows a much higher spatial resolution, due to the closer positioning of the object to the camera. As a result, the fine ridges of the seed pod (~millimeter spacing) can be resolved, as predicted by the ray tracing resolution of ~0.75 mm.

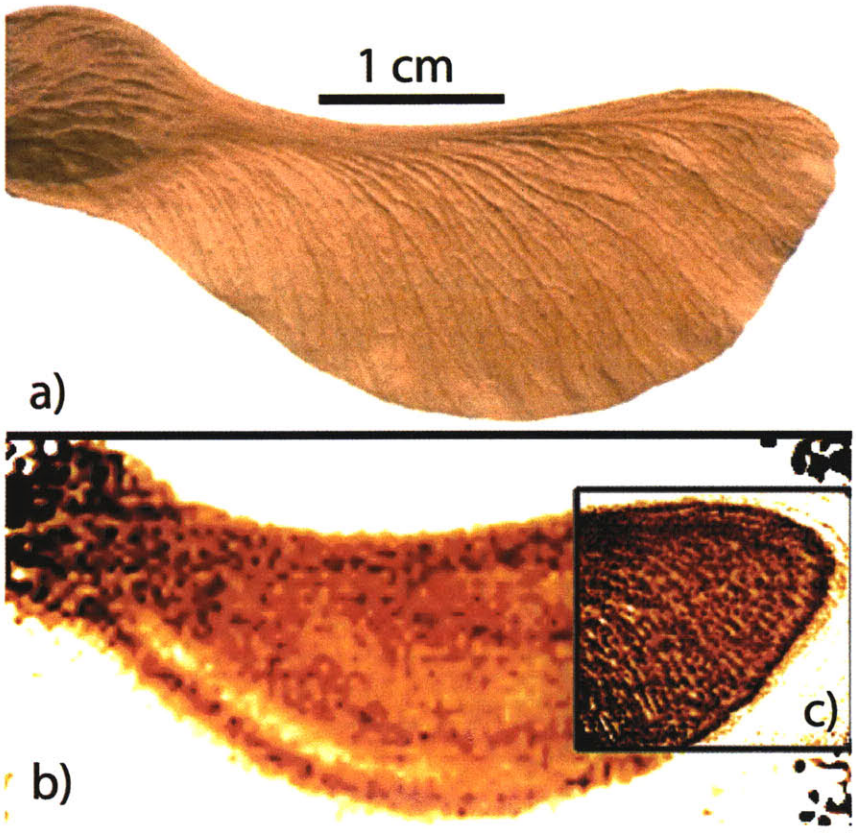

Figure 2-15 Sample images of a dried seed pod: (a) image at visible frequency; (b) terahertz image taken with configuration (1); (c) terahertz image taken with configuration (2). Both (b) and (c) are taken with 1-second integration (average of 20 frames).

The beam propagation losses were measured using optical configuration (1) with a shorter 10.1 m path, to allow the use of the thermopile detector with a sufficient SNR. The thermopile was used at the focal point of the 15-cm mirror, without a Si lens. Power measurements were taken immediately after the OAP, and after the 10.1 m path. The propagation loss was determined to be 0.79 ± .03 dB/m, somewhat larger than the predicted loss of 0.52 ± .05 dB/m, which was calculated using the experimental conditions of 292 K and 48 ± 5 % RH. Some of these losses were likely due to divergence of higher-order spatial modes, whose power was included in the measurement after the first OAP. In fact, the beam pattern measured immediately after the first OAP is far less symmetric than that shown in Figure 2-14, indicating that most of the higher-order spatial modes have been "filtered out" after a long distance (>10 meters). Additional losses were likely due to imperfect mirror reflectivity of the four folding mirrors and absorption by the protective coating of the 15-cm spherical mirror.

Using the calculated path loss of 0.79 dB/m, it is estimated that ~150 μW reaches the object after ~25.8 meters, which is still sufficient for penetrating the dried seed pod for imaging with the microbolometer camera. Optimization of the microbolometer camera specifically for THz frequencies could reduce the optical noise equivalent power (NEP) and thus improve SNR by two orders of magnitude, from ~320 pW/√Hz to several pW/√Hz that is close to its measured electrical NEP of ~1 pW/√Hz. Exponential improvements can be made by utilizing atmospheric transmission windows at lower frequencies, most notably the ~1.5 THz window (~0.23 dB/m at 296 K and 40% RH), which has the lowest absorption in the 1-5 THz range. The lower frequencies are also beneficial for better penetration of optically dense materials such as clothes and leaves.

3 High-Power QCLs Using Lens Coupling

3.1 Introduction

Thus far, the desirable high power levels and narrow beam patterns (12°, full-width at half maximum, FWHM) have been obtained from QCLs using semi-insulating surface plasmon (SISP) ridge waveguides, a result of their spatially extended transverse mode profile (confinement factor $\Gamma \approx 0.1$—0.5). This produces a low divergence beam as seen in Figure 2-7, as well as a low reflectivity ($R \approx 0.32$) output facet, making mirror losses α_m comparable to waveguide losses α_w, resulting in high slope efficiencies, $dL/dI \propto \alpha_m/(\alpha_m+\alpha_w)$ and correspondingly high output power levels [56]. However, these benefits result in a tradeoff with higher threshold current densities (J_{th}) caused by greater waveguide losses. Due to these additional losses, operation of SISP devices is limited to temperatures below 105 K (see appendix A for a more detailed description of this argument based on numerical simulations of SISP waveguides) [54].

In comparison, metal-metal (MM) waveguides have a near unity confinement factor ($\Gamma \approx 1$) due to the highly confined mode propagating between the two metal strips; this essentially eliminates the additional loss from substrate absorption. The subwavelength confinement results in divergent beam patterns exceeding 180°, and enhanced reflectivity at the end-facets ($R \approx 0.7 - 0.9$, $\alpha_m \approx 0.5 - 2$ cm^{-1}) [56, 57, 73]. The additional reflectivity is due to a modal mismatch between the confined surface plasmon mode (attached to the closely spaced metal strips) and the near-field modes at the aperture, resulting in lower J_{th}, and high maximum operating temperatures (T_{max}) of 186 K [53]. However, since α_m is small compared to α_w, these devices typically have lower slope efficiencies and power levels of 10's of mW. A strategy to increase α_m with minimal impact on T_{max}, is to pattern a second-order distributed feedback grating in the top metal strip for surface emission [51, 74, 75]. These devices improve measured slope efficiency by reducing beam divergence in the grating axis, improving collection efficiency (η_{col}), resulting in ~10 mW power levels and single-mode operation.

3.2 Lens-coupled metal-metal waveguides

As an alternative, a Fabry-Pérot MM waveguide with a dielectric lens (Figure 3-1) can be used to improve the beam pattern. In this work, silicon (n_{si}~3.4) – which is nearly index matched to the GaAs/AlGaAs active region (n_{GaAs}~3.6) – is placed in contact with the output facet to increase η_{col}. The enhancement results from increased radiation in the forward direction due to the presence of the dielectric [76]. Analogously, slot antennas on dielectric substrates radiate power into air and the substrate in the ratio $1:\varepsilon_r^{3/2}$. While the MM waveguide is not identical to a slot antenna, similar enhancements in directivity are expected in the patterns observed in [57] and [73]. Further enhancement is obtained by increasing the beam directivity with the lens. This approach leads to higher powers and better beam patterns without significantly reducing T_{max}, in contrast to SISP devices.

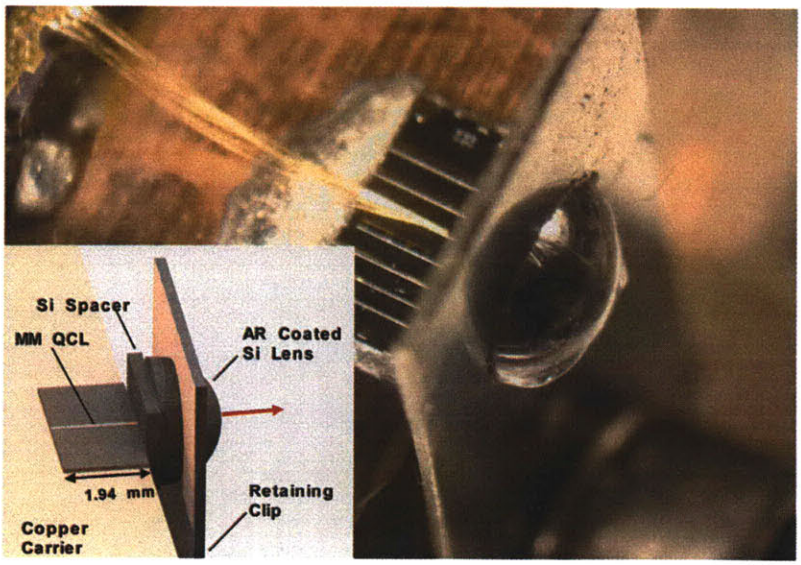

Figure 3-1 Metal-metal THz QCL with abutted HRSi spacer and lens

The device is based on the resonant-phonon depopulation design and uses the same active region described in section 1.6 [51, 54]. The MM waveguide was fabricated using the wet-etching processing described in [74], with the waveguide oriented so that the facets could be defined by cleaving. An 80 μm-wide by 1.94 mm-long device was aligned and indium soldered to a copper carrier so that the output facet was flush with the carrier edge, allowing a double-side polished, 340 μm-thick, high-resistivity silicon (HRSi, >10

KΩ-cm) spacer to be epoxied to the carrier and remain in contact with the facet. Close positioning of the spacer was critically important, with similarly sized devices producing <100 mW, likely due to gaps between the facet and the spacer (effect discussed in section 3.3). Good contact between the spacer and the facet was achieved by using a die bonder tip to push on the spacer during epoxy curing. The fixed spacer provided a mating surface for the HRSi lens, preventing damage to the facet during lens alignment. The lens has a 3-mm diameter and a total length of 1.62 mm, making the total setback from the center 0.46 mm, roughly at the *R/n* aplanatic point [77]. To reduce reflections at the lens surface, the lens was anti-reflection (AR) coated using a ~14 μm-thick layer of low-density polyethylene (LDPE, $n \approx 1.5$) which acts as a quarter-wave matching layer at the lasing frequency of 4.1 THz. In a separate measurement, a single side of a flat HRSi wafer was coated with this film, improving transmission by ~30% (from 49% to 63% through the wafer). A transmission of ~90% is then deduced for the Si/LDPE/Air interface ($0.9 \approx 1.3 \times 0.7$ where 70% is the transmission of the Si/Air interface).

The lens was positioned against the spacer, and held in contact by a spring steel retaining clip. The position of the lens with respect to the facet was adjusted using fine set screws at room temperature by dissipating heat pulses in the device (Figure 3-2, shown for a similar metal-metal waveguide device with a 200 μm wide facet), and imaging the facet onto an infrared microbolometer camera operating in differential mode (see section 2.5.1). Though a relatively high average power of 0.5 W was dissipated in the device, a real-time thermal image was not possible due to the high thermal conductivity of the metal-metal waveguide. The resulting thermal image, shown in part (b), was taken over 5 minutes of integration (~6000 differential frames) in order to reduce the noise making a small temperature differences more apparent. This thermal alignment procedure allowed fine alignment of the lens with respect to the laser facet, prior to cryogenic laser operation.

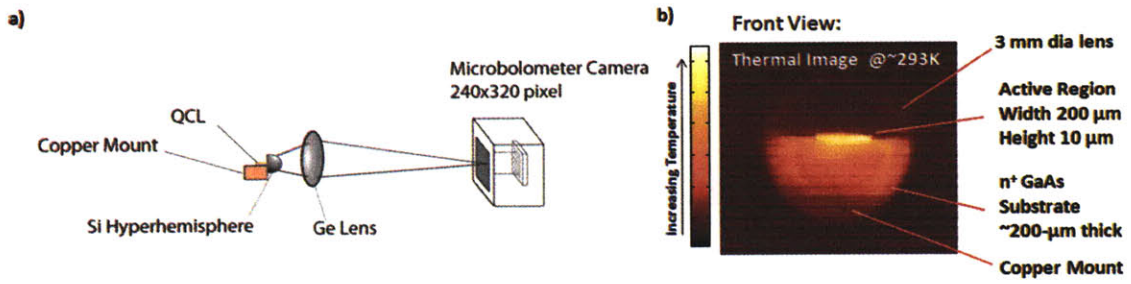

Figure 3-2 Part (a) shows room-temperature hyperhemispherical lens alignment setup. Heat pulses are applied to a device and synchronously detected using scheme from 2.5.1. Part (b) shows resulting thermal image of aligned 3-mm diameter lens with respect to heated 10 × 200 μm^2 device facet. The magnification of hyperhemispherical lens increases the apparent size of the facet relative to the lens.

After alignment, the device was mounted in a vacuum cryostat with a polypropylene window and biased with 200 ns pulses repeated at 50 KHz for a total duty cycle of 1%. The output power was measured versus current (Fig. 2) using a pyroelectric detector, with the peak power calibrated with a thermopile power meter (ScienTech model AC2500H). At 5 K, J_{th} = 266 A/cm^2 with a maximum peak power of 145 mW lasing up to 160 K. The slope efficiency was *dL/dI*=296 mW/A near threshold, and was 140 mW/A at the peak, with a maximum wall-plug power efficiency of 0.7%. For comparison with an open facet, the lens and spacer were removed and the device was tested using a Winston cone to collect the emitted power. At 5 K, J_{th} = 254 A/cm^2 with a peak power of 26 mW, lasing up to 165 K. Due to a thermal runaway problem of the MM devices fabricated from this wafer, several devices failed catastrophically in CW operation [51]. As a result, all pulsed measurements (with and without the lens) were concluded before attempting CW measurements. After remounting the spacer and lens, the device produced a peak power of 102 mW with 2 μs long pulses at 25% duty cycle before failing. This failure was not associated with the lens set-up. Similar lens-coupled MM devices fabricated from a different wafer (FL179C-M9-2, lasing at ~2.7 THz) yielded ~50 mW of CW power.

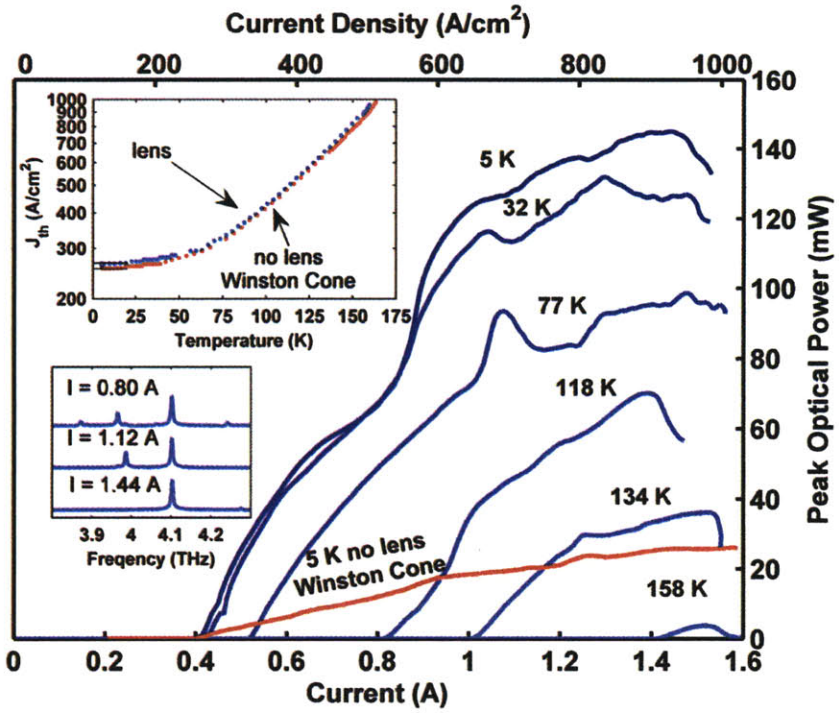

Figure 3-3 Light vs. current: lens-coupled and Winston cone-coupled devices. Insets: (upper) J_{th} vs. temp.; (lower) typical spectra of device with lens

An expression for the measured slope efficiency is $\eta_{col} \cdot \alpha_m/(\alpha_m+\alpha_w)$, with the observed change in slope efficiency (5.5×) resulting from increases in η_{col} or α_m. The small difference in J_{th} and T_{max} suggests a small increase in α_m since J_{th} should increase with $(\alpha_m+\alpha_w)$. However, deduction of α_m is hampered by the unknown transparency current and hence gain-current relation in the resonant-phonon gain medium, as a parasitic current channel below the designed bias sets the transparency current density substantially different than zero [78]. A larger influence is expected from improved η_{col}, which is estimated numerically for bare-faceted and lens-coupled devices (Fig. 3). A full-wave simulation is used to determine the far-field patterns for the front and rear facets of the bare and lens-covered devices. For the lens-coupled device an HRSi halfspace is assumed for the front facet covering, as the lens/air boundary is ~70 λ_{si} from the facet. A superposition of the front and rear far-field patterns (in the forward direction) separated by the device length is then used to model the far-field pattern of the device. Collection efficiency is determined using the collection angle of the bare facet, which is ~15° limited by the aperture of the power meter (29-mm dia., 55 mm from the device). For the lens-coupled facet the collection angle is $\beta_{max}=\sin^{-1}(r \cdot \sin(\gamma)/sb) \sim 70^\circ$ (set back, sb = 0.46 mm)

limited by critical angle (γ) at the lens/air boundary, which is unaffected by the AR coating. Though this beam pattern model is simpler than [73], when applied at the wavelengths and device dimensions of [57] the interference fringe separation agreed with the measured patterns. This analysis precludes the use of a Winston cone because the cone is optically close (~3.5 λ_o ~ 250 μm) to the front facet, making the use of far-field ray tracing unjustified. Moreover, the entrance aperture of the Winston cone is computationally large ~26 λ_o (1.9 mm), preventing a three-dimensional full wave simulation. However, the relative improvement in η_{col} of the Winston cone over the bare facet is determined experimentally to be 4.3×, which allows a comparison of Winston cone and lens-coupled configurations. For the fundamental lateral mode (mode 0), $\eta_{col}\approx$3.5% for the bare facet and reduces slightly for higher order lateral modes due to increasing divergence. The lens greatly enhances forward radiation (i.e. improved directivity) and results in a dramatically different beam pattern, $\eta_{col}\approx$62%, and improves the slope efficiency by ~16×, including the transmission of the AR coating. Including the improvement of the lens on the Winston cone (5.5×), the overall lens to bare-facet improvement is ~23×, reasonably agreeing with the numerical results.

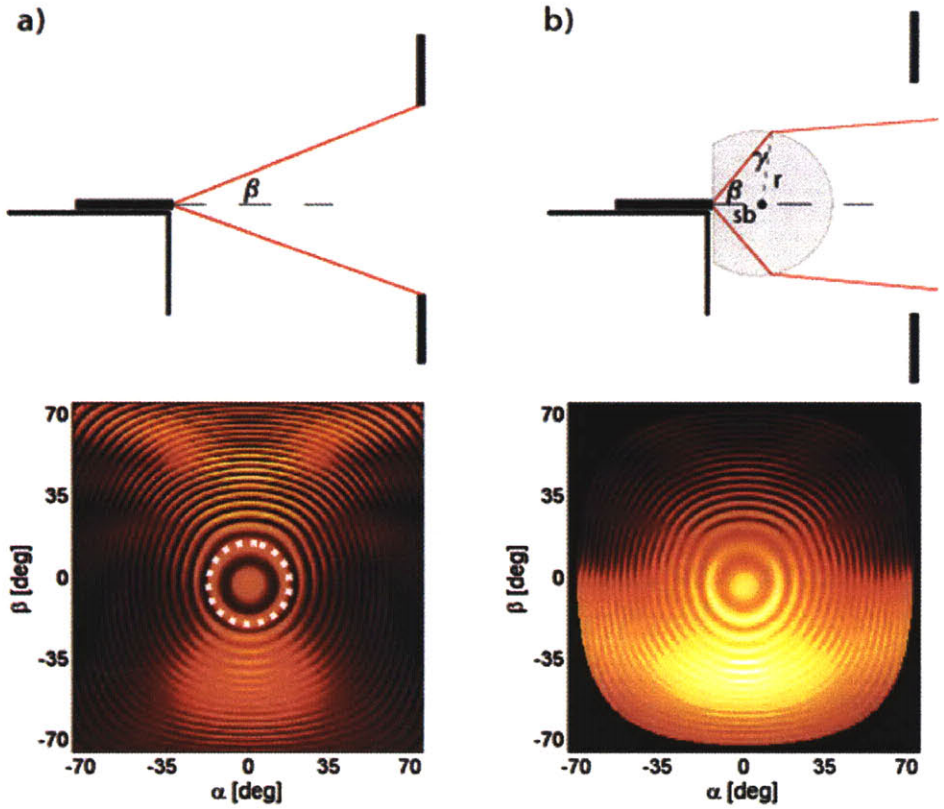

β_{max}	η_{col} – Mode 0	η_{col} – Mode 2	η_{col} – Mode 4
15°	3.5% (16×)	2.5% (22×)	2.1% (23×)

Figure 3-4 (Top) Collection angle (β): bare facet (a); lens-coupled (b). (Middle) Calculated beam pattern: bare facet (a, collected power circled); lens-coupled (b, into HRSi, uncollected power blackened). (Bottom) Collection efficiency of bare facet for even lateral modes; expected relative improvement of lens-coupled facet in brackets.

To verify the high directivity of the lens-coupled configuration, the FWHM of the beam was measured in the H-plane using a rotation stage and a pyroelectric detector (12 mm aperture) placed 30 cm from the device. Both the far-field beam pattern and a cross-section of the beam pattern from the microbolometer camera have a FWHM $\approx 4.8^{\circ}$ (Fig. 4). Diffraction patterns in the beam image at 6 cm are likely due to spurious reflection off the cryostat window and/or unevenness of the AR coating, however these patterns disappeared in the far field. In conclusion, our work demonstrates that careful optical engineering of lens-coupled metal-metal waveguide THz lasers can produce high power levels with good beam patterns, while preserving their advantage of higher T_{max}.

3.3 Facet Reflectivity

The decrease in maximum operating temperature and increase in J_{th} are small in scale compared to the SISP device, suggesting that that decreased reflectivity is a minor effect. The effect of the spacer on the facet reflectivity was investigated using finite-element simulations with geometry similar to [56]. Large variations in power were observed for similarly sized devices, and it was suspected that small gaps might exist between the facet and the spacer. To model this effect, the reflectivity is plotted against this air gap distance for the fundamental and first two even-symmetry lateral modes (Figure 3-5).At larger gap distances, the effect of the spacer is reduced, and the reflectivity of the fundamental mode approaches 74%, which is the open facet reflectivity calculated in ref. [56]. At the zero gap distance the facet reflectivity is reduced below 10% due to the elimination of dielectric mismatch, and the reduction of the wavelength outside the cavity, λ_o/n_{Si}, which eases modal mismatch. SEM images of various MM waveguide facets revealed micron scale protrusions resulting from tearing of the top and bottom metal strips during cleaving. Thus, small gaps are unavoidable for facets that are defined by cleaving and act to limit the reduction in reflectivity.

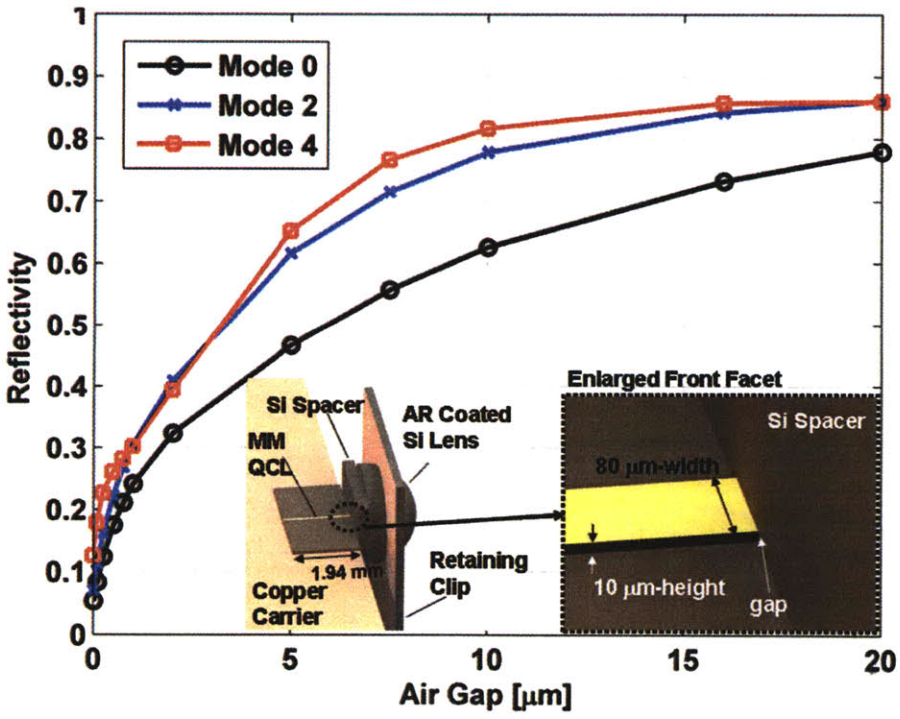

Figure 3-5 Output facet reflectivity of a metal-metal waveguide (80-μm wide and 10-μm high) with a high-resistivity Si spacer placed at various air gap distances

A larger effect on the enhancement of power is expected from improved collection efficiency by the presence of the dielectric. For antennas fabricated on thick, high ε_r substrates, the ratio power radiated into air and the substrate is $1:\varepsilon_r^{3/2}$ for slot and dipole antennas [76]and a similar effect is expected with the spacer covered facet. Using finite element simulations to model the radiation patterns of the bare and covered facets, the improvement in collection efficiency between the lens-coupled and bare-faceted devices for the fundamental lateral mode was calculated to be 16×. The observed improvement in power between the lens and the Winston cone, and the Winston cone and bare facet are 5.5× and 4.3× respectively, giving an overall improvement of the 23× for the lens over the bare facet. This improvement factor includes the effects of collection efficiency and decreased reflectivity and was in relatively good agreement with the numerical results.

The low beam divergence of the lens-coupled MM waveguide QCL is apparent in the measured beam patterns (Figure 3-6, (a) and (b)). The beams were measured in the H-plane of the far-field (30 cm), and had a full-width at half-maximum of 4.8°, with the full beam pattern measured with a microbolometer camera at a distance of 6 cm (b).

These low divergence beam patterns allow nearly all of the emitted power to be collected in an f/1 optic, external to the cryogenic dewar, whereas ~85% of the power can be collected using the SISP device and even less with a bare-faceted MM device. This large amount of collected power allows the use of a spatial filter to improve the beam pattern (c), which is useful for even illumination in imaging or in coupling to the single-mode antennas used in heterodyne detectors. The pattern in (c) was produced by a smaller (80 μm-wide, 1.2 mm-long) lens-coupled MM devices fabricated from a different wafer (FL179C-M9-2, lasing frequency at ~2.7 THz) yielding ~50 mW of CW power at 30 K in a closed cycle cryorefridgerator, and had 7 mW after filtering. This high CW power at 30 K is equivalent to the performance of the larger FL183R-2 SISP device at this temperature [54],demonstrating the benefits of this technique. Comparison of CW power with the lens-coupled FL183R-2 device was not possible as the device failed due to thermal runaway (not associated with lens setup) during high duty cycle testing. Prior to failure it produced 102 mW with 2 μs long pulses at 25% duty cycle.

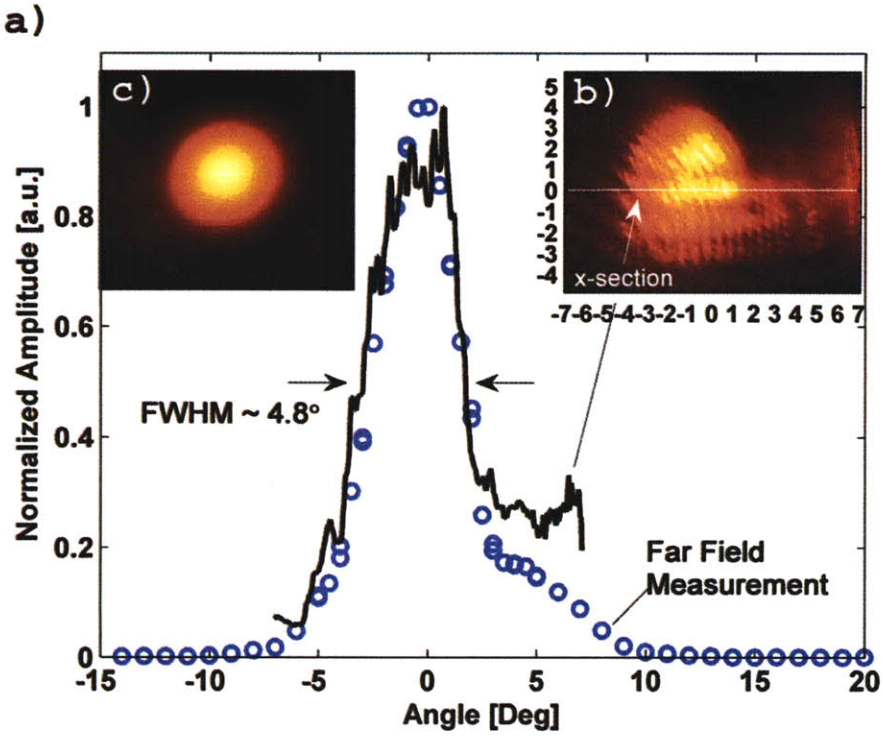

Figure 3-6 Far-field beam pattern in H-plane of lens-coupled QCL (FL183R-2). Part (b) shows beam pattern measured by focal plane array, with H-plane cross-section marked by white line. Part (c) shows beam pattern of 2.7 THz lens-coupled QCL after spatial filtering with a 3mm aperture

The lens-coupled MM device has combined the key features of both SISP and MM waveguides: it produced a peak power of 148 mW over short laser pulses, within a factor of 2 of the highest power QCL, with a maximum operating temperature of 160 K, which is <10 K below the highest reported operating temperature [53], while maintaining a narrow beam width of 4.8°. Future improvement of the lens-coupling should improve optical powers with larger reductions in operating temperature.

4 Tunable External Cavity Terahertz Quantum Cascade Lasers

Tunable lasers have been described as a "wrench of wavelength," for their ability to provide high power spectral densities at precise wavelengths, obviating the need for wavelength measurement – making them useful general purpose devices [79]. These properties are desirable in imaging applications where the spectroscopic information can be converted to depth information as in the case of swept source optical coherence tomography [80, 81], or the spectroscopic information can be used to identify gases by their narrow spectral features (~MHz) [47, 72, 82] or solids by their broad spectral features (>100 GHz) [17, 18, 83]. In all applications high output power levels are desirable as the signal-to-noise ratios scale with the power of the source [84], and larger tunable bandwidths are desirable for greater depth resolution and analytical capability. Single mode operation (lasing at a single frequency) is also highly desirable as it reduces ambiguities in spectroscopic analysis and in depth measurement. With these criteria in mind, several approaches have been taken to create tunable lasers at terahertz frequencies.

4.1 Previous Work

A variety of methods of manipulating the index of refraction of the active region of single mode devices have been used to affect a small amount of tuning. Thermal tuning can be achieved by increasing the temperature of the active region of a QCL, resulting in a small increase of the index of refraction, causing proportional red shifts of frequency. For distributed feedback (DFB) lasers where the lasing frequency is essentially determined by the grating period, small frequency shifts of <20 GHz (0.7% of the central frequency) for large temperature changes of >100 K have been reported [74, 85]. Similarly, by increasing the current through a Fabry-Pérot device, Joule heating can be used for fine control of the frequency and has been demonstrated in a frequency locking scheme [86].

Similar amounts of tuning have been observed from the cavity-pulling effect, where the index of refraction is instead affected the gain of the device. A small amount of tuning is observed in microdisk resonator structures, which show 30 GHz (fractional tuning 0.85% of the central frequency), reported in [87, 88]. While either of these techniques could potentially be used for spectroscopy of gasses they are not suitable for spectroscopy of room-temperature solids where tuning of over 100 GHz is necessary, or for depth measurement where bandwidth is inversely proportional to resolution.

For this broader tuning, an external cavity QCL (EC-QCL) with frequency selective feedback is typically used and several initial efforts (Figure 4-1) have resulted in mixed success. The common elements of the EC-QCL approach include an anti-reflection (AR) coating applied to the gain medium/air interface to prevent/reduce reflections, and strong external feedback using a reflective element such as a grating or mirror. The first experiments in tuning EC-QCLs had limited success due to a lack of high quality AR coatings at THz frequencies, resulting in the inability to suppress the optical feedback from one of the gain medium facets, which are typically defined by cleaving, and must compete with the feedback from the external reflector [89]. These AR coatings were formed by angle polishing the gain medium at an angle, θ_F, of 13° which approaches the Brewster angle, 15.1° ($n_{GaAs} \approx 3.7$), but does not exceed the 15.7° angle of total internal reflection. In addition to the fabrication difficulties of angle polishing the fragile gain medium, the refraction of the emitted beam resulted in relatively steep angles of emission of $\theta_B \approx 43°$. This had an unknown effect on the beam shape, making the external optical configuration challenging. An off-axis parabolic mirror is used to collimate the emitted light, with a grating providing frequency selective feedback for angle tuning. Results from this experiment show multimodal performance (part c) at frequencies corresponding to the free spectral range of the gain medium i.e. $\Delta f = c/n2L$, where c is the speed of light, n and L are the effective index and length of the gain medium respectively. This result indicates residual reflection from the imperfect AR coating. The frequency selective feedback from the grating adds to the residual reflection to emphasize certain Fabry-Pérot modes depending on the grating angle. In this work no estimates for residual reflection of AR coated facet or reflection of the external grating were given.

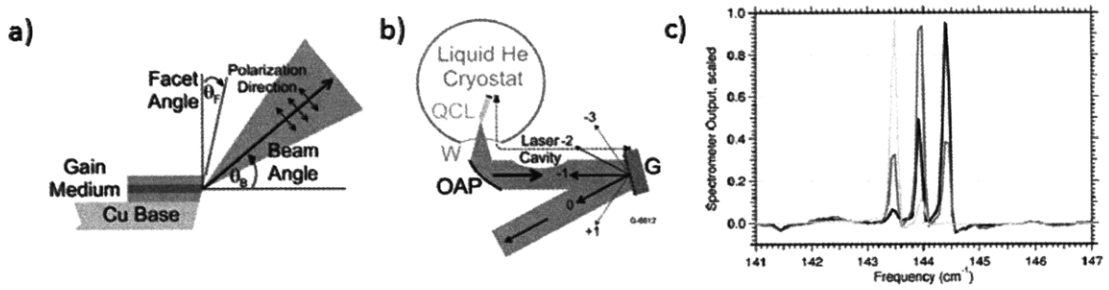

Figure 4-1 (from [89]) Part (a) shows a Brewster angle polished facet acting as an anti-reflection coating in an external cavity configuration (b) using a grating for frequency selective feedback. Optical configuration uses off-axis paraboloid (OAP) to collimate light from the angle polished facet. Residual reflection from polished facet combined with reflection from grating, results in multimodal output (c).

Improved AR coatings were demonstrated in [90-92] using a single layer of SiO_2 with an index of refraction, $n_{SiO_2} \approx 1.8 - 1.9$, which is nearly ideal for a $\lambda/4n$ plane wave impedance matching layer between the GaAs/$Al_{0.15}Ga_{0.85}As$ gain medium and air. The ideal index of a $\lambda/4n$ layer would be $n = \sqrt{n_{GaAs}} \approx 1.89$, similar to 1.98 to 2.1 observed values of SiO_2 [70, 93, 94]. In a controlled study a GaAs wafer was coated with an SiO_2 layer targeting $\lambda \approx 41$ μm. The coated wafer was found to have less than 0.12% reflectivity over a 1-μm bandwidth at a center wavelength of 41.9 μm [90, 91]. This coating was applied to the cleaved facet of the gain medium, and external feedback was provided by a closely spaced external mirror that could be moved over a distance of 160 μm (M in Figure 4-2). The opposed cleaved facet that was not coated acted as the output coupling mirror. Tuning of the metallic mirror inside the liquid helium cryostat allowed continuous frequency tuning by effectively adjusting the cavity length. However the tuning was restricted to within a free spectral range of the cavity (~15 GHz) due to a lack of frequency selective feedback (part b).

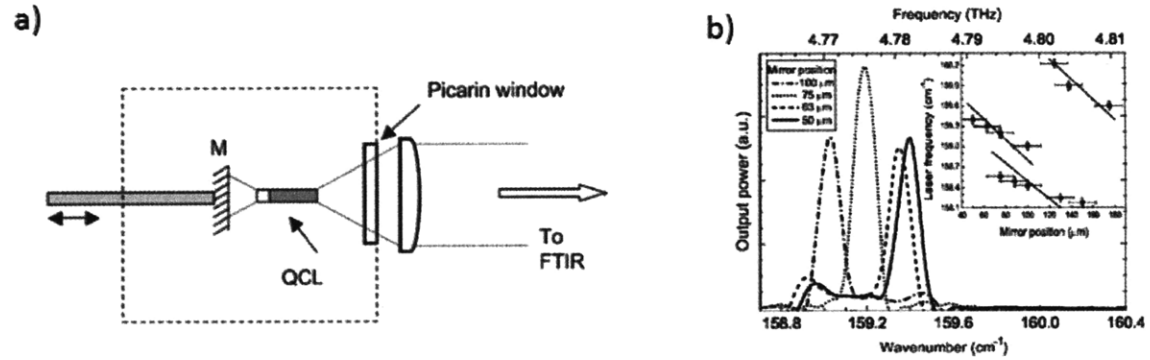

Figure 4-2 (from [91]) Part (a) shows external cavity QCL using a plunger to push an external mirror (M) positioned close the anti-reflection coated facet of the gain medium. The output is taken from the uncoated opposed facet. This design uses an improved λ/4n-thick layer of SiO_2 as an anti-reflection coating. External feedback from the mirror (no frequency selectivity) shows continuous tuning within the free spectral range of the QCL chip.

Estimates of the residual reflectivity of the SiO_2 AR coating were made by observing the lasing threshold current, I_{th}, with and without the presence of the mirror. An expression relating I_{th} with the optical losses due to the presence of the mirror can be derived from the round-trip condition. This is a stationary condition which states that propagating wave must have the same amplitude and phase after a round-trip in order for the laser to oscillate:

$$r_1 r_2 e^{\frac{2jn_{eff}L}{\lambda}} e^{L(\Gamma g_{th} - \alpha_w)} = 1 \qquad \textbf{Eq. 4-1}$$

Here n_{eff} and L are the effective index and length of the gain medium respectively, Γ is the overlap of the optical mode with the gain medium (discussed in section 4.3), $g_{th}$is the material gain necessary to achieve oscillation, α_w is the waveguide loss and r_1 and r_2 are the complex reflection coefficients of the mirrors. The phase condition restricts the lasing wavelengths to values that satisfy:

$$\arg(r_1) + \arg(r_2) + 2 \cdot \frac{n_{eff}L}{\lambda} = M \cdot \pi \qquad \textbf{Eq. 4-2}$$

where M is an integer. When the phase condition is satisfied the gain can be equated to optical losses

losses:

$$\Gamma g_{th} = \alpha_w + \alpha_{m1} + \alpha_{m2} \qquad \textbf{Eq. 4-3}$$

Where $\alpha_{m1,2} = -\frac{1}{2L} \cdot \log\left(|r_{1,2}|^2\right)$. By assuming that Γg_{th} is proportional to I_{th} the effect of changing the mirror reflectivity $R_2=|r_2|^2$ can be used to calculate the residual AR coating reflectivity, $\alpha_{m2}^{no\ mirror}$:

$$\frac{I_{th}^{no\ mirror}}{I_{th}^{mirror}} = \frac{\alpha_w + \alpha_{m1} + \alpha_{m2}^{no\ mirror}}{\alpha_w + \alpha_{m1} + \alpha_{m2}^{mirror}} \qquad \text{Eq. 4-4}$$

Where α_{m2}^{mirror} is assumed to be 0 (i.e. perfect reflection of the closely spaced mirror), the waveguide loss α_w is calculated to be 10.7 cm^{-1}, and the uncoated facet α_{m1} is calculated using the standard literature value of R_1=32% (i.e. reflection of a plane wave at a GaAs/air interface). Using these assumptions an upper bound of $R_2 < 4\%$ is determined for the residual reflectivity of the AR coating.

While this approach demonstrates continuous tuning over a free spectral range (~15 GHz), larger amounts of tuning are not possible without frequency selective feedback. The EC-QCL developed in this work, described in section 4.2, overcomes this limitation by using frequency selective grating feedback. The use of an external grating for feedback instead of a closely spaced mirror results in a large number of additional losses, described in sections 4.4. This approach is made possible largely because of a lens-coupled facet approach similar to that described in chapter 3, along with a semi-insulating surface plasmon waveguide, whose properties are described in section 4.3. This results in good AR coating of the gain medium, as well as some benefits of beam collection. Determination of the performance of the AR coatings is different than the approach used by [91], which relies on the assumption that I_{th} is proportional to g_{th}. This assumption is in general not true, as the gain is a non-linear function of current. An alternate approach is developed in section 4.5 that assumes and quantifies a linear dependence of g_{th} on I_{th} and further does not rely on calculation of the waveguide loss.

4.2 EC-QCL Optical Design

The EC-QCL shown in Figure 4-3 is based on a gain medium (gain chip) with a cleaved front facet which is optically coupled to a silicon hyperhemispherical lens with an external grating for optical feedback (Figure 4-3 part a). The lens is attached using a spacer made of the same high-resisitvity silicon (>10 KOhm-cm, $n_{Si} \approx 3.41$) which is a good index match to the gain medium ($n_{GaAs} \approx 3.6$) resulting in low reflectivity at this

interface. More detailed study of the reflectivity of this interface using finite element simulations is undertaken in section 4.3. Anti reflection coatings using low-density polyethylene are used to reduce reflections at the lens/air interface and are detailed in section 4.5. Two external cavity configurations were considered: a large 10-mm diameter lens for direct collimation of the emitted beam (part b), and a smaller 3-mm diameter lens used in combination with an off-axis parabolic mirror for beam collimation (part c). In both configurations the frequency selective feedback was provided by a grating described in section 4.4.1..

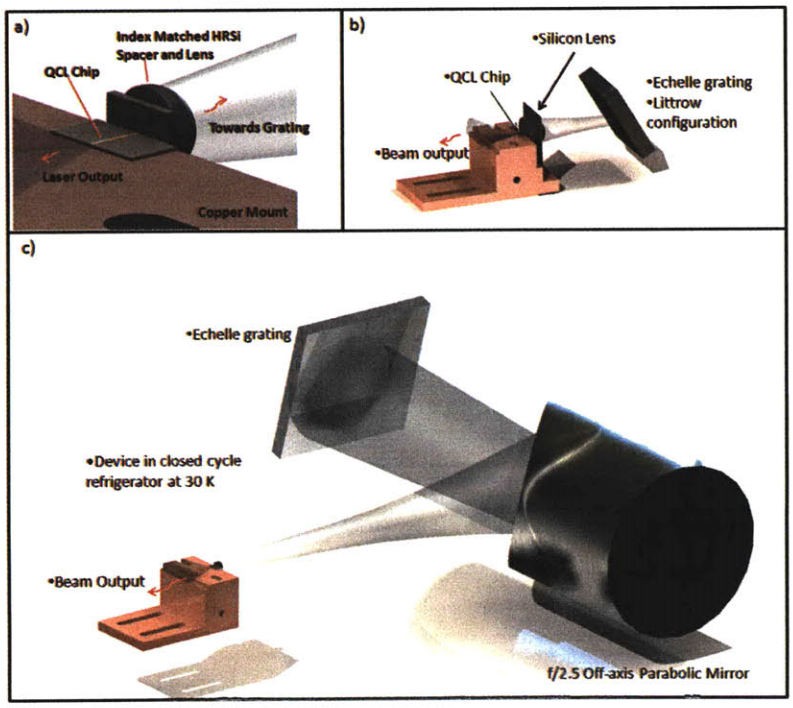

Figure 4-3 External cavity QCL setup. Part (a) shows QCL gain medium (QCL chip) abutted to high-resisitivity silicon (HRSi) spacer and lens, which acts as an anti-reflection coating and a beam forming element. Part (b) shows 10-mm diameter HRSi lens for direct beam collimation, attached using metal retaining clip. Part (c) shows 3-mm diameter HRSi lens attached with optical glue, resulting in a divergent beam which must collimated with an off-axis parabolic mirror. Echelle grating shown in s-polarization (electric field perpendicular to the ruled grooves), though both polarizations were used.

The choice of spacer thickness can be understood from Figure 4-4 which schematically shows the effect on beam divergence. When the spacer thickness is equal to R/n_{Si}, where R is the radius of the lens, the aplanatic condition is met and all rays emerging from point P in Figure 4-4 will refract and diverge as if they originated from point O in the absence

of the lens. This has the effect of both reducing the beam divergence and eliminating spherical and coma aberrations and has been used extensively for millimeter wave applications and as an immersion lens for microscopic objectives [76, 95, 96]. As the spacer thickness is increased, the beam divergence decreases, and the diameter of the beam is best calculated using Gaussian beam theory.

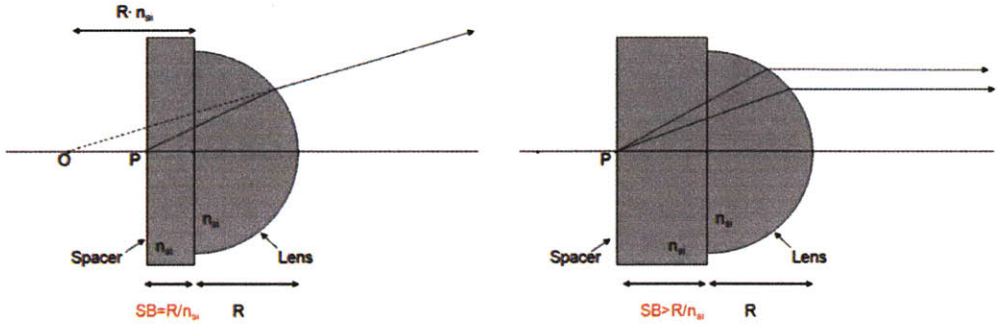

Figure 4-4 Hyperhemispherical lens schematic. Part (a) shows spacer/setback (SB) thickness of R/n. All rays with a focal point of O will have focal point of P after refraction by the lens, resulting in elimination of spherical aberration and coma. Part (b) shows SB>R/n resulting in larger amounts of collimation/focusing at the expense of optical aberration.

Direct collimation of the beam is possible only for larger lens diameters, as the of the beam waist at the lens/air plane, ω_{lens}, which is proportional to the lens size, yields a lower divergence angle, $\theta \approx \lambda/\pi \cdot \omega_{lens}$. Figure 4-5 shows the calculated radius of the $1/e^2$ intensity of a Gaussian beam for both a 10-mm diameter lens system and (part a) and a 3-mm diameter lens system (part b). For the 10-mm lens the spacer thickness was chosen to be approximately 2.2 mm which is 50% greater than the R/n_{Si} distance – resulting in beam collimation over an appreciable distance of ~50 mm. This allows the grating to be placed sufficiently far from the device such that there is no mechanical interference with the vacuum windows of the cryocooler. For the smaller, 3-mm lens configuration, the spacer thickness was chosen to be equal to the $R/n_{Si} \approx 0.46$ mm, resulting in a divergent beam requiring collimation by an off-axis parabolic (OAP) mirror. In Figure 4-5 the OAP is approximated by a thin lens with a focal length of 160 mm. For both Gaussian beam simulations the grating is placed close to a beam waist, which is a symmetry point that allows refocusing of the beam for feedback into the gain chip. A important parameter for this simulation is the initial beam diameter emitted by

the laser, which is calculated to be $\omega_{x,y} \approx 38\ \mu m$, from the calculations of the waveguide parameters 4.4.

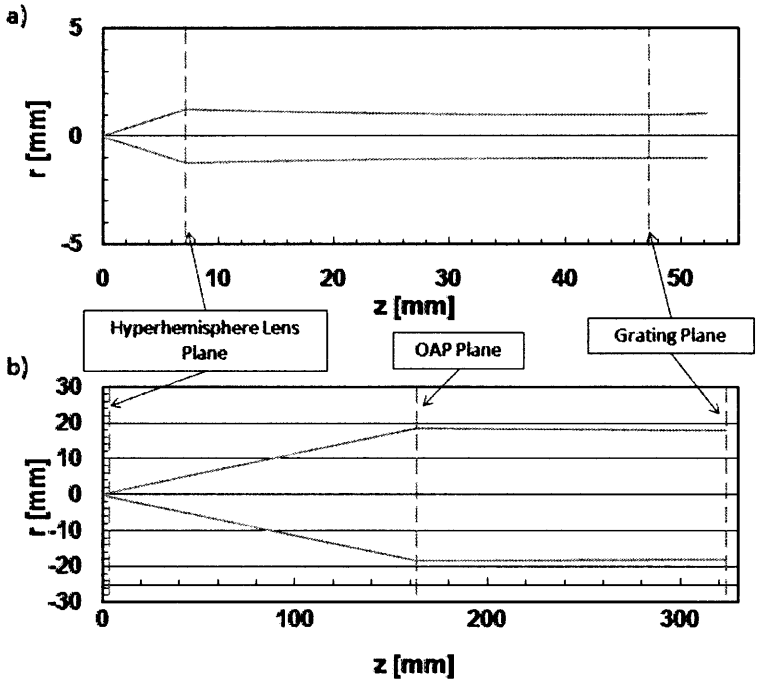

Figure 4-5 Gaussian $1/e^2$ beam radius along the optical axis: part (a), 10-mm diameter lens direct collimation configuration; part (b), 3-mm diameter lens with off-axis paraboloid (OAP) collimation configuration. Calculation assumes λ = 66 μm and an initial $1/e^2$ beam radium of 36 μm, and OAP approximated by thin lens with f=160 mm.

4.3 Semi-Insulating Surface Plasmon Waveguide

The semi-insulating surface plasmon waveguide structure is shown schematically in Figure 4-6 part (a) and consists of the GaAs/AlGaAs active region mesa with a top metal contact above a thin (<1 μm) heavily doped n^+-GaAs contact layer on a semi-insulating GaAs substrate. The doping level of the contact layer used in this work is $n \approx 3\times10^{18}$ cm^{-3} and is sufficient to make the dielectric constant negative at the ~4.4 THz operating frequency of the gain medium. This results in a surface plasmon mode which attaches to the n^+ layer and decays exponentially into the semi-insulating substrate. The result is a low loss waveguide whose intensity mode profile is shown for available widths of 100, 150 and 200 μm, with a substrate thickness of 170 μm and a mesa height of 10 μm. The two dimensional mode simulations were performed using a finite element analysis and are identical to those performed in [97].

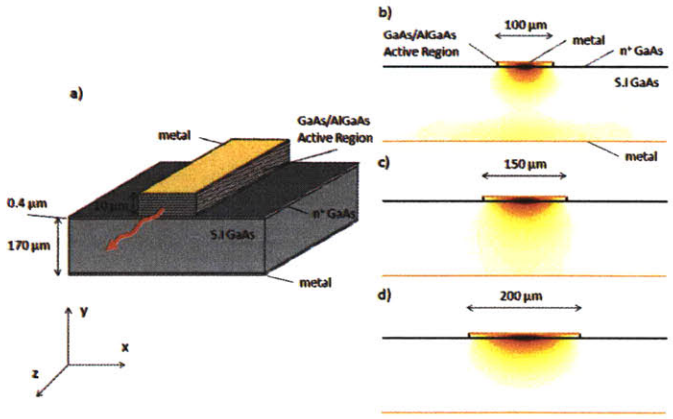

Figure 4-6 Part (a) schematic layout of semi-insulating surface plasmon (SISP) waveguide. Parts b-d show two dimensional finite element mode intensity profile for SISP waveguides with widths of 100 to 200 µm.

An overlap integral between the calculated mode profile and a Gaussian beam can be performed to determined ω_x and ω_y, the Gaussian beams waists in the x and y directions at the facet:

$$\eta = \frac{\int dxdy \cdot E_1(x,y) \cdot E_2^*(x,y-y_o)}{\sqrt{\int dxdy \cdot E_1(x,y) \cdot E_1^*(x,y) \cdot \int dxdy \cdot E_2(x,y) \cdot E_2^*(x,y)}} \qquad \textbf{Eq. 4-5}$$

Where E_1 is the numerically determined y-polarized electric field of the SISP waveguide, the dominant field component, and E_2 is the Gaussian beam electric field at the beam waist (z=0):

$$E_2(x,y) \propto e^{-\frac{x^2}{\omega_x^2}} \cdot e^{-\frac{y^2}{\omega_y^2}} \qquad \textbf{Eq. 4-6}$$

When E_2 is a Gaussian mode the resulting overlap integral, $\eta_{Gaussian}$, is termed "Gaussicity," and is the degree to which the beam is a fundamental Gaussian mode, and is a useful parameter for coupling to other components [98]. Eq. 4-5 is solved numerically to maximize η as a function of ω_x and ω_y and a vertical offset, y_o, resulting in values shown in Table 4.1. For the 100 and 150-µm wide waveguide widths ω_x and

ω_y are nearly identical and therefore have similar collimation lengths and focal points. However the 200-μm wide waveguide is appreciably astigmatic and will therefore be more difficult to feedback into the waveguide using the external cavity.

Table 4-1 SISP Waveguide parameters resulting from finite element simulations at 4.4 THz for the structure shown in Figure 4-6

Width	n_{eff}	α_w (cm^{-1})	Γ	$\eta_{coupling}$ (%)	ω_x (um)	ω_y (um)	$\eta_{gaussian}$ (%)	R_{open} (%)	R_{spacer} (%)
100 μm	3.5964	2.02	.11	35	23.9	19.4	49.8	32.0±0.5	0.1±0.5
150 μm	3.6025	2.51	.16	47	40.0	38.1	71.1	31.4±0.5	0.1±0.5
200 μm	3.6043	2.98	.21	50	42.6	23.5	77.1	31.4±0.5	0.1±0.5

An additional complication of using the asymmetric (in y-axis) SISP waveguide is due to image inversion when the mode passes through the optical system and is fed back into the waveguide, and is shown in Figure 4-7. The external grating/mirror is a symmetry point (part a) which can be unfolded for analysis (part b). Since the beam is collimated by the lens, the unfolded system acts as a two element compound lens, inverting the image of the waveguide mode. In dielectric waveguides this is seldom a problem because the modes are typically symmetric and highly Gaussian. However the SISP waveguide is asymmetric in the y-axis resulting in a reduced optical feedback in an external cavity. Note that in the case where the first lens element focuses the beam on the symmetry point (part c), there is no inversion. This configuration would result in a small area of the grating being illuminated and poor grating efficiency.

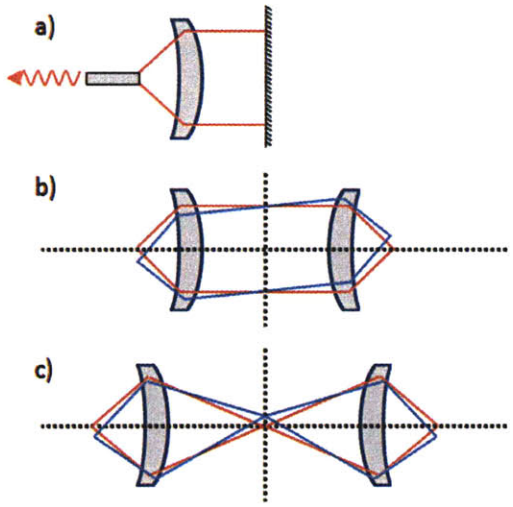

Figure 4-7 Schematic optical ray trace of EC-QCL illustrating the inversion problem: part (a) shows emitted beam collimated with a lens and reflected by mirror; part (b) shows unfolded mirror, and inverted image; part (c) shows hypothetical case for focusing lens, which would not invert the image. Focusing lens is not possible because the small illuminated area in the mirror plane would lead to low grating efficiency.

The maximum coupling efficiency under inversion, $\eta_{coupling}$, is calculated using Eq. 4-5 with the displacement in the y-axis as a fitting parameter. Here E_1 is again the numerically calculated vertically polarized electric field and E_2 is an inverted image of E_1. For the narrower, 100-μm wide waveguide, the maximum coupling is only 35%. This is because the narrower width forces the mode into the dielectric making it more asymmetric, which can also be inferred from the low value of $\eta_{Gaussian}$. The 150-μm waveguide is therefore preferred because of the high value $\eta_{Coupling}$, and the symmetry of the beam in the x and y axes.

Additional three-dimensional simulations were performed on the SISP waveguide to determine the facet reflectivity under open conditions and when covered by a silicon spacer for AR coating. The simulation technique is similar to the approach taken for metal-metal waveguide facet simulation by *Kohen* [97]. The simulation uses the two dimensional mode as an excitation for three dimensional structure, with a "cleaved," open facet. The result is a standing wave caused by the interference of the excitation and the reflection from the open facet. The standing wave ratio is used to determine the facet reflectivity:

$$SWR = \frac{\langle E_1(x,y)|E(x,y)\rangle|_{max}}{\langle E_1(x,y)|E(x,y)\rangle|_{min}} = \frac{1+|r|}{1-|r|} \qquad \text{Eq. 4-7}$$

Here E_1 is the y polarized electric field from the two dimensional simulation, and E is a cross-section from the three dimensional simulation. The inner product in Eq. 4-7 is taken over the xy-plane at various points along the z-axis propagation direction where the maximum and minimum values are observed. For the open facet condition the calculated reflectivity is 32% and identical to what would be expected from Fresnel reflection, i.e. a plane wave at normal incidence on a GaAs/air interface. It is not surprising that when the facet is covered by a silicon spacer, the reflectivity effectively vanishes below the numerical error of the simulation <0.5%. Note that this assumes that there are no gaps between the silicon spacer and the waveguide facet – a condition that is sometimes difficult to achieve in practice.

4.4 External Cavity Laser Model

The lasing threshold gain of a simple Fabry-Pérot cavity device can be calculated by determining the net gain, $\Gamma g_{th} - \alpha_w = \alpha_{m1} + \alpha_{m2}$ from Eq. 4-3, which is required to overcome the optical losses of the cavity mirrors, r_1 and r_2. For more complicated three mirror systems such as an EC-QCL with a weakly reflecting anti-reflection coating as depicted in Figure 4-8, three reflection coefficients exist: r_1 and r_2, the electric field reflection coefficients of the front and back facet of the QCL chip; and $r_{ext}(\lambda,\theta_G)$, the reflection coefficient from the external grating which is a function of wavelength and grating angle θ_G. The combination of r_2 and r_{ext} can be considered a compound external mirror that can be equated to a single reflection coefficient, r_{eff} allowing compatibility with Eq. 4-2 and Eq. 4-3. Here, the interference between the reflections from r_2 and r_{ext} have been incorporated in the second term of equation Eq. 4-8, simplifying the resonator as shown in part c.

$$r_{eff}(\lambda,\theta_G) = r_2 + \frac{t_2^2 \cdot r_{ext}(\lambda,\theta_G) \cdot e^{-2\cdot j\cdot \beta_{ext}\cdot L_{ext}}}{1 + r_2 \cdot r_{ext}(\lambda,\theta_G) \cdot e^{-2\cdot j\cdot \beta_{ext}\cdot L_{ext}}} \qquad \text{Eq. 4-8}$$

Using r_{eff}, the phase condition of Eq. 4-2 can be used to solve for the lasing wavelengths, allowing Eq. 4-3 to be solved in turn. However a more general approach using transmission matrices described in [99] and implemented in section 0 allows the net gain/mirror losses to be determined at all wavelength, and not just the lasing wavelengths. In either case the r_{eff} must be determined along with its dependence on λ and θ_G.

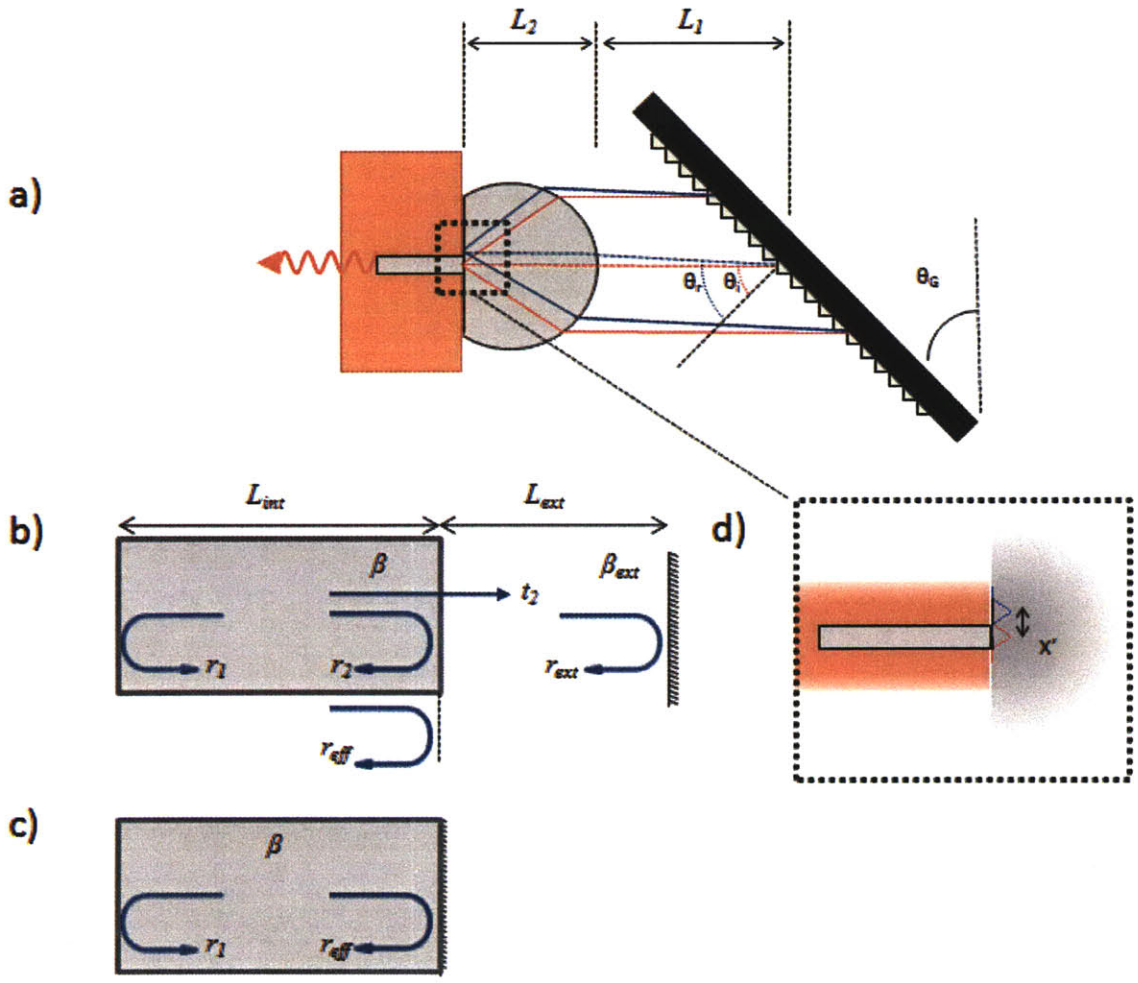

Figure 4-8 Schematic drawing of External Cavity QCL in Littrow configuration

The external reflectivity, $|r_{ext}|^2$, is the fraction of the emitted power that is coupled back into the optical mode of the SISP waveguide by the external grating:

$$|r_{ext}|^2 = T^2 \cdot \eta_{coupling} \cdot \eta_{grat}, \qquad \textbf{Eq. 4-9}$$

where T is the power transmitted and accounts for the optical losses of the system, η_{grat} is the grating reflectivity described below, and $\eta_{coupling}$ is the maximum overlap of the SISP optical mode with the reflected image from the grating calculated in section 4.3. The use of the grating makes r_{ext} a function of the grating angle, θ_G, and wavelength, λ. This is depicted schematically in the ray trace of part (a): after the emitted beam (red) has propagated through the lens, it is diffracted from the grating and coupled back into the waveguide (blue). Dispersion from the grating causes a small displacement of the diffracted beam, seen as a displacement of the ray trace in part a. The displacement, x', is shown schematically in part (d) for a Gaussian mode profile, illustrating the reduction of overlap of the reflected mode with the waveguide mode. To calculate the lateral displacement, x' an optical ray transfer matrix (ABCD) is used to model the effect of each optical component on a ray passing from the center of the grating to the focal plane of the lens on the facet of the device (dashed blue line):

$$\begin{bmatrix} x' \\ \theta' \end{bmatrix} = \underbrace{\begin{bmatrix} 1 & L_1 \\ 0 & 1 \end{bmatrix}}_{Freespace} \cdot \underbrace{\begin{bmatrix} 1 & 0 \\ \frac{(n_1 - n_2)}{R \cdot n_2} & \frac{n_1}{n_2} \end{bmatrix}}_{Curved\ Si\ Lens} \cdot \underbrace{\begin{bmatrix} 1 & L_2 \\ 0 & 1 \end{bmatrix}}_{Freespace} \cdot \begin{bmatrix} x \\ \theta \end{bmatrix} \qquad \textbf{Eq. 4-10}$$

Where x=0 is the initial displacement of the ray from the optical axis, $\theta=\theta_r-\theta_i$ is the initial angle of the ray, and x' and θ' are the final displacement and angle respectively.
Using the optical elements depicted in Figure 4-8, the displacement is:

$$x' = (\theta_r - \theta_i) \cdot \left[L_1 \cdot \left(\frac{L_2 \cdot (n_1 - n_2)}{R \cdot n_2} + 1 \right) + \frac{L_2 \cdot n_1}{n_2} \right]_{x=0} \qquad \textbf{Eq. 4-11}$$

Wavelength dependence of x', is determined by the grating equation, which determines the diffraction angle, θ_r.

$$d \cdot (\sin\theta_i + \sin\theta_r) = m \cdot \lambda \qquad \textbf{Eq. 4-12}$$

Where m is the grating order and d is the separation between the grooves of the grating. For a given grating angle, there exists a wavelength such that the diffraction angle is equal to the incidence angle, $\theta_G \equiv \theta_i = \theta_r$. This is the Littrow condition, which maximizes the feedback of the external grating:

$$2 \cdot d \cdot sin\theta_G = \lambda_L \qquad \textbf{Eq. 4-13}$$

Combining the grating equation, Eq. 4-12 and the Littrow condition, Eq. 4-13, results in the expression $\theta_r - \theta_i = \frac{m\cdot(\lambda-\lambda_L)}{d\cdot\cos\ \theta G}$. In combination with Eq. 4-11, this allows determination of x' and therefore $\eta_{coupling}(\lambda)$ as a function of wavelength. Figure 4-9 shows $\eta_{coupling}(\lambda)$ for a 150-μm wide waveguide in both the -1st and -2nd grating diffraction orders. The peak value of $\eta_{coupling}(\lambda)$ corresponds to the maximum value in table Table 4-1 when $x'= 0$.

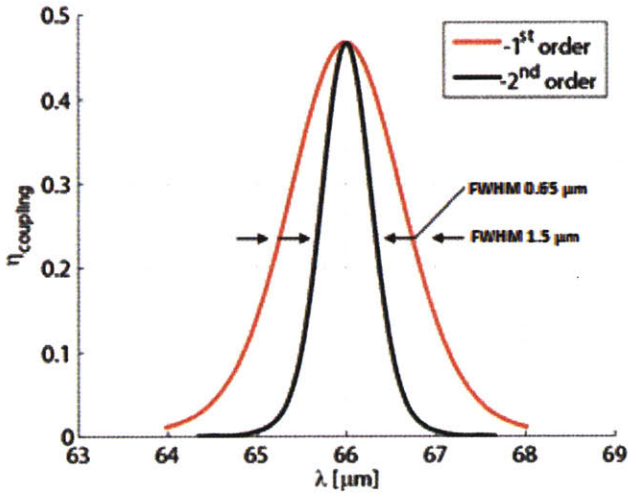

Figure 4-9 Coupling efficiency ($\eta_{coupling}$) plotted against wavelength for the EC-QCL system depicted in Figure 4-8 for 150-μm wide waveguide . Center wavelength can be adjusted by changing the grating angle.

4.4.1 Grating Efficiency

The Littrow grating efficiency, $\eta_{grat}(\lambda,m)$, is the reflectivity of the grating for angles $\theta_i = \theta_r$ and is calculated in Figure 4-10, and parameterized as a function of grating order, m. The calculation was performed using a commercial code (PC-Grate, IIG) to solve for the

reflectivity of a sawtooth shaped grating with a blaze angle of 27.4^0 with a frequency of 7.8 grating periods/mm. At this frequency and blaze angle, the optimum wavelength for the 1st diffraction order is 118 μm, and 59 μm for the 2nd order according to equation Eq. 4-13. The simulation differs somewhat due to polarization effects of the p-polarized (TE or electric field parallel to grooves) light. This simulation gives only a rough estimate of grating reflectivity as no specifications were provided by the manufacturer.

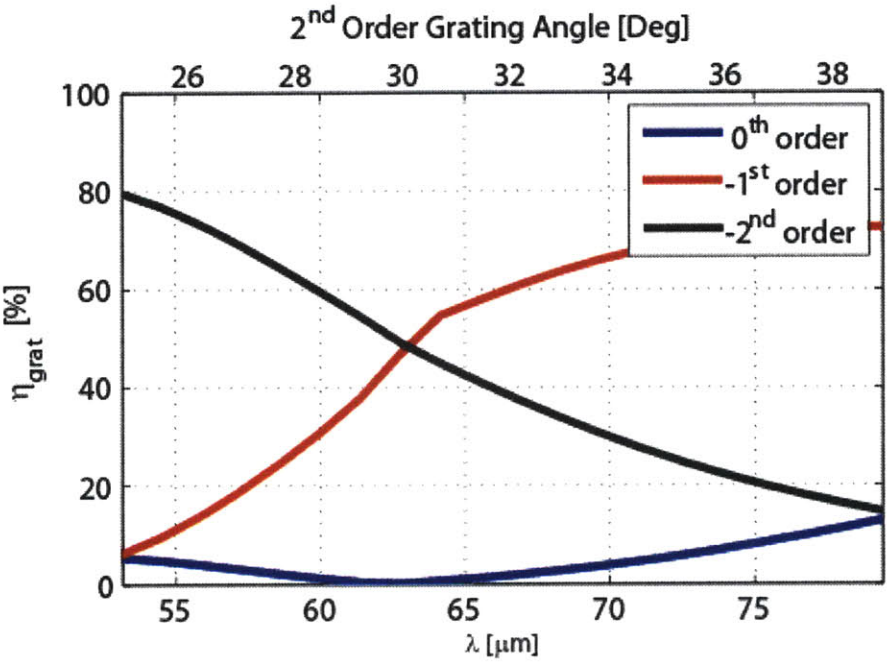

Figure 4-10 Grating efficiency (η_{grat}) in Littrow configuration ($\theta_i = \theta_r$) as a function of wavelength, parameterized by grating order.

4.4.2 Optical Losses

Optical losses/reflections can reduce the transmission, *T*, through the external cavity. This can result from absorption by the silicon lens, partial transmission at lens/air interface, partial transmission through the polypropylene vacuum window, and atmospheric absorption in the external cavity. To quantify some of these losses Fourier transform infrared (FTIR) transmission measurements were made on samples shown in Figure 4-11. A 1.5-mm thick high-resisitivity silicon was used as the substrate and has transmission between 45 and 50% throughout the frequency range of interest 2-5 THz (60 to 150 μm). This is consistent with Fresnel reflection losses at two air/silicon interfaces

and suggests that the losses are < 1 cm^{-1}. Three thin film coatings were tested as candidate anti-reflection coatings for the lens/air interface: parylene-N, SiO_2, low density polyethylene (LDPE), and SiO_2. Parylene-N was vacuum deposited on both sides of the sample and was measured to be 10.5-μm thick. The peak transmission is at 5.2 THz ($n_{Parylene} \approx 1.48$) at 88% which corresponds to a single sided (vacuum/parylene/silicon) transmission of 94% (assuming no optical losses), which is consistent with literature values [100, 101]. Similar results were obtained for 13-μm thick LDPE coatings which had 84% transmission (92% single sided) at a frequency of 3.9 THz ($n_{LDPE} \approx 1.46$). Good performance of SiO_2 coatings have been reported [90, 94], however poor results were obtained for coatings attempted here. The coatings were deposited by PECVD using a substrate temperature of 150°C, limited by the machinery. It is possible that higher temperature result in an annealing effect, improving the quality of the materials. As high quality polymer coatings were already available, no further study of SiO_2 coatings were done.

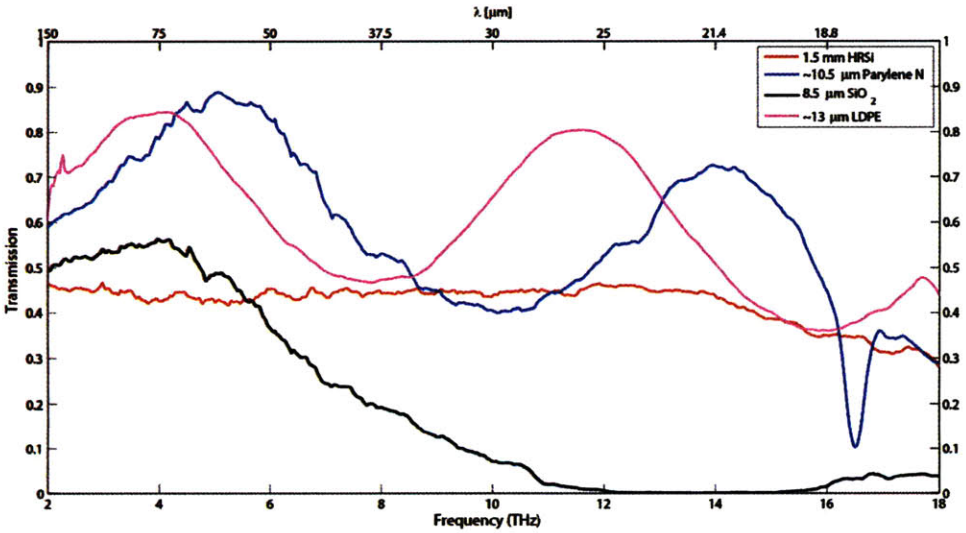

Figure 4-11 Transmission through silicon wafer with various sample anti-reflection coatings applied.

Additional losses from the vacuum windows were previously measured and reported in [102]. The thin, 0.25-mm thick polypropylene vacuum sheets have values of 80-90% from 2 to 5 THz. Losses due to atmospheric water vapor are modeled using HITRAN, and are highly frequency depended. For modeling purposes low losses of 90% are

consistent with short path lengths (~10 cm) in transmission windows such as that shown in Figure 4-16.

4.4.3 Numerical Analysis of EC-QCL Modes

The EC-QCL shown in Figure 4-8 has an equivalent transmission matrix (T-matrix) representation as shown below, and can be used for analysis of power flow into and out of the system providing a model for the determination of the optical losses/threshold gain condition and the lasing frequencies. This analysis uses the notation from *Coldren* [99] and assumes a single mode (transmission line) description of the field in the waveguide, $\mathbf{E}(x,y,z,t) = \hat{\boldsymbol{e}} \cdot E_o U(x,y) e^{j(\omega t - j\beta z)}$, where E_o is the wave amplitude and the x and y spatial dependence can be separated, leaving only the $e^{j\beta z}$ spatial depenced. The resulting input and output to the system is the amplitude of the waveguide mode $A_j = \frac{E_0}{\sqrt{2\eta_j}} \cdot e^{-j\cdot\beta\cdot z}$. Here the power flowing in in the positive $\hat{z}$ direction is calculated $P_j^+ = A_j \cdot A_j^* = \frac{|E_o|^2}{2\cdot\eta_j}$ where η_j is the impedance of the guided wave and the power flowing into any node is calculated $P_j = A_j \cdot A_j^* - B_j \cdot B_j^*$.

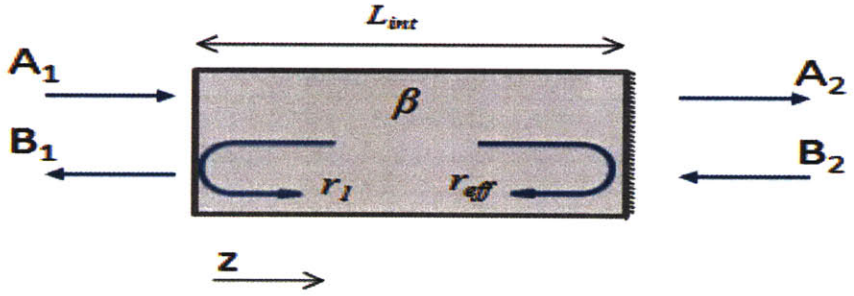

Figure 4-12 Transmission matrix parameter definitions

$$\begin{bmatrix} A_1 \\ B_1 \end{bmatrix} = \begin{bmatrix} T_{11} & T_{12} \\ T_{21} & T_{22} \end{bmatrix} \cdot \begin{bmatrix} A_2 \\ B_2 \end{bmatrix}$$

$$= \underbrace{\begin{bmatrix} T'_{11} & T'_{12} \\ T'_{21} & T'_{22} \end{bmatrix}}_{r_1} \cdot \underbrace{\begin{bmatrix} T''_{11} & T''_{12} \\ T''_{21} & T''_{22} \end{bmatrix}}_{Active\ Region} \cdot \underbrace{\begin{bmatrix} T'''_{11} & T'''_{12} \\ T'''_{21} & T'''_{22} \end{bmatrix}}_{r_{eff}} \cdot \begin{bmatrix} A_2 \\ B_2 \end{bmatrix} \qquad \textbf{Eq. 4-14}$$

$$= \underbrace{\begin{bmatrix} \frac{1}{t_1} & \frac{r_1}{t_1} \\ \frac{r_1}{t_1} & \frac{1}{t_1} \end{bmatrix}}_{r_1} \cdot \underbrace{\begin{bmatrix} e^{j\beta L_{int}} & 0 \\ 0 & e^{-j\beta L_{int}} \end{bmatrix}}_{Active\ Region} \cdot \underbrace{\begin{bmatrix} \frac{1}{t_{eff}} & \frac{r_{eff}}{t_{eff}} \\ \frac{r_{eff}}{t_{eff}} & \frac{1}{t_{eff}} \end{bmatrix}}_{r_{eff}} \cdot \begin{bmatrix} A_2 \\ B_2 \end{bmatrix}$$

The reflection coefficient r_1 is determined from the waveguide simulations of 4.3, and is close to the value expected for a plane wave at normal incident to a GaAs/Air ($n_{GaAs} \approx 3.61$) dielectric interface $|r_1|^2=32\%$. The external effective reflection coefficient r_{ext} is evaluated using the preceding analysis. Calculation of the transmission coefficient includes all power not reflected into the waveguide mode, and includes light that is radiated, absorbed, scattered or reflected into evanescent/higher order modes, i.e. $t_j = \sqrt{1 - |r_j|^2}$. The real part of the complex propagation coefficient $\beta=\beta'+j\beta''$, is the propagation constant of the waveguide, β' , and the imaginary part is the net gain or loss of the material, $\beta''= (\Gamma g - \alpha_w)/2$. Numerical determination of the cavity losses at a particular frequency (propagation constant) is possible by calculating the ratio of output power to input power, as a function of the gain parameter β'':

$$\frac{P_{out}}{P_{in}} = \frac{|A_2|^2 + |B_1|^2}{|A_1|^2} = \frac{|T_{21}|^2 + 1}{|T_{11}|^2} \qquad \textbf{Eq. 4-15}$$

In the simplifying case of a Fabry-Pérot resonator with identical front and back mirrors ($r_1=-r_2$), Eq. 4-15 reduces to:

$$\frac{P_{out}}{P_{in}} = \frac{\left|1 - e^{-2\cdot j\cdot \beta'\cdot L} \cdot e^{2\cdot \beta''\cdot L}\right|^2 \cdot |r_1|^2 + e^{-2\cdot \beta''\cdot L} \cdot |t_1|^4}{\left|1 - |r_1|^2 e^{-2\cdot j\cdot \beta'\cdot L} \cdot e^{2\cdot \beta''\cdot L}\right|^2} \qquad \textbf{Eq. 4-16}$$

This expression becomes singular at the resonant frequencies of the cavity, $\beta' \cdot L = m \cdot \pi$ where m is an integer, and when the gain parameter equals the cavity loss due to the mirrors, $\beta'' = -j \cdot \frac{\ln|r_1|}{L}$. This condition corresponds to the threshold for lasing where the P_{out} is infinite for a finite P_{in}. At non-resonant frequencies, the gain parameter which maximizes Eq. 4-16 can be determined numerically, resulting in a finite value of P_{out}/P_{in} i.e. amplification instead of oscillation. A plot of the numerically determined gain parameters, converted to net gain by multiplication by a factor of 2, are shown in Figure 4-13. This gain parameter is equivalent to the mirror losses, $\alpha_{m1} + \alpha_{meff}$, where r_2 has been replaced by the r_{eff} of Eq. 4-8.

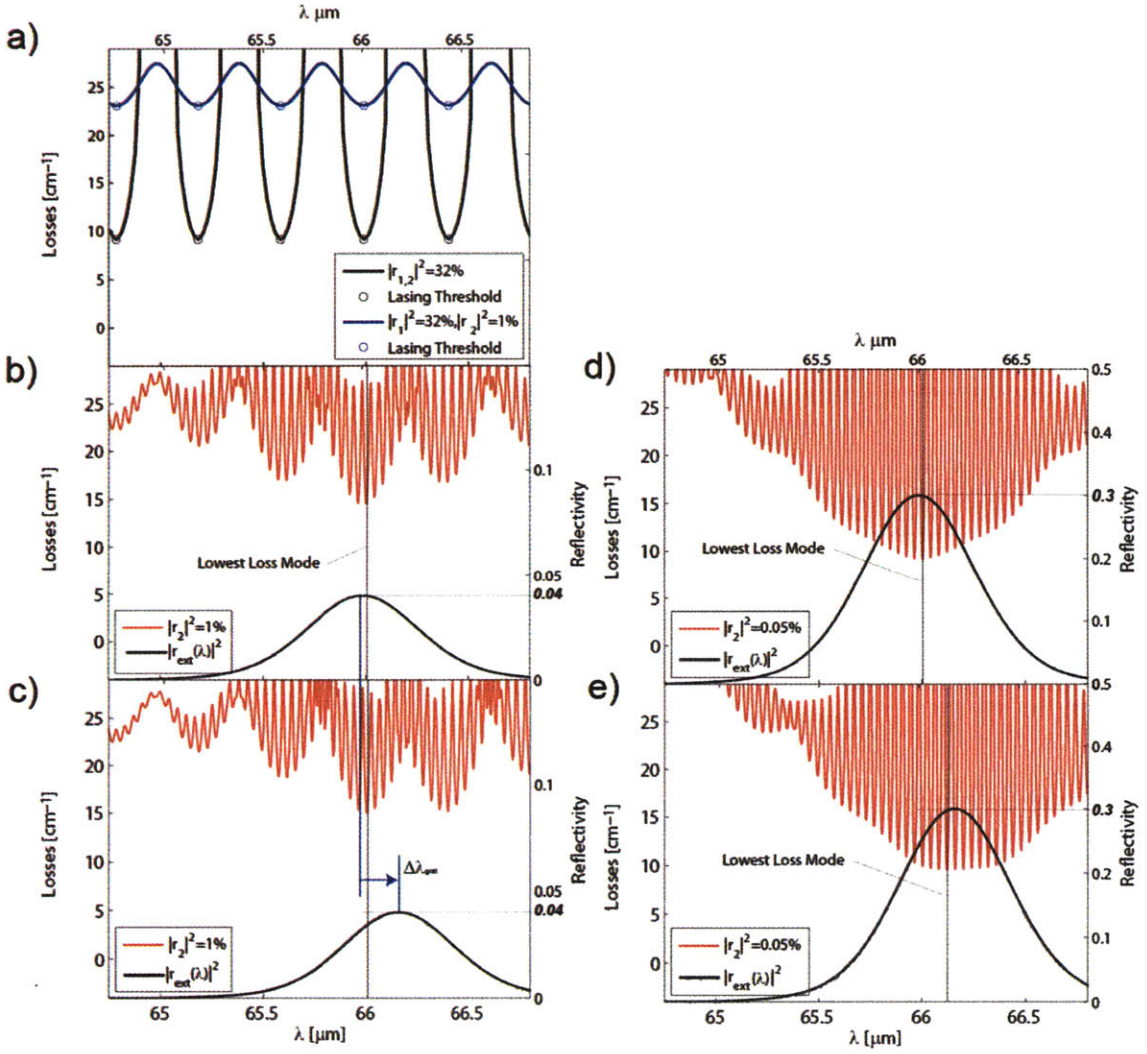

Figure 4-13 Mirror losses (net gain) analysis: part (a) shows Fabry-Pérot laser cavity with equal mirror reflectivity of 32% (black) and with one mirror anti-reflection coated at $|r_2|^2$=1% (blue); part (b) shows the same anti-reflection coated Fabry-Pérot with an additional external mirror, with wavelength dependent reflectivity, $|r_{ext}(\lambda)|^2$ (black). With imperfect AR coatings angle tuning of the grating resulting in wavelength shift ($\Delta\lambda_{grat}$) of $|r_{ext}(\lambda)|^2$ does not guarantee that the lasing wavelength will change as seen in (b) and (c). In (c) the peak reflectivity is chosen to be midway between Fabry-Pérot modes, where tuning is most difficult. Good AR coatings and strong external reflectivity allow tuning between Fabry-Pérot modes as shown in part (d) (note the peak $|r_{ext}(\lambda)|^2$ is 20%). Device length used in simulation is 1.247 mm with an effective index n_{eff}=4.26 with an external cavity length of 50 mm.

This analysis is useful for observing the net gain at non-resonant frequencies for devices with anti-reflection coatings, and predicting the tuning performance of an external cavity device. Figure 4-13 part (a) shows the net gain for a device with two cleaved facets (black trace). Lasing can occur on any of the Fabry-Pérot modes as they have equal amounts of loss. With the application of an imperfect AR coating with a reflectivity of 1% the threshold of the Fabry-Pérot modes increases but the net gain between the modes decreases. With the addition of an external grating (part b) the closely spaced external longitudinal modes of the external cavity become apparent and lowest loss modes occurs near the Fabry-Pérot chip modes due to external reflectivity reinforcing the reflection of the imperfect AR coatings. Here the maximum of $|r_{ext}(\lambda)|^2$ is taken to be 4%, which is consistent with measurements taken below. As the grating tunes to a frequency between the Fabry-Pérot modes, the lowest loss mode does not change. In contrast, using the highest theoretical $|r_{ext}(\lambda)|^2 \approx 30\%$ along with improved AR coatings with a reflectivity of 0.05%, tuning between the closely spaced external cavity modes is possible (parts d and e). This is because the interaction of the Fabry-Pérot chip modes is far reduced. In these simulations only angle tuning is performed, in practice the length of the external cavity, L_{ext}, is also tuned simultaneously so that continuous tuning can be obtained, i.e. changing L_{ext} allows tuning between the external cavity modes.

4.5 Results

The gain medium of the QCLs is based on the resonant-phonon depopulation design and are the same as those in [54], which showed power levels of ~250 mW at 10 K in pulsed operation, lasing at ~4.3 THz. Two devices were used in configuration (a) of Figure 4-14 with dimensions of 100-μm wide by 1.34- and 1.5-mm long, and a device measuring 150-

μm wide by 1.25-mm long was used in configuration (b). Using the lens alignment technique from section 3.4 [58], high resistivity silicon (HRSi, >10 kOhm-cm) lenses and thin HRSi spacers were abutted to the cleaved laser facets. The HRSi spacer protects the facet during lens alignment and allows accurate control of the total lens thickness which affects beam divergence and optical aberrations. For the larger 10-mm lens a spring retaining clip was used to maintain contact with the spacer/facet. For the smaller 3-mm lens, the holding force of UV-curing glue (Norland #81) was sufficient to secure the lens and spacer. The 10-mm diameter HRSi lens configuration was used with two slightly different spacer thicknesses of 2.21 mm and 1.97 mm for the 1.34 and 1.5 mm long devices respectively, which showed negligible performance differences. All lenses were coated with a 13-μm thick layer of LDPE as an AR coating. LDPE was chosen for its simplified application by temperature controlled hot air gun and comparable performance to parylene-N at the lasing frequencies.

The reduced divergence of the 10-mm diameter lens setup is verified experimentally from the microbolometer images of the beam from the 1.34-mm long device at distances of 52 mm and 60 mm from the lens tip, shown in Figure 4-14 (c) and (d) respectively [41]. By comparison, the much smaller 3-mm lens configuration, which has a total length of 1.96 mm, resulted in a smaller beam waist, and a much more divergent beam as seen by the larger beam pattern at a closer position of ~22 mm from the lens tip (Figure 4-14 (e)). This increased divergence required an external f/2.5 off-axis paraboloid mirror to collimate the beam. The echelle grating used in all configurations is blazed for a wavelength of 118 μm and is operated in either the -1^{st} or -2^{nd} order in Littrow configuration.

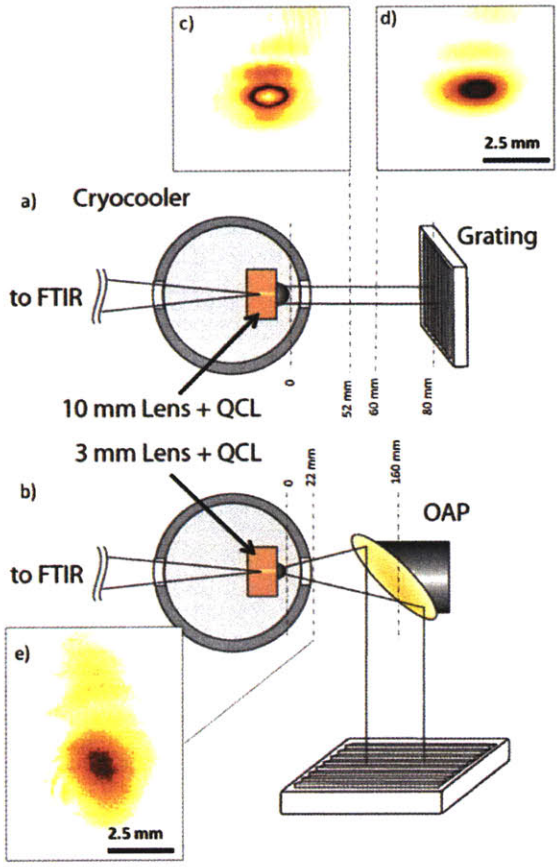

Figure 4-14 Parts (a) and (b): EC-QCL configurations with and without off-axis paraboloid mirror (OAP). Parts (c),(d) and (e): measured beam patterns from lens coupled QCLs.

The devices were mounted in a closed-cycle, pulse-tube cryorefrigerator (PT60, Cryomech), and cooled to ~30 K. A pulsed electrical bias of 13.5 ms repeated at 20 Hz was used for the collected light versus current (*L-I*) characteristics in Figure 4-15. Here three different conditions are shown: without a lens, using a lens with maximum external feedback from a gold mirror, and using a lens with no external feedback. The 1.34-mm long device shows an increase in threshold current (current density, J_{th}) from 0.81 A (600 A/cm^2) before mounting a lens, to 0.88 A (650 A/cm^2) with a lens and an external mirror for feedback, up to 0.95 (710 A/cm^2) when using a lens without any external feedback.

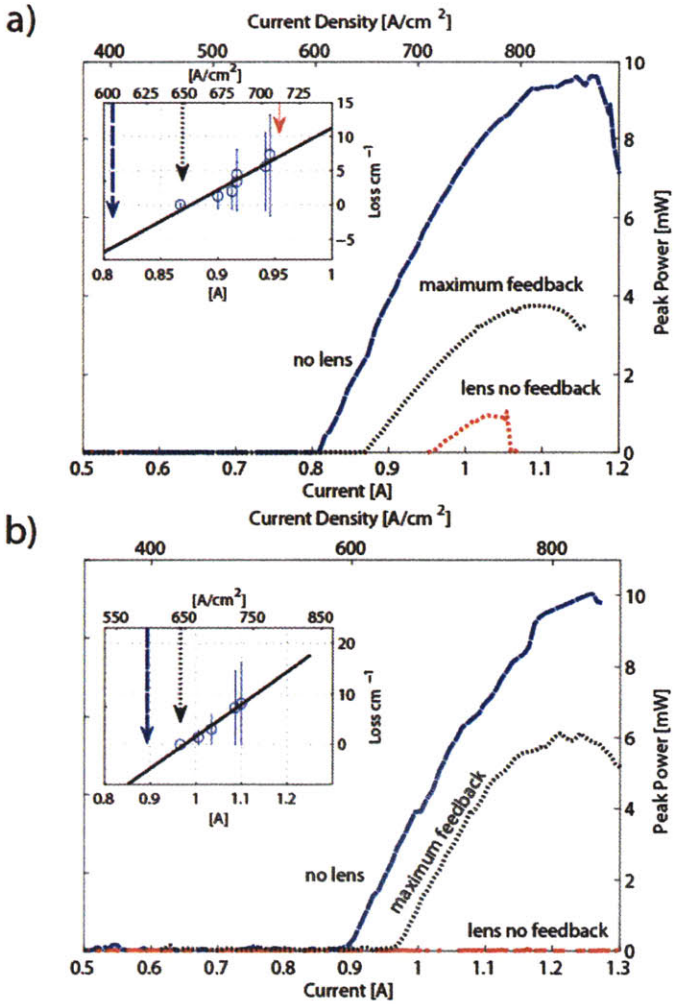

Figure 4-15 Collected light versus current characteristics for devices measuring: 100-μm wide by 1.34-mm long (a), and 1.5-mm long (b), using 10-mm diameter lens setup of Figure 4-14 part (a). Insets shows variation of threshold current versus additional loss added to the path of the external cavity. Vertical arrows indicate lasing threshold.

The maximum and minimum reflectivities of the external optical system can be determined by studying the effect of the cavity losses on J_{th}. For resonant-phonon designs J_{th} is limited by a parasitic current channel ($J_{th} > J_{Parasitic}$). This necessitates an incremental comparison of J_{th} with loss:

$$\Delta J_{th} \propto \Delta\alpha \qquad \textbf{Eq. 4-17}$$

Note that this analysis differs for that presented in section 4.1 by *Xu et. al.*, where I_{th}, equivalent in the comparison to J_{th}, was directly compared with losses due to the use of a bound-to-continuum design. In Eq. 4-17, α is the sum of the optical loss terms: the waveguide loss, α_ω; the mirror loss from the output facet, α_{m1}; the mirror loss from the lens-coupled facet, α_{m2}; and an additional loss, α_{add}, which can be added to the path of the external cavity to study J_{th}. Additional loss is added by inserting a number of polyester/polyethylene sheets in the external cavity. The sheets were positioned at an angle with respect to the beam in order to eliminate Fabry-Pérot effects. Transmission values of the polyester/polyethylene sheets were determined by biasing the laser above the lasing threshold and measuring the transmitted power using a pyroelectric detector. Loss values were calculated using the formula $\alpha_{add}=-\log(T)/L$, where T is the transmission through the lossy sheets, and L is the device length. The inset of Figure 4-15 (a) shows the resulting linear relationship of J_{th} versus α_{add} with a slope of $d\alpha/dJ=12\cdot10^{-2}$ [$cm^{-1}/(A/cm^2)$]. The slope allows the calculation of α_{m2}:

$$\alpha_{m2} = -\frac{\log(0.32)}{2 \cdot L_{int}} + (J'_{th} - J_{th}) \cdot \frac{\partial \alpha}{\partial J} \qquad \textbf{Eq. 4-18}$$

Where the first term is the assumed mirror loss from a bare facet with a reflectivity of 32%, and the second term is the additional loss inferred by the increase in threshold current density, where J_{th} is measured without a lens or spacer and J_{th}' is measured with a lens and various amounts of feedback. For the case of maximum external feedback (i.e. a mirror), α_{m2} is 9.8 cm^{-1} which corresponds to a reflectivity of 7%. For the case of minimum external feedback (i.e. no external mirror), α_{m2} is 18 cm^{-1} which corresponds to a minimum (residual) reflectivity of 1%. Similar measurements were performed on the 1.5-mm long device, which showed somewhat better AR characteristics through the suppression of lasing in the absence of external feedback. The resulting slope is $d\alpha/dJ=9.6\cdot10^{-2}$ corresponding to an α_{m2} of 8.5 cm^{-1} (8% maximum reflectivity) based on threshold current (current density) values of 0.89 A (595 A/cm^2) and 0.97 A (640 A/cm^2). A minimum reflectivity cannot be determined in this case because there is no observable threshold in the absence of external feedback. However, bounds for the minimum

reflectivity can be determined using the peak current density of 1.21 A (800 A/cm^2) and the highest observed threshold of 1.1 A (730 A/cm^2) resulting in residual reflectivity values between 0.05% and 0.6%, which are sufficient to quench lasing.

The measured maximum reflectivity of 7-8% using the gold external mirror is slightly lower than the calculated values of $|r_{ext}|^2$ = 20-27% resulting from Eq. 4-9 (where $\eta_{grating}$ = 1 for external mirror). The maximum optical losses result from the polypropylene vacuum window which has ~80% transmission, an atmospheric transmission of ~90%, calculated for the 17-cm external path length at 296 K and 40% relative humidity (Figure 4-16, HITRAN 2008), the LDPE AR layer on the lens with a transmission of ~92% at 4.4 THz (Figure 4-16), and $\eta_{coupling}$ of 35% and 47% for 100 and 150 μm wide waveguide respectively. The 20-27% maximum reflectivity is likely further reduced by optical aberrations and misalignment of the external optics, which are not calculated here.

The external optical system, in combination with the lower reflectivity of the grating, is sufficient to allow frequency selective feedback by angle tuning, resulting in the spectra shown Figure 4-16 part (b) for the 1.5 and 1.25-mm long devices. Here spectra taken at various grating angles are superposed. The devices were operated with short pulses of 200 to 800 ns repeated at 100 KHz. For the 1.5-mm long device (configuration a) the total tuning range is 165 GHz with a center frequency of 4.4 THz, equivalent to 3.8% tunability of the central frequency. However, frequency hopping is observed between the longitudinal modes of the ridge device spaced at 24 GHz, which corresponds to an effective index n_{eff}=4.24. Even though lasing is suppressed in the absence of feedback, the lens does not provide a perfect AR coating, and lasing occurs preferentially on the longitudinal modes where there is some small residual feedback in addition to the external feedback. This is consistent with the EC-QCL model simulations for similar reflectivities and feedback in Figure 4-13. A similar result was obtained for the 1.25-mm long device (configuration b) which showed 145 GHz of discontinuous tuning between modes spaced at 29 GHz, corresponding to n_{eff}=4.14. However in this case 9 GHz of continuous tuning near the longitudinal modes was measured, suggesting either slightly stronger feedback or better AR effect of the lens.

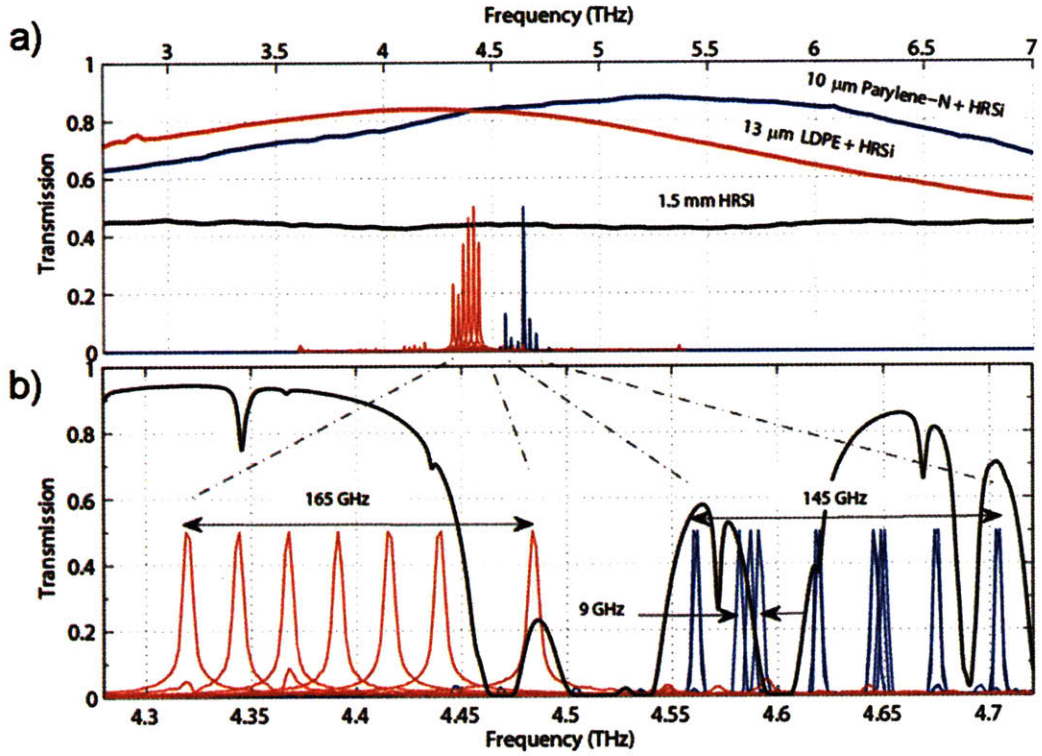

Figure 4-16 Part (a): Transmission spectra of anti-reflection coatings applied to both sides of a 1.5-mm thick HRSi window. Unnormalized QCL spectra of devices measuring 100-μm wide by 1.5-mm long (red) and 150-μm wide by 1.25-mm long (blue). Part (b): Enlarged and normalized spectra from (b) and calculated atmospheric transmission through external cavity (HITRAN 2008).

5 Summary and Future Work

5.1 Key Contributions

In this thesis I have described a system for real-time terahertz imaging using quantum-cascade lasers. To improve on the system, high-power, high-temperature and tunable quantum-cascade lasers were developed. A brief summary of some of the major accomplishments and experimental observations include the following:

- The development of the first real-time terahertz imaging system using a quantum-cascade laser. The system demonstrated 25 dB of SNR per pixel at a 20 Hz framerate when illuminated in transmission mode by a 4.3 THz, 48 mW (25% duty cycle) QCL. The equivalent pixel acquisition rate is ~4×10^5 pixels/second, over two orders of magnitude improvement over existing systems with similar SNRs. The system was demonstrated in a closed-cycle cryorefrigerator, demonstrated the feasibility of cryogen free real-time imaging with a quantum cascade laser.
- The microbolometer focal plane used for imaging was observed to have an optical noise equivalent power of $NEP_o \approx 320$ pW/$\sqrt{Hz}$ at 4.3 THz in differential mode. Key limitations of the NEP_o were identified to be the limited transmission of the germanium vacuum window and the low, 4% absorption of light at 4.3 THz.
- The lasing frequency of a quantum-cascade laser was coarsely adjusted to emit in the 4.9 THz atmospheric transmission window by adjusting the cavity dimensions. The resulting laser produced ~17 mW and was sufficient for illumination in real-time imaging over a 25-m distance.
- A high-power and high-temperature quantum-cascade laser is developed by butt-coupling a silicon lens to the facet of a metal-metal waveguide. The resulting device demonstrated a peak power of 145 mW, a record for metal-metal waveguide QCLs, while continuing to operate up to a heat

sink temperature of 160 K. This required the development of a technique for mounting and aligning the butt-coupled silicon lens. Calculations on the facet reflectivity suggest a reducing in reflectivity from ~74% to ~7%.

- Frequency tunable external cavity quantum-cascade lasers were developed demonstrated 165 GHz of mode-hopping tuning and 9 GHz of continuous tuning based on lens coupled, semi insulating surface plasmon waveguide based devices. Two external cavity configurations were explored and analyzed along with Parylene-N and LDPE anti-reflection coatings. A novel experimental technique was developed for measurement of the residual and external reflectivities of the external cavity lasers. The measurements revealed that the presence of the lens reduces the reflectivity below 1%, and the maximum external feedback is 8%.

5.2 Future Work

5.2.1 Depth Measurement in an imaging system (three dimensional imaging)

The work demonstrated in this thesis is primarily concerned with two dimensional imaging and spectroscopy thereof. However the tunable laser source can be used for depth measurement using an interferometer, which is commonly done at near-infrared wavelengths, known as optical coherence tomography [80, 103]. The first demonstrations of this technology measured the time of flight of femtosecond pulses reflecting from a sample. The measurement technique is similar to terahertz pulsed spectroscopy/imaging (TPS/TPI) setup as it uses a scanning reference mirror for range gating of the reflections from a sample. The resulting scan is similar to an ultrasound A-scan and is converted to full 3D imagery by fast raster scanning using galvo mirrors. However, due to the complexity of femtosecond mode locked laser sources, other techniques have been developed, notably the swept-source optical coherence tomography technique, which is described in [80] and shown for a terahertz configuration in Figure 5-1 part (a). Here the beam from a frequency tunable QCL is split into two paths, a reference arm and a sample arm. The beam in each arm is focused using a lens so that a small lateral dimension of the sample is interrogated. Reflections from the sample and

the reference arms are combined by the beam splitter and focused on a detector resulting in the signal, s, proportional to the received power:

$$s[k_m] = \eta \cdot P_o[k_m] \cdot \left[R_{ref} + \sum_{i=1}^{N} R_i + \sum_{i=1}^{N} 2\sqrt{R_i R_{ref}} \cdot \cos\left(2k_m \Delta x_i\right) \right] \quad \textbf{Eq. 5-1}$$

Where $k_m = 2\pi/\lambda_m$ is the m^{th} wave number, P_o is the power from the tunable source, R_{ref} is the reflectivity of the reference mirror including the loss of the beam splitter, R_i is the reflectivity of the i^{th} interface in the sample including the loss of the beam splitter, and Δx_i is the difference in path length between the i^{th} interface and the reference mirror. Expression Eq. 5-1 uses the simplifying assumptions that there are no multiple reflections in the sample (no Fabry-Pérot effect), that the index of refraction is uniform throughout[4], and neglects weaker interference terms. Part (b) shows a simulated signal from the detector resulting from the interference of the reflections from a dielectric layer attached to a metal substrate, and the reference arm, or N = 2 interfaces.

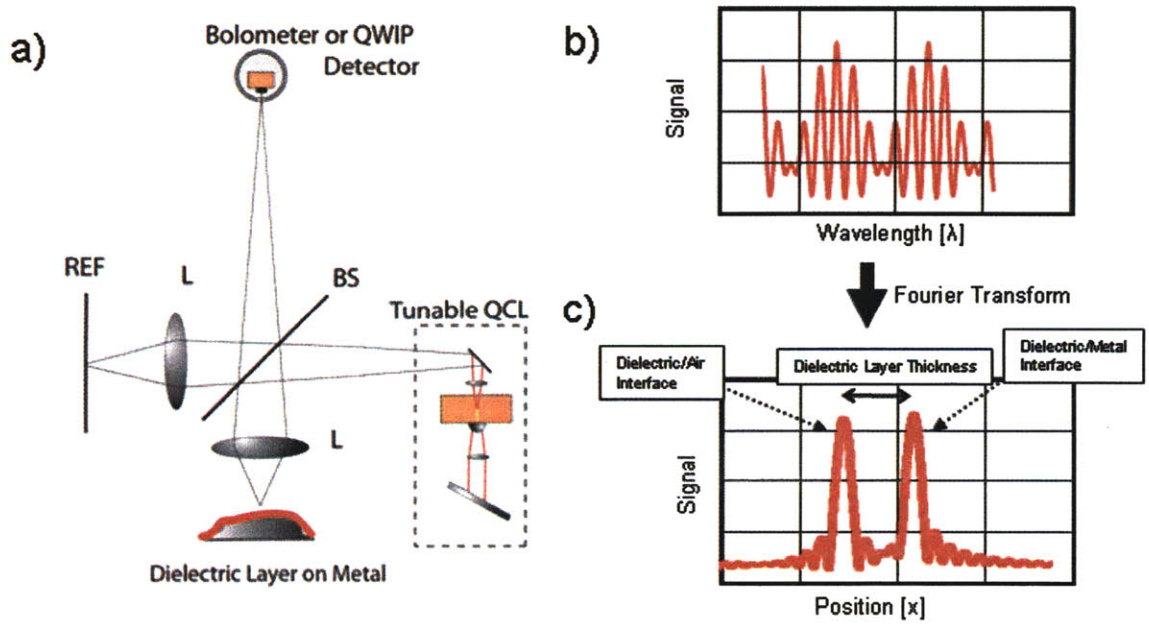

Figure 5-1 Part (a): Swept-Source Optical Coherence Tomography system. Components include frequency tunable QCL and interferometer using a beam splitter (BS) to divide the beam between a reference arm (REF) and a sample. Lenses (L) used for imaging a small point on a sample. Part (b):

[4] If this is not the case, the index of the refraction of the sample must be known to calculate the thickness of the sample, resulting in a modified argument of the cosine term in Eq. 5-1.

Resulting signal as a function of the laser wavelength, showing complex interference pattern between the reflections from the layers of the sample and REF. Part (c): Fourier transform of (b) reveals interfaces in the sample.

In order to determine the thickness of the dielectric layer, the signal is Fourier transformed, resulting in a depth profile of the sample (part c):

$$S[x] = \left| \sum_{k=1}^{M} s[k_m] e^{-jk_m x} \right| \qquad \textbf{Eq. 5-2}$$

Eq. 5-2 is effectively the convolution of the Fourier transform of the source spectrum $P_o[k_m]$ convolved with a delta function at every interface. The depth resolution, δx, is therefore limited by the spectral shape, and more importantly the bandwidth, Δf, of the source. For a rectangular spectral shape this gives:

$$\delta x = \frac{c}{2 \cdot \Delta f} \qquad \textbf{Eq. 5-3}$$

Were c is the speed of light. For example using the ~4.4 THz EC-QCL demonstrated in section 4, which as a ~5% bandwidth, would result in a depth resolution of 340 μm, where an extra factor of 2 improvement is obtained by dithering the reference mirror[104]. This expression only represent the full width at half maximum (FWHM) of a detected interface (e.g. the FWHM of one of the peaks in part (c)). If the SNR of the returned signal is high, smaller interface separations can be sub-resolved.

An alternative to the EC-QCL as tunable source, is a laser array shown in Figure 5-2. Here 32 individual laser ridges are fabricated into parallel distributed feedback (DFB) waveguides, as demonstrated in the mid-infrared [105]. The lasing frequency of each device can be selected by manipulating the grating parameters to achieve evenly spaced spectral coverage of several hundred GHz limited by the gain bandwidth of the gain medium. The lateral spacing of the array over ~1 mm results in difficulty in overlapping

the emitted beam, which can be overcome using a lens for collimation, and a grating to adjust parallelize the angle of emission as depicted in part b [106, 107]. The advantage of such an integrated source is that there are no moving parts, which allows a high-power rapid frequency scanning source.

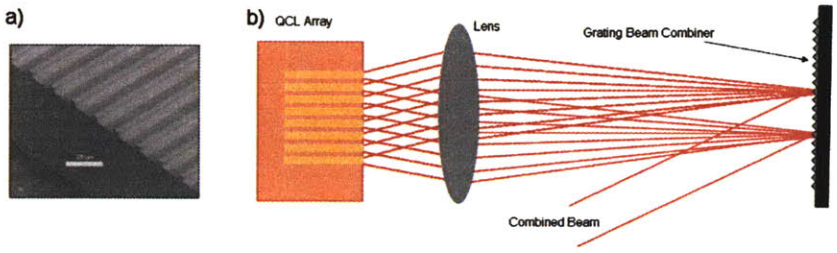

Figure 5-2: Part (a) shows an example of an array of frequency separated QCLs demonstrated in [105]. Part (b) shows the concept of this array using a lens and a grating to spatially combine the beam similar to [106].

5.2.2 Depth measurement using triangulation

Range finding by laser triangulation is commonly used in industry for the micron level depth accuracy and real-time operation [108-110]. Typically the collimated light from a visible or near infrared laser is reflected off the top surface of an object and imaged onto a CCD array. As the beam is scanned over the object, differences in the object height result in a change in position of the signal on the CCD. For a transparent object, light can be reflected off the interfaces within the object, and measurement can take place in specular (Figure 5-3 part (a)) or diffuse (part (b)) reflectance mode [111]. Laser triangulation allows depth information to be converted to lateral position information on the CCD.

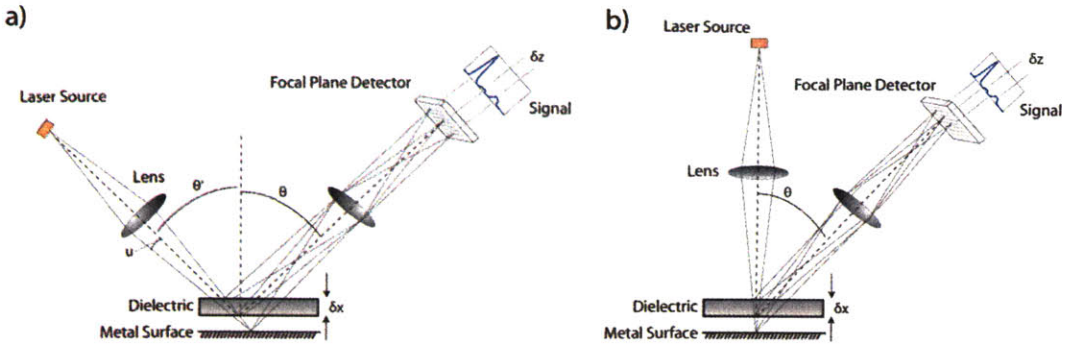

Figure 5-3 Laser triangulation in specular reflection (a) and diffuse reflection (b) configurations. In both configurations reflections from dielectric/metal interfaces are imaged to distinct positions on

focal plane array. A single line of the array ('Signal') is used to calculate the relative positions of the interfaces.

The depth resolution (δx) of a laser triangulation system is limited by the beam waist (ω_o) on the surface of the object [112]:

$$\delta x \approx \frac{\omega_o}{2 \cdot \sin\theta} = \frac{1}{2\pi} \cdot \frac{\lambda}{\sin u} \cdot \frac{1}{\sin\theta} \qquad \textbf{Eq. 5-4}$$

For a Gaussian beam the beam waist is $\omega_o = \lambda/\pi \cdot \sin u$, where λ is the wavelength of light, u is the angle of convergence of the laser beam incident on the surface and θ is the observing angle of the detector with respect to the surface normal. Laser triangulation clearly favors shorter wavelengths and larger observation angles. For optimized systems δz can be on the order of several wavelengths (~2 λ) [109, 112].

A proof of concept laser triangulation based imaging is shown in Figure 5-4. The setup is essentially the same as in section 2. The source is a ~50 mW peak power, 4.3 THz QCL mounted in a cooled to 30 K closed cycle, cryorefrigerator. The beam emitted from the QCL is collected by off-axis parabolic mirrors and is focused through an aperture to form a near diffraction-limited beam. The beam is focused with a 50 mm silicon lens so that the beam waist is approximately at the sample, which consists of a 3.2-mm thick high-density polyethylene (HDPE) sheet, separated by a variable distance from a metal reflecting surface. Due to the smooth surfaces of the polyethylene and metal layers, and the limited sensitivity (NEP≈320 pW/$\sqrt{}$Hz) of the microbolometer detector array, only specular reflections were obtainable. The specular reflection from the top interface (air/HDPE), bottom interface (HDPE/air), and metal layer are clearly visible in real-time as laterally displaced images of the beam waist. A plot of a single row from the microbolometer array allows the distances between the surfaces to be measured if the index of refraction of HDPE is known (n≈1.5). The minimum resolvable separation between the metal surface and the HDPE sheet was ~250 μm.

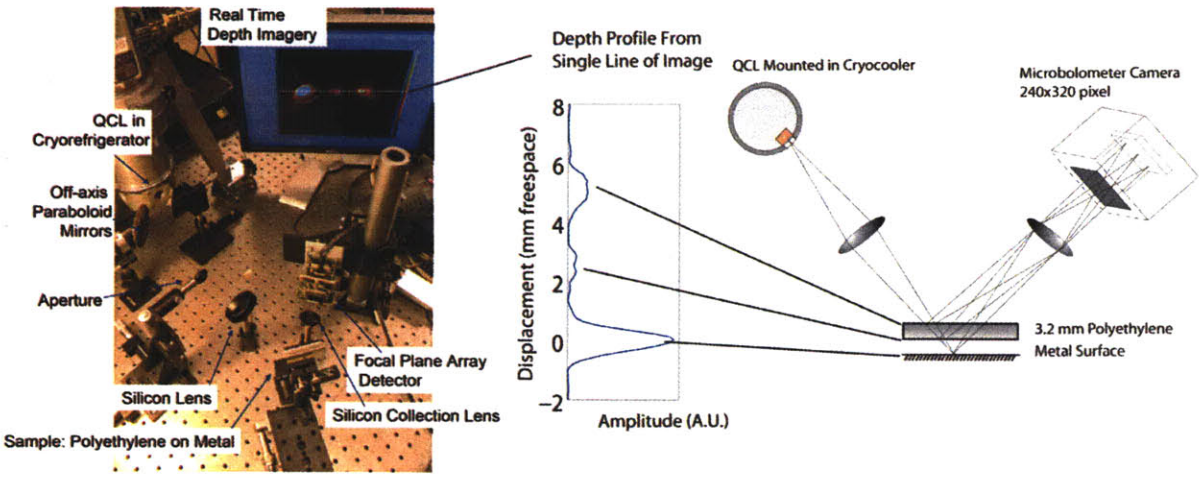

Figure 5-4 QCL based Laser Triangulation Prototype

Appendix A: Waveguide simulation parameters

In quantitative terms, SISP and metal-metal waveguides shown in Figure A-1, for typical dimensions used in this work, can be compared using the finite element electromagnetic simulation techniques described by *Kohen* [97]. Key waveguide parameters simulated at 4.4 THz are shown in Table A-1.

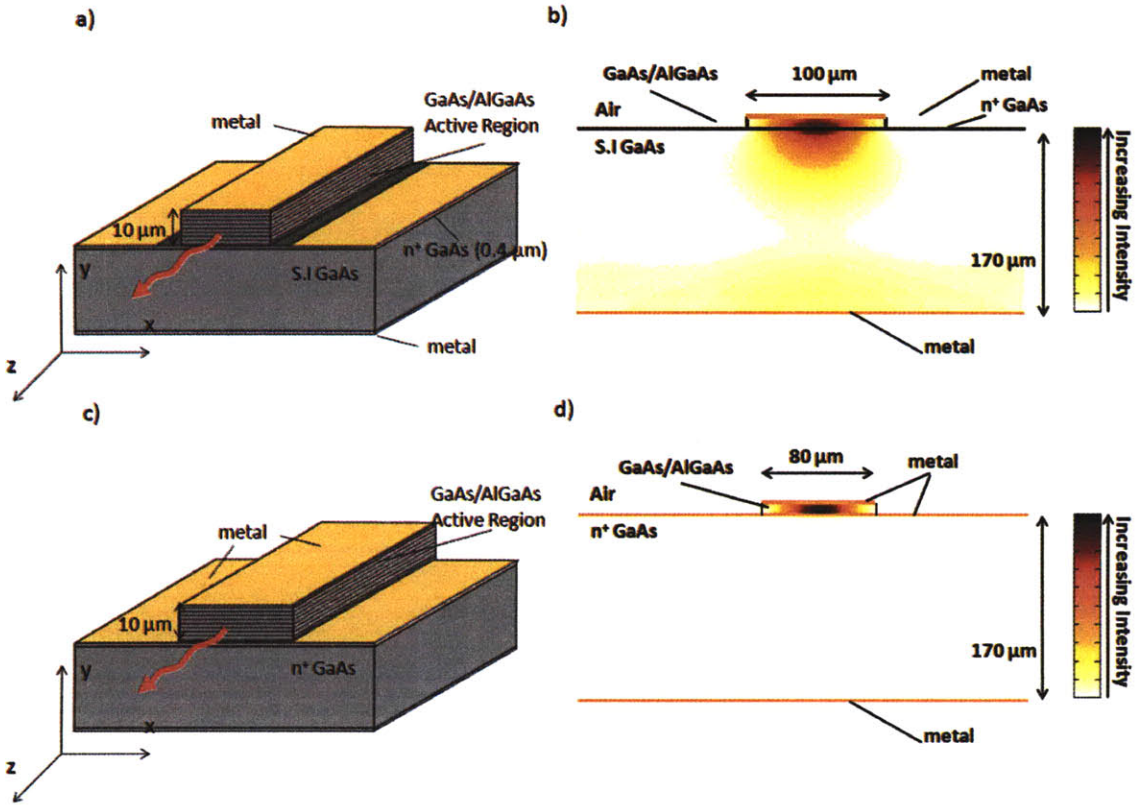

Figure A-1 Part (a) shows semi-insulating surface plasmon waveguide structure. Active region is has top metal contact, and sits above a thin, heavily n-doped layer (400 nm, silicon doped at 3×10^{18} cm^{-3}), above a nominally undoped (semi-insulating) substrate. A surface plasmon mode results from the negative dielectric constant of n-doped layer, resulting in the optical mode shown in (b). Part (c) shows metal-metal (MM) waveguide consisting of a top and bottom metal layers enclosing QCL active region. Part (d) shows optical mode and near unity optical confinement (overlap of optical mode with active region), similar to microstrip transmission line.

These parameters can be understood from the laser cavity roundtrip gain condition, which requires that the gain of the device be equal to the optical losses:

$$g_{th} = \frac{\alpha_{m1} + \alpha_{m2} + \alpha_w}{\Gamma} \quad [cm^{-1}] \qquad \textbf{Eq. 0-1}$$

The confinement factor, Γ, is the spatial overlap of the optical mode with the active region:

$$\Gamma = \frac{\iint_{active} |E_y|^2 dxdy}{\iint_{-\infty}^{\infty} |E|^2 dxdy} \qquad \textbf{Eq. 0-2}$$

and is modified to take into account the polarization selection rule which only couples the y-polarized electric field with the gain medium. The optical losses in Eq. 0-1 are due to the waveguide loss, α_w, which is dominated by free carrier loss[5], and mirrors loss, $\alpha_{m1,2}$:

$$\alpha_{m1,2} = -\frac{\log R_{1,2}}{2L} \quad [cm^{-1}] \qquad \textbf{Eq. 0-3}$$

Where $R_{1,2}$ are the reflectivities of the first and second mirror of the cavity and L is the length of the device.

The output power of either SISP or MM devices is proportional to the outcoupling factor:

$$P \propto \frac{\alpha_{m1}}{\alpha_{m1} + \alpha_{m2} + \alpha_w} \qquad \textbf{Eq. 0-4}$$

which is the ratio of the optical losses due to power coupled out of the device (useful loss, α_{m1} in the numerator) to the total optical losses (denominator). Using parameters from Table A-1 the outcoupling factor for SISP devices are seen to be ~56% (with the back facet covered with a high-reflectivity coating), whereas the outcoupling for a similarly

[5] The dielectric constant results from the Drude model $\epsilon(\omega) = \epsilon_{core} + \frac{j\sigma}{\omega}$ where $\sigma = \frac{ne^2\tau}{m^*(1-j\omega\tau)}$. For the active region the electron density is $n=5.5\times 10^{15}/cm^3$ and the scattering time τ=0.5 ps. For the plasma layer in the SISP waveguide $n=3\times10^{18}/cm^3$ with $\tau=0.1$ ps. For the metal layers $n=5.9\times10^{22}/cm^3$ and $\tau=0.05$ ps.

However, the total optical losses for the SISP devices, 42.7 cm^{-1} (with the back facet covered with a high-reflectivity coating), are significantly higher than MM waveguides, 13.1 cm^{-1}. This results in significantly higher lasing threshold current densities for SISP devices, and reduced high-temperature performance.

Table A-1 Key Waveguide Parameters for a 100-μm wide × 2-mm long device in a semi-insulating surface plasmon waveguide with a 170-μm thick SI-gaas substrate, and a 80 μm wide × 2-mm long metal metal waveguide device (fundamental mode), calculated at 4.4 THz.

Waveguide Parameter	SISP	MM
Width	100 μm	80 μm
Length	2 mm	2 mm
Confinement Factor, Γ	12%	98%
Facet Reflectivity, R	32%	74%
Single facet mirror loss, α_m	2.8 cm^{-1}	0.75 cm^{-1}
Scaled facet mirror loss, $\frac{\alpha_m}{\Gamma}$	23.8 cm^{-1}	0.76 cm^{-1}
Waveguide loss, α_w	2.3 cm^{-1}	11.3
Scaled Waveguide Loss, $\frac{\alpha_w}{\Gamma}$	19.0 cm^{-1}	11.5 cm^{-1}
Total Optical Loss, $\frac{2\cdot\alpha_m+\alpha_w}{\Gamma}$	66.5 cm^{-1}	13.1 cm^{-1}
Total Optical Loss with high-reflectivity coating, $\frac{\alpha_m+\alpha_w}{\Gamma}$	42.7 cm^{-1}	12.3 cm^{-1}
Outcoupling, $\frac{\alpha_m}{2\cdot\alpha_m+\alpha_w}$	35%	5.9%
Outcoupling, with high-reflectivity coating, $\frac{\alpha_m}{\alpha_m+\alpha_w}$	56%	6.2%

1. M. Skolnik, *Radar handbook* (McGraw-Hill Professional, 1990).
2. J. L. Tissot, "IR detection with uncooled sensors," Infrared Physics & Technology **46**, 147-153 (2004).
3. P. Kruse and D. Skatrud, *Uncooled infrared imaging arrays and systems* (Academic Press, 1997).
4. D. Leisawitz, "NASA's far-IR/submillimeter roadmap missions: SAFIR and SPECS," Advances in Space Research **34**, 631-636 (2004).
5. T. Phillips and J. Keene, "Submillimeter astronomy [heterodyne spectroscopy]," Proceedings of the IEEE **80**, 1662-1678 (1992).
6. D. T. Leisawitz, W. C. Danchi, M. J. DiPirro, L. D. Feinberg, D. Y. Gezari, M. Hagopian, W. D. Langer, J. C. Mather, J. Samuel H. Moseley, M. Shao, R. F. Silverberg, J. G. Staguhn, M. R. Swain, H. W. Yorke, and X. Zhang, "Scientific motivation and technology requirements for the SPIRIT and SPECS far-infrared/submillimeter space interferometers," in (SPIE, 2000), 36-46.
7. J. W. Waters, "Submillimeter-wavelength heterodyne spectroscopy and remote sensing of the upper atmosphere," Proceedings of the IEEE **80**, 1679-1701 (1992).
8. D. Auston and P. Smith, "Generation and detection of millimeter waves by picosecond photoconductivity," Applied Physics Letters **43**, 631 (1983).
9. M. Van Exter, C. Fattinger, and D. Grischkowsky, "Terahertz time-domain spectroscopy of water vapor," Opt. Lett. **14**, 1128-1130 (1989).
10. W. L. Chan, J. Deibel, and D. M. Mittleman, "Imaging with terahertz radiation," Rep. Prog. Phys. **70**, 1325-1379 (2007).
11. X. C. Zhang, "Terahertz wave imaging: horizons and hurdles," Phys Med Biol **47**, 3667--3677 (2002).
12. B. Ferguson and X.-C. Zhang, "Materials for terahertz science and technology," Nat Mater **1**, 26--33 (2002).
13. Teraview, "TPI Spectra 3000 Datasheet," in *www.teraview.com*, (Cambridge, 2008).
14. ZOmega, "Z-2 Terahertz Time Domain Spectrometer," in *www.zomega.com*, (2010).
15. Picometrix, "T-Ray 4000 TD-THz System," in *www.picometrix.com*, (2010).
16. X.C. Zhang, http://news.rpi.edu/update.do?artcenterkey=359, Accessed 11/01/09.
17. E. J. Heilweil and M. Campbell, "THz Spectral Database," (NIST, 2005).
18. R. S. Tera-photonics Laboratory, "RIKEN THz Spectral Database," (2005).
19. P. F. Taday, I. V. Bradley, D. D. Arnone, and M. Pepper, "Using Terahertz pulse spectroscopy to study the crystalline structure of a drug: a case study of the polymorphs of ranitidine hydrochloride," J Pharm Sci **92**, 831--838 (2003).
20. P. F. Taday, "Applications of terahertz spectroscopy to pharmaceutical sciences," Philos Transact A Math Phys Eng Sci **362**, 351--363; discussion 363-354 (2004).
21. B. B. Hu and M. C. Nuss, "Imaging with terahertz waves," Optics Letters **20**, 1716 - (1995).
22. Teraview, "TPI Imaga 2000 Datasheet," in *www.teraview.com*, (Cambridge, 2008).
23. D. Zimdars, J. A. Valdmanis, J. S. White, G. Stuk, S. Williamson, W. P. Winfree, and E. I. Madaras, "Technology and Applications of Terahertz Imaging Non-

Destructive Examination: Inspection of Space Shuttle Sprayed On Foam Insulation," in (AIP, 2005), 570-577.
24. N. Karpowicz, H. Zhong, C. Zhang, K.-I. Lin, J.-S. Hwang, J. Xu, and X.-C. Zhang, "Compact continuous-wave subterahertz system for inspection applications," Applied Physics Letters **86**, 054105 (2005).
25. H. Zhong, N. Karpowicz, J. Xu, M. Shur, and X. C. Zhang, "Inspection of Space Shuttle Insulation Panels with CW THz Radiation," in *RICC,* (2004).
26. NASA, "Columbia Accident Invsetigation Board Report Vol I," (NASA, 2003).
27. NASA, "NASA's Implementation Plan for Space Shuttle Return to Flight and Beyond (12th ed)," (2006).
28. D. Graham-Rowe, "Terahertz takes to the stage," Nat Photon **1**, 75-77 (2007).
29. Q. Wu, T. D. Hewitt, and X. C. Zhang, "Two-dimensional electro-optic imaging of THz beams," Applied Physics Letters **69**, 1026-1028 (1996).
30. T. Yasui, K.-I. Sawanaka, A. Ihara, E. Abraham, M. Hashimoto, and T. Araki, "Real-time terahertz color scanner for moving objects," Optics Express **16**, 1208-1221 (2008).
31. A. Nahata, J. T. Yardley, and T. F. Heinz, "Two-dimensional imaging of continuous-wave terahertz radiation using electro-optic detection," Applied Physics Letters **81**, 963 (2002).
32. P. H. Siegel, "Terahertz technology," IEEE Transactions on Microwave Theory and Techniques **50**, 910-928 (2002).
33. D. Woolard, W. Loerop, and M. Shur, *Terahertz Sensing Technology: Electronic devices and advanced systems technology* (World Scientific Pub Co Inc, 2003).
34. J. S. Ward, G. Chattopadhyay, J. Gill, H. Javadi, C. Lee, R. Lin, A. Maestrini, F. Maiwald, I. Mehdi, E. Schlecht, and P. Siegel, "Tunable broadband frequency-multiplied terahertz sources," in *Infrared, Millimeter and Terahertz Waves, 2008. IRMMW-THz 2008. 33rd International Conference on*, 2008), 1-3.
35. M. Rosenbluh, R. J. Temkin, and K. J. Button, "Submillimeter laser wavelength tables," Appl. Opt. **15**, 2635-2644 (1976).
36. E. Mueller, R. Henschke, J. Robotham, WE, L. Newman, L. Laughman, R. Hart, J. Kennedy, and H. Pickett, "Terahertz local oscillator for the Microwave Limb Sounder on the Aura satellite," Applied Optics **46**, 4907-4915 (2007).
37. E. Mueller, J. Fontanella, and R. Henschke, "Stabilized, Integrated, Far-Infrared Laser System for NASA/Goddard Space Flight Center," in 2000),
38. A. W. M. Lee and Q. Hu, "Real-time, continuous-wave terahertz imaging by use of a microbolometer focal-plane array," Optics Letters **30**, 2563 - 2565 (2005).
39. R. J. Blackwell, T. Bach, D. O'Donnell, J. Geneczko, and M. Joswick, "17 mu m pixel 640 x 480 microbolometer FPA development at BAE Systems," in (SPIE, 2007), 65421U-65424.
40. N. R. Butler, R. Blackwell, R. Murphy, R. Silva, and C. A. Marshall, "Low-cost uncooled microbolometer imaging system for dual use," in Proceedings of SPIE - The International Society for Optical Engineering (Society of Photo-Optical Instrumentation Engineers, Bellingham, WA, USA, 1995), 583-591.
41. A. W. M. Lee, B. S. Williams, S. Kumar, Q. Hu, and J. L. Reno, "Real-time imaging using a 4.3-THz quantum cascade laser and a 320 x 240 microbolometer focal-plane array," IEEE Photonics Technology Letters **18**, 1415 - 1417 (2006).

42. R. Köhler, A. Tredicucci, F. Beltram, H. E. Beere, E. H. Linfield, A. G. Davies, D. A. Ritchie, R. C. Iotti, and F. Rossi, "Terahertz semiconductor-heterostructure laser," Nature **417**, 156--159 (2002).
43. M. Rochat, L. Ajili, H. Willenberg, J. Faist, H. Beere, G. Davies, E. Linfield, and D. Ritchie, "Low-threshold terahertz quantum-cascade lasers," Applied Physics Letters **81**, 1381-1383 (2002).
44. B. S. Williams, H. Callebaut, S. Kumar, Q. Hu, and J. L. Reno, "3.4-THz quantum cascade laser based on longitudinal-optical-phonon scattering for depopulation," Applied Physics Letters **82**, 1015 - 1017 (2003).
45. C. Walther, M. Fischer, G. Scalari, R. Terazzi, N. Hoyler, and J. Faist, "Quantum cascade lasers operating from 1.2 to 1.6 THz," Applied Physics Letters **91**, 131122 (2007).
46. A. W. M. Lee, Q. Qin, S. Kumar, B. S. Williams, Q. Hu, and J. L. Reno, "Real-time terahertz imaging over a standoff distance (>25 meters)," Applied Physics Letters **89**, 141125 - (2006).
47. A. A. Danylov, J. Waldman, T. M. Goyette, A. J. Gatesman, R. H. Giles, J. Li, W. D. Goodhue, K. J. Linden, and W. E. Nixon, "Terahertz sideband-tuned quantum cascade laser radiation," Opt Express **16**, 5171--5180 (2008).
48. J. R. Gao, J. N. Hovenier, Z. Q. Yang, J. J. A. Baselmans, A. Baryshev, M. Hajenius, T. M. Klapwijk, A. J. L. Adam, T. O. Klaassen, B. S. Williams, S. Kumar, Q. Hu, and J. L. Reno, "Terahertz heterodyne receiver based on a quantum cascade laser and a superconducting bolometer," Applied Physics Letters **86**, 244104 - (2005).
49. Q. Hu, B. S. Williams, S. Kumar, H. Callebaut, S. Kohen, and J. L. Reno, "Resonant-phonon-assisted THz quantum-cascade lasers with metal-metal waveguides," Semiconductor Science and Technology **20**, 228 - 236 (2005).
50. B. S. Williams, "Terahertz quantum-cascade lasers," Nat Photon **1**, 517-525 (2007).
51. S. Kumar, "Development of Terahertz Quantum-Cascade Lasers," (Massachusetts Institute of Technology, 2007).
52. J. Faist, F. Capasso, D. L. Sivco, C. Sirtori, A. L. Hutchinson, and A. Y. Cho, "Quantum Cascade Laser," Science **264**, 553-556 (1994).
53. S. Kumar, Q. Hu, and J. L. Reno, "186 K operation of terahertz quantum-cascade lasers based on a diagonal design," Applied Physics Letters **94**, 131105-131103 (2009).
54. B. S. Williams, S. Kumar, Q. Hu, and J. L. Reno, "High-power terahertz quantum-cascade lasers," Electronics Letters **42**, 89 - 91 (2006).
55. J. Ulrich, R. Zobl, N. Finger, K. Unterrainer, G. Strasser, and E. Gornik, "Terahertz-electroluminescence in a quantum cascade structure," Physica B: Condensed Matter **272**, 216-218 (1999).
56. S. Kohen, B. S. Williams, and Q. Hu, "Electromagnetic modeling of terahertz quantum cascade laser waveguides and resonators," Journal of Applied Physics **97**, 053106 - (2005).
57. A. J. L. Adam, I. Kasalynas, J. N. Hovenier, T. O. Klaassen, J. R. Gao, E. E. Orlova, B. S. Williams, S. Kumar, Q. Hu, and J. L. Reno, "Beam patterns of

terahertz quantum cascade lasers with subwavelength cavity dimensions," Applied Physics Letters **88**, 151105 - (2006).
58. A. W. M. Lee, Q. Qin, S. Kumar, B. S. Williams, Q. Hu, and J. L. Reno, "High-power and high-temperature THz quantum-cascade lasers based on lens-coupled metal-metal waveguides," Optics Letters **32**, 2840 - 2842 (2007).
59. A. W. M. Lee, B. S. Williams, S. Kumar, Q. Hu, and J. L. Reno, "Tunable Terahertz Quantum Cascade Lasers with External Gratings," Optics Letters **accepted for publication**(2010).
60. G. J. Stacey, J. W. Beeman, E. E. Haller, N. Geis, A. Poglitsch, and M. Rumitz, "Stressed and unstressed Ge:Ga detector arrays for airborne astronomy," International Journal of Infrared and Millimeter Waves **13**, 1689-1707 (1992).
61. A. Poglitsch, C. Waelkens, and N. Geis, "The Photodetector Array Camera and Spectrometer(PACS) for the Herschel Space Observatory," in 2003), 662-673.
62. H. Luo, H. C. Liu, C. Y. Song, and Z. R. Wasilewski, "Background-limited terahertz quantum-well photodetector," Applied Physics Letters **86**, 231103-231103 (2005).
63. H. C. Liu, C. Y. Song, A. J. SpringThorpe, and J. C. Cao, "Terahertz quantum-well photodetector," Applied Physics Letters **84**, 4068-4070 (2004).
64. G. Huang, W. Guo, P. Bhattacharya, G. Ariyawansa, and A. G. U. Perera, "A quantum ring terahertz detector with resonant tunnel barriers," Applied Physics Letters **94**, 101115 (2009).
65. B. L. Cardozo, "GaAs Blocked-Impurity-Band Detectors for Far-Infrared Astronomy," (University of California at Berkeley, 2004).
66. J. Farhoomand, D. Sisson, and J. Beeman, "A low noise 2 × 16 Ge:Sb focal-plane array: Paving the way for large format FPAs for far IR astronomy," Infrared Physics & Technology **51**, 102-112 (2007).
67. IrLabs, "Scientific and Technical Products Catalog," (2008).
68. P. L. Richards, "Bolometers for Infrared and Millimeter Waves," Journal of Applied Physics **76**, 1-24 (1994).
69. N. Fieldhouse, S. M. Pursel, M. W. Horn, and S. S. N. Bharadwaja, "Electrical properties of vanadium oxide thin films for bolometer applications: processed by pulse dc sputtering," Journal of Physics D: Applied Physics, 055408 (2009).
70. E. Palik and G. Ghosh, *Handbook of optical constants of solids* (Academic press, 1985).
71. J. Geneczko, R. Blackwell, and M. Kohin, "MULTI-SPECTRAL UNCOOLED MICROBOLOMETER DETECTORS," WO 20051094460 A2 (2005).
72. L. S. Rothman, D. Jacquemart, A. Barbe, D. C. Benner, M. Birk, L. R. Brown, M. R. Carleer, C. Chackerian Jr, K. Chance, L. H. Coudert, V. Dana, V. M. Devi, J. M. Flaud, R. R. Gamache, A. Goldman, J. M. Hartmann, K. W. Jucks, A. G. Maki, J. Y. Mandin, S. T. Massie, J. Orphal, A. Perrin, C. P. Rinsland, M. A. H. Smith, J. Tennyson, R. N. Tolchenov, R. A. Toth, J. Vander Auwera, P. Varanasi, and G. Wagner, "The HITRAN 2004 molecular spectroscopic database," Journal of Quantitative Spectroscopy and Radiative Transfer **96**, 139-204 (2005).
73. E. E. Orlova, J. N. Hovenier, T. O. Klaassen, I. Kasalynas, A. J. L. Adam, J. R. Gao, T. M. Klapwijk, B. S. Williams, S. Kumar, Q. Hu, and J. L. Reno, "Antenna model for wire lasers," Phys Rev Lett **96**, 173904 (2006).

74. S. Kumar, B. S. Williams, Q. Qin, A. W. M. Lee, Q. Hu, and J. L. Reno, "Surface-emitting distributed feedback terahertz quantum-cascade lasers in metal-metal waveguides," Optics Express **15**, 113 - 128 (2007).
75. J. A. Fan, M. A. Belkin, F. Capasso, S. Khanna, M. Lachab, A. G. Davies, and E. H. Linfield, "Surface emitting terahertz quantum cascade laser with a double-metal waveguide," Opt. Express **14**, 11672-11680 (2006).
76. D. Rutledge, D. Neikirk, D. Kasilingam, and I. Antennas, "Infrared and Millimeter Waves, vol. 10," Orlando, FL: Academic (1983).
77. M. Born and E. Wolf, *Principles of optics* (Pergamon, 1959).
78. H. Callebaut, S. Kumar, B. S. Williams, Q. Hu, and J. L. Reno, "Analysis of transport properties of tetrahertz quantum cascade lasers," Applied Physics Letters **83**, 207 - 209 (2003).
79. C. Gmachl, "Tunable Terahertz Lasers: A wrench of wavelength," Nat Photon **3**, 683-684 (2009).
80. M. Choma, M. Sarunic, C. Yang, and J. Izatt, "Sensitivity advantage of swept source and Fourier domain optical coherence tomography," Opt. Express **11**, 2183-2189 (2003).
81. A. F. Fercher, C. K. Hitzenberger, G. Kamp, and S. Y. El-Zaiat, "Measurement of intraocular distances by backscattering spectral interferometry," Optics Communications **117**, 43-48 (1995).
82. M. Gaidis, H. Pickett, C. Smith, S. Martin, R. Smith, and P. Siegel, "A 2. 5-THz receiver front end for spaceborne applications," IEEE Transactions on Microwave Theory and Techniques **48**, 733-739 (2000).
83. H. Liu, H. Zhong, N. Karpowicz, Y. Chen, and X. Zhang, "Terahertz spectroscopy and imaging for defense and security applications," Proceedings of the IEEE **95**, 1514-1527 (2007).
84. R. A. Kingston, *Detection of Optical and Infrared Radiation*, Springer Series in Optical Sciense (Springer-Verlag, 1978), Vol. 10, p. 138.
85. B. S. Williams, S. Kumar, Q. Hu, and J. L. Reno, "Distributed-feedback terahertz quantum-cascade lasers with laterally corrugated metal waveguides," Optics Letters **30**, 2909 - 2911 (2005).
86. A. L. Betz, R. T. Boreiko, B. S. Williams, S. Kumar, Q. Hu, and J. L. Reno, "Frequency and phase-lock control of a 3 THz quantum cascade laser," Optics Letters **30**, 1837 - 1839 (2005).
87. L. A. Dunbar, R. Houdre, G. Scalari, L. Sirigu, M. Giovannini, and J. Faist, "Small optical volume terahertz emitting microdisk quantum cascade lasers," Applied Physics Letters **90**, 141114-141113 (2007).
88. H. Zhang, L. A. Dunbar, G. Scalari, R. Houdré, and J. Faist, "Terahertz photonic crystal quantum cascade lasers," Opt. Express **15**, 16818-16827 (2007).
89. J. Hensley, D. Bamford, M. Allen, J. Xu, A. Tredicucci, H. Beere, and D. Ritchie, "Demonstration of an External Cavity Terahertz Quantum Cascade Laser," in *Optical Terahertz Science and Technology*, Technical Digest (Optical Society of America, 2005), TuA3.
90. D. Fenner, J. Hensley, M. Allen, J. Xu, and A. Tredicucci, "Antireflection Coating for External-Cavity Quantum Cascade Laser Near 5 THz," (2007).

91. J. Xu, J. M. Hensley, D. B. Fenner, R. P. Green, L. Mahler, A. Tredicucci, M. G. Allen, F. Beltram, H. E. Beere, and D. A. Ritchie, "Tunable terahertz quantum cascade lasers with an external cavity," Applied Physics Letters **91**, 1-3 (2007).
92. J. Hensley, D. Fenner, M. Allen, J. Xu, R. Green, L. Mahler, A. Tredicucci, F. Beltram, and H. Beere, "An External Cavity 4.7 Terahertz Quantum Cascade Laser," in *Optical Terahertz Science and Technology,* (Optical Society of America, 2007).
93. K. Lee, T. Lu, and X. Zhang, "Tera Tool [terahertz time-domain spectroscopy]," IEEE Circuits and Devices Magazine **18**, 23-28 (2002).
94. K. Kawase and N. Hiromoto, "Terahertz-Wave Antireflection Coating on Ge and GaAs with Fused Quartz," Appl. Opt. **37**, 1862-1866 (1998).
95. M. Born, E. Wolf, and A. Bhatia, "Principles of optics," (1964).
96. G. Rebeiz, "Millimeter-wave and terahertz integrated circuit antennas," Proceedings of the IEEE **80**, 1748-1770 (1992).
97. S. Kohen, "Electromagnetic Modeling of Terahertz Quantum Cascade Laser Waveguides and Resonators," (Massachusetts Institute of Technology, Cambridge, 2004).
98. D. Filipovic, G. Gauthier, S. Raman, and G. Rebeiz, "Off-axis properties of silicon and quartz dielectric lens antennas," IEEE Transactions on Antennas and Propagation **45**, 760-766 (1997).
99. L. Coldren and S. Corzine, *Diode lasers and photonic integrated circuits* (Wiley, New York, 1995).
100. H. Hübers, J. Schubert, A. Krabbe, M. Birk, G. Wagner, A. Semenov, G. Gol'tsman, B. Voronov, and E. Gershenzon, "Parylene anti-reflection coating of a quasi-optical hot-electron-bolometric mixer at terahertz frequencies," Infrared Physics and Technology **42**, 41-47 (2001).
101. A. J. Gatesman, J. Waldman, M. Ji, C. Musante, and S. Yngvesson, "Anti-reflection coating for silicon optics at terahertz frequencies," IEEE Microwave and Guided Wave Letters **10**, 264-266 (2000).
102. B. S. Williams, "Terahertz quantum cascade lasers," 2003).
103. G. Tearney, M. Brezinski, J. Southern, B. Bouma, M. Hee, and J. Fujimoto, "Determination of the refractive index of highly scattering human tissue by optical coherence tomography," Opt. Lett **20**, 2258–2260 (1995).
104. M. Wojtkowski, A. Kowalczyk, R. Leitgeb, and A. F. Fercher, "Full range complex spectral optical coherence tomography technique in eye imaging," Opt. Lett. **27**, 1415-1417 (2002).
105. B. G. Lee, M. A. Belkin, R. Audet, J. MacArthur, L. Diehl, C. Pflugl, F. Capasso, D. C. Oakley, D. Chapman, A. Napoleone, D. Bour, S. Corzine, G. Hofler, and J. Faist, "Widely tunable single-mode quantum cascade laser source for mid-infrared spectroscopy," Applied Physics Letters **91**, 231101-231103 (2007).
106. V. Daneu, A. Sanchez, T. Y. Fan, H. K. Choi, G. W. Turner, and C. C. Cook, "Spectral beam combining of a broad-stripe diode laser array in an external cavity," Opt. Lett. **25**, 405-407 (2000).
107. B. G. Lee, J. Kansky, A. K. Goyal, C. Pflügl, L. Diehl, M. A. Belkin, A. Sanchez, and F. A. Capasso, "Beam combining of quantum cascade laser arrays," Opt. Express **17**, 16216-16224 (2009).

108. F. Blais, "Review of 20 years of range sensor development," Journal of Electronic Imaging **13**, 231-243 (2004).
109. Micro-Epsilon, "Laser Triangulation Displacement Sensors," (Micro-Epsilon, Raleigh, NC, 2009).
110. W. Pastorius, "Triangulation sensors: An overview" (InTech, FindArticles.com, 2001), retrieved 29 Aug, 2009, http://findarticles.com/p/articles/mi_qa3739/is_200107/ai_n8997992/
111. J. P. Peterson and R. B. Peterson, "Laser triangulation for liquid film thickness measurements through multiple interfaces," Appl. Opt. **45**, 4916-4926 (2006).
112. R. G. Dorsch, G. Häusler, and J. M. Herrmann, "Laser triangulation: fundamental uncertainty in distance measurement," Appl. Opt. **33**, 1306-1314 (1994).